SHOCK-INDUCED C_2H_2 PYROLYSIS AND CO EMISSIVITY

Thesis by

William Joseph Hooker

In Partial Fulfillment of the Requirements

For the Degree of

Doctor of Philosophy

California Institute of Technology

Pasadena, California

1958

TO MY WIFE

ACKNOWLEDGEMENTS

I wish to express my gratitude for the opportunity granted me to study and to do research at the California Institute of Technology. I extend my thanks to the graduate faculy and, in particular, to Dr. S. S. Penner, whose enthusiastic support and frequent technical counsel made this research possible.

I wish to thank Drs. A. T. Ellis, U. Oppenheim and Mr. D. Weber for many helpful discussions of experimental problems. I sincerely appreciate the time devoted by Mr. A. Thomson to the interpretation of many physical phenomena of general interest to the field of this research.

The research reported in Part I was supported by the U. S. Air Force through the Air Force Office of Scientific Research of the Air Research and Development Command under Contract No. AF18(603)-2.

The research reported in Part II was supported by the Physics Branch of the Office of Naval Research, U. S. Navy, under Contract Nonr-220(03), NR 015 401.

Full credit for the professional typing preparation of this manuscript goes to Miss Ruth Winkel.

ABSTRACT

PART I: SHOCK TUBE STUDIES OF ACETYLENE DECOMPOSITION

Extensive experimental studies have been conducted on the rate of decomposition of argon-acetylene mixtures by means of shock waves. Activation energies of 26 and 33 kcal/mole, respectively, have been found for the first- and second-order decomposition reactions of acetylene.

A well defined curve of temperature versus induction time for incipient carbon formation has been established. Analysis of these data suggests that possibly a somewhat better correlation is obtained for decomposition reactions of order $n = 1$ and $n = 1.5$ than for $n = 2$. The corresponding activation energies are 10, 13 and 16 kcal/mole for $n = 1$, 1.5 and 2, respectively.

The effects of impurity and diluent gas radiation, as well as molecular and solid particle light scattering, have been shown to have a negligibly small influence on the results.

PART II: AN ANALYSIS OF EQUILIBRIUM INFRARED GAS EMISSIVITIES FOR DIATOMIC MOLECULES BASED ON A JUST-OVERLAPPING ROTATIONAL LINE MODEL

General equations are developed for the engineering emissivity of diatomic molecules with equally intense R- and P-branches and just-overlapping rotational line structures. Integral expressions for the emissivity are evaluated by exact numerical integration and by approximate series representations.

The results are applied to the molecules CO and HCℓ. Comparisons are made with emissivity predictions for the same molecules with a completely overlapped rotational line model and an isolated rotational line model. The theoretical emissivity calculations for CO are in fair accord with empirically determined estimates.

TABLE OF CONTENTS

PART I.

SHOCK TUBE STUDIES OF ACETYLENE DECOMPOSITION

PART II.

AN ANALYSIS OF EQUILIBRIUM INFRARED GAS EMISSIVITIES FOR DIATOMIC MOLECULES BASED ON A JUST-OVERLAPPING ROTATIONAL LINE MODEL

LIST OF SYMBOLS

B_e	equilibrium rotational constant
c	velocity of light
d	Kerr-cell plate separation
d	mass density
D_e	rotational energy level constant
E	activation energy for acetylene decomposition
E_D	activation energy for incipient carbon formation
$E_{n,j}$	energy level of the state (n, j)
f	frequency
H	magnetic field strength
h	Planck's constant
I_e	equilibrium moment of inertia
I_o	radiation intensity incident on an observation region
I, I_t	radiation intensity transmitted through an observation region
k	Boltzmann's constant
K	Kerr constant
L	length
ΔL	change in length
m_r	reduced mass of vibrating diatomic molecule
N_o	number density of particles at S. T. P.
$N_{n,j}$	number density of particles in the state (n, j)
N_T	total number density of particles
$P(\omega)$	spectral absorption coefficient
p	pressure

Q	partition function
$R(\omega)$	spectral radiancy
$R^o(\omega)$	blackbody spectral radiancy
R	molar gas constant
$\|R_{n,n'}\|^2$	square of vibrational matrix element
S	integrated intensity for a vibration-rotation band
S	integrated intensity for a spectral line
T	tension
T	temperature
T	fractional transmission
V	voltage
V	Verdet constant
X	optical depth
α	integrated intensity of a vibration-rotation band
α_e	vibration-rotation energy level constant
δ	rotational line spacing
ϵ	engineering emissivity
$\Gamma(z)$	gamma function of argument 2.
μ	micron (wavelength)
μ_1	linear term in dipole moment
ω	wave number
$\Delta\omega$	wave number interval
$\omega_e x_e$	vibrational energy level constant
$\omega_e y_e$	vibrational energy level constant
ρ	mass per unit length
σ	tensile strength
σ	Stefan-Boltzmann constant

ϕ	angular rotation of plane of polarization
$\Delta\tau$	induction time

PART I.

SHOCK TUBE STUDIES OF ACETYLENE DECOMPOSITION

I. INTRODUCTION

The experimental research program discussed in the following sections forms a part of a continuing investigation in this laboratory on the mechanism of acetylene decomposition. The progress of pyrolysis in thermally excited argon-acetylene mixtures has been studied with the aid of shock tube techniques.

A considerable amount of time has been devoted to further development and improvement of shock-tube facilities constructed by earlier investigators (1), (2). Details of the facilities used by us are described in Sections II and III.

II. THE SHOCK TUBE AND ASSOCIATED MEASURING EQUIPMENT

A. The Shock Tube and Gas-Handling Systems

The shock tube used for experimental measurements was made from Shelby seamless steel tube with a three inch internal diameter and one-quarter inch wall thickness (1), (2). The internal surface of the tube appeared to be smooth, although no special operations were performed to change the surface conditions from those present when the tubing was purchased from the manufacturer.

The low-pressure section of the shock tube was either 1.695 or 2.000 meters long, depending on the type of experiment being performed. These lengths were chosen in such a way that a minimum time of 100 microseconds would be available for observation behind the incident shock wave for all possible variations of shock parameters.

The high-pressure section of the shock tube was 1.525 meters long. This length was determined by the imposed restriction that the reflected rarefaction wave should not arrive at the observation region sooner than 100 microseconds after the reflected shock wave intersected the contact surface. This criterion was established as a safety factor to preclude the possibility of quenching of the heated gases by the reflected rarefaction before all desired experimental measurements had been completed.

The individual sections of the shock tube were flanged at both ends. Sealing between a mating pair of flanges was effected by two concentric O-rings. Even though the flange faces had been carefully machined, air leakage past the O-rings prohibited the attainment of low vacuo. This problem was satisfactorily eliminated by hand-lapping the individual flange faces until a uniform transfer of Prussian blue high-spot indicator between mating flanges was obtained. The flange faces were lightly covered with Apiezon type M high-vacuum grease prior to assembly of the shock tube.

Accommodations for observation windows were present at selected positions along the low-pressure section of the shock tube wall. Figures 1 and 2 show cross sections of the two types of window holders used.

The windows used for all spectral radiation and absorption measurements in this research were made from commercial sapphire ($A\ell_2O_3$). This material possesses the very desirable properties of good durability, low cost and good spectral transmission characteristics.

An end plate for the low-pressure section of the shock tube was made with an axial recess for a pyrex observation window. Spectral radiation measurements in the visible region of the spectrum could then be made from an optical path that contained the axis of the shock tube.

The high-pressure section of the shock tube was fitted with a plunger mechanism for bursting the diaphragms at a specified pressure. The plunger consisted of a length of one-eighth inch diameter drill rod attached to a one and one-quarter inch diameter piston. The piston, machined to fit a cylinder bolted to the tube wall at a 45 degree angle, was accelerated by 100 psi shop air. The high-pressure air was admitted to the top of the cylinder by a quick-opening solenoid valve. The plunger was directed in such a way as to strike the diaphragm near the center, thereby bursting it.

After considerable experimentation it was found that better reproducibility of the shock wave velocity could be obtained by scoring the diaphragms in an appropriate manner and letting them burst by pressure alone, rather than by bursting them with the plunger. A device was designed and built to score the diaphragms in two mutually perpendicular directions to a uniform depth. The diaphragms used most often were made from hard, cold-rolled copper sheet of 0.016 inch thickness.

A manifold system was connected to the shock tube for handling of test gases and evacuation of the system. All parts of the manifold that were used for evacuation were made from 1/2 inch OD copper refrigeration tubing. Solder fittings were used throughout. Circle Seal type 9259B-2PP brass plug valves were used in all pumping lines. Hoke type 434 brass bellows valves were used for the Hg manometer line and the test gas mixing bottle and pressure gauge, while Hoke type 344 high-pressure packing valves were used in all the high-pressure lines.

A Kinney type K C 8 double stage mechanical pump and a Consolidated Vacuum Corp. type MCF-60 oil diffusion pump were used for evacuating the shock tube and associated gas-handling systems. The ultimate vacuum in the manifold system up to the shock tube was 10^{-4} mm Hg, while the shock tube itself could be pumped down to 5×10^{-4} mm Hg. The leak rate for the entire system was of the order of 0.1 micron per minute.

The Kinney pump discharged through a piping system to a hood to prevent oil vapors from settling on optical parts. The test gases could either be exhausted to the room or to the hood (figure 3).

Pressures in the range of fractions of millimeters of Hg were measured with the aid of a Phillips type PHG-09 vacuum gauge. This gauge was calibrated against a McLeod gauge and an ionization gauge.

Pressures in the range of fractions of an atmosphere were measured by use of a Wallace and Tiernan type FA-135-173 precision mercury manometer. The manometer was separated from the manifold by a dry ice-acetone cold trap (mixture temperature of -56°C was used; at this temperature Hg has a vapor pressure of less than 10^{-6} mm of Hg). The coolant prevented mercury vapors from contaminating the Phillips gauge.

Pressures above atmospheric were measured on Duragauge Laboratory Test Gauges and Marsh Mastergauges.

B. Shock Velocity Measurement

A one-dimensional, inviscid, flow analysis of the wave phenomena in a shock tube showed that all the pertinent state functions for the gases behind shock fronts could be calculated from a knowledge of the shock wave velocity.

The shock velocity was measured electronically by counting the transit time of the shock wave between two fixed stations along the shock tube wall (figure 3). Thin film platinum heat gauges of the type described by Rabinowicz et al (3) provided voltage pulses indicating the shock arrival at either station. Figure 4 shows the output-time characteristics of one of these gauges for typical experimental conditions. The physical dimensions and mounting details of one of the gauges are illustrated in figure 5.

The heat gauges proved to be the most durable and versatile shock detection devices used on our shock tube. The sensitivity and time response qualities of the gauges were essentially unaffected after more than 200 shock-tube experiments.

Strain-gauge and barium titanate pressure-sensing pickups were tried extensively as devices for measuring shock velocity, but both techniques suffered from the inherent natural frequency associated with the transducer mass, and from the superposed noise resulting from pressure waves inthe wall of the shock tube itself.

Schlieren devices for sensing density changes across a shock wave were employed successfully over a limited range of initial pressures; this method is also, in general, less satisfactory than the procedure using the heat gauges.

Drawings of the bias circuit and amplifier stages for the heat gauges are shown in figure 6. The original amplifier tubes were

6AC7's, giving an overall voltage gain of approximately 1000. This was more than sufficient to trigger the electronic counting apparatus. In later experiments, however, the sound noise connected with the operation of a mechanical light chopper introduced microphonic tube disturbances to the point where the electrical signal to noise ratio was near unity. This problem was eliminated by using the low-microphonic equivalent tube, 5693. Unfortunately, the gain characteristics of the 5693 are inferior to those of the 6AC7, and the overall amplifier voltage gain dropped to approximately 250, a value insufficient to activate the following counter apparatus. A Shasta Model 854 A wide-band preamplifier set at a voltage gain of ten was connected in series with each of the heat gauge amplifiers, thereby providing the necessary overall voltage gain.

Errors in shock velocity measurement arose from two factors. The first was due to the fact that the shock required a finite time to cross the gauge face. The minimum shock wave velocity for these experiments was approximately 1000 meters/second which, for a gauge width of 1 mm, resulted in a transit time of 1 microsecond. The second source of error was due to the inherent counting resolution of the Berkeley Model 7360 Counter, which ammounted to ± 1 count. These two factors lead to an uncertainty of ± 2 microseconds out of a minimum count time of 400 microseconds, i.e., ± 1/2 per cent.

C. Concentration Measurements of Test-Gas Mixtures

Generally, a necessary condition for the interpretation of data concerning molecular relaxation and dissociation phenomena is the requirement that the process involved must proceed in a nearly isothermal manner. This would apply to most of the experiments discussed here, where the temperature is known only from a calculation involving a knowledge of the shock velocity.

This condition can be met most simply by diluting the reacting gas under study with a large excess of inert gas. Argon was chosen as the diluent for all experiments reported herein, with acetylene as the reacting gas. Mixtures of 95 per cent of A - 5 per cent of C_2H_2 and 98 per cent of A - 2 per cent of C_2H_2 were used. The physicochemical properties of the highly diluted mixtures were largely determined by argon.

The numerical calculations of Bennett (2) were used for the 95 per cent of A - 5 per cent of C_2H_2 mixtures, while the tabulated values of Lukasiewicz (4) were used for the 98 per cent of A - 2 per cent of C_2H_2 mixtures (i.e., we treated the latter mixture ratio as pure argon). Graphs of the pertinent functions are reproduced in figures 7 to 12.

The argon-acetylene mixtures used for the experiments were thoroughly agitated with glass beads in a mixing bottle in order to insure homogeneous gas compositions (see figure 3).

The low partial pressures of acetylene admitted to the shock tube prior to an experiment introduced the possibility of error due to selective absorption of acetylene on the walls of the shock tube and associated gas-handling systems. It was considered a necessary step in the experimental procedure to measure the acetylene concentration directly in the shock tube before each test. Since the optical depth of the acetylene initially present in the shock tube varied from approximately 0.01 to 0.15 cm-atmos, the problem of quantitative analysis was complicated, and several methods were tried before a successful procedure was developed.

In the wavelength interval between 1900 and 2500 Å, acetylene has numerous electronic vibration-rotation bands (5). This region of the spectrum is not easily accessible, however, since the glass envelopes of the available photomultiplier radiation detectors have very poor transmission characteristics in this short wavelength region. No measurable absorption was obtained.

The fundamental vibration-rotation band of acetylene at 3287 cm^{-1} possesses the largest integrated intensity of the measured acetylene infrared bands ($\mathcal{S} = 590\ cm^{-2}\text{-}atmos^{-1}$) and, hence, is most easily observed. Three different methods for measuring the absorption of this band were tried.

The optical path which we used for gaseous concentration measurements physically coincided with one of the optical paths used for emission studies of heated gases behind shock fronts. This path was necessarily restricted in aperture and solid angle to meet the requirements of the emission experiments (see Section II E). In order to measure the concentration of acetylene in the shock tube, however, it was desirable to have as small an overall optical f-number as possible. To make these two requirements compatible, the collimating slit system was made in such a manner that it could be removed conveniently for initial concentration measurements and replaced quickly for radiation measurements behind shock fronts.

Because of lack of equipment in the early stages of our program, the first attempts at infrared absorption measurement were necessarily time-consuming and, in the end, unsuccessful. A Beckman I R-2 infrared prism instrument was available, equipped with an Eastman PbS detector, but the associated electronics were not in functioning condition. The power supply and light source (Nernst) regulator were eventually repaired by us, but the signal amplifying channels remained inoperable. A Tektronix low-level preamplifier was then used for amplifying the PbS signal, the output being recorded on an oscilloscope. This combination gave a favorable signal-to-noise ratio, but the PbS cell sensitivity, even when cooled with dry ice (the cell was originally intended to be uncooled) dropped off rapidly beyond two microns in the infrared, making it unsuitable for quantitative work.

A similar attempt was made using a Santa Barbara Research Center PbSe cell, both cooled and uncooled, but this failed also.

At this stage of the program a Perkin-Elmer Model 13 Infrared Spectrophotometer was made available, and suitable mounts and optics were devised to fit it into the existing optical system. The Perkin-Elmer was first tried with a PbS cell that came with the instrument, the signal being registered on a Leeds and Northrup Recorder. The uncooled PbS cell sensitivity went essentially to zero in the middle of the 2.7 μ water band, and we were unable to detect acetylene overtone bands in the range of its maximum strength.

The standard thermocouple supplied with the instrument was the last detector used, and while the signal-to-noise ratio at first was near unity, with suitable changes in the optical system the signal was increased in magnitude to the point (approximately 1 microvolt) where noise was virtually undetectable.

The spectral slit width used for the final measurements was approximately 6 cm^{-1} with an LiF prism. An LiF prism, rather than an NaCℓ prism, was used since the linear dispersion at the exit slit for LiF is less than one-fifth that of NaCℓ in the spectral range covering the band with center at 3287 cm^{-1} (6).

In figure 13 an experimental plot of $\ell n(I/I_o)$ vs acetylene partial pressure in mm Hg is presented to illustrate the sensitivity of the measuring technique. Here I/I_o is the ratio of transmitted to incident intensity for infrared radiation absorbed by acetylene in the shock tube.

Besides providing a quantitative measure of the acetylene concentration in the shock tube prior to an experiment, recording of the infrared absorption gave an independent check on the homogeneity of the argon-acetylene mixtures. It was found that five minutes of vigorous shaking with glass beads in the mixing bottle was sufficient to produce a uniformly mixed gas.

D. Radiation Detectors

Photomultiplier radiation detectors were used to convert spectral emissions in the visible region of the spectrum into measurable signals. Two variations of the standard voltage divider network for the photomultiplier power supply were tried. The standard network is shown in figure 14a. A power supply in which batteries of the proper voltage have replaced the dropping resistors is shown in figure 14b, and in figure 14c the standard network with added dynode to dynode capacitance is illustrated. In terms of frequency response to a rapidly oscillating applied light signal, the standard network was poorest, while the other two circuits had negligible charging time loss for a 200 kc signal. The circuit illustrated in figure 14c is the one that was finally adopted.

In general, IP28 photomultiplier tubes were used because of their superior sensitivity and noise characteristics.

An InSb semi-conducting infrared radiation detector was used for monitoring spectral radiations with wavelengths greater than one micron. The detector was developed by the Chicago Midway Laboratories, Chicago University, under sponsorship of the U. S. Air Force.

The InSb cell, equipped with a sapphire window, could detect radiation to at least 6 microns in the infrared, at which point the LiF prism transmission began to decrease. Figure 15 shows a plot of relative intensity versus wavelength for the InSb cell. The light source used for this calibration was a Nernst Glower run at 0.5 amps.

The spectral slit width of the Perkin-Elmer monochromator was approximately 30 cm^{-1}. The absorption of atmospheric water vapor and carbon dioxide can be seen in figure 15. No current bias was supplied for the detector.

During our experimental studies, a glass-to-metal seal on the InSb detector broke, thereby exposing the cell itself to atmospheric conditions. Only due to the quick and capable repair work of Professor G. T. Wasserburg was the cell restored to operating condition.

E. The Optical System for Studying Radiation Phenomena Behind Shock Fronts

A versatile optical system for measuring radiation phenomena behind shock fronts has been constructed. This system served to collimate transmitted and emitted radiant energy from the shock tube and to focus this radiation on the slit of a monochromator. Four main divisions of this apparatus may be isolated in relation to their function: 1) light sources and source optics for initial gaseous concentration measurements and absorption studies behind shock fronts, 2) collimating slits for radiation emitted behind shock fronts, 3) condensing optics to focus collimated radiant energy on a monochromator slit or the photocathode of a photomultiplier tube, and 4) monochromator and detector optics. Figure 16 is a photograph of the assembled shock tube facility with the major parts labeled.

Prior to each experiment, a quantitative infrared absorption measurement was made to determine the amount of acetylene present in the shock tube (Section II. C.). The source and chopper assembly were mechanically separated from the monochromator unit in order to permit placing of the shock tube containing the infrared active gas between them (see figure 16). Since this instrument has an effective optical f-number of 4.5, the large (several meters) separation between the source and the monochromator would have resulted in a negligible amount of source energy falling on the monochromator slit. To overcome this difficulty, a spherical mirror (not shown in figure 16) with a 4" diameter and an 8" focal length was placed with its principal focus at the source image immediately adjacent to the exterior of the source optics and chopper housing. This mirror was oriented in such a manner as to direct the resulting parallel beam of radiation through the horizontal pair of windows in the observation section of the shock tube. The radiant energy was subsequently refocussed on the spectrometer slit. The internal optics of the light source and chopper assembly were chosen in such a way that the Perkin-Elmer instrument fuctioned as a single-beam rather than a double-beam spectrometer. A Nernst glower operated with 0.5 amperes current served as light source.

A tungsten light source and a carbon arc were provided so that the absorption of hot gases and solid particles behind shock fronts could be studied. Radiation from the source was focussed with no magnification on the slots of a high-frequency light chopper (see Section III. E.). The radiation was subsequently rendered parallel and directed through the vertical pair of windows in the observation region of the shock tube (see figure 17) and then focussed on a radiation detector.

A collimating slit system has been designed and built to define within the shock tube two uniform geometric regions of observation. These regions are oriented at right angles to each other in a plane normal to the direction of shock propagation. The spacially resolved volumes extend 1 mm along the axis of the tube, 15 mm normal to the axis of the tube in one direction, and 75 mm along the tube diameter. Four sapphire windows are located symmetrically in the wall of the tube at the plane of observation.

The enclosed slit system has been constructed so that all the rays reflected specularly from the inside of the collimating tube are blocked by scatter plates (see figure 18). The slits at either end of the system restrict the radiating solid angle of the gases in the shock tube to two degrees.

The collimating tube for the horizontal pair of windows in the shock tube observation section has been constructed in such a way that it may be removed and returned precisely to its original position. This arrangement permits more energy from the Perkin-Elmer light source to reach the monochromator thermocouple (see Section II. C.).

The condensing optics for the collimated radiation either focussed the radiant energy from the two separate observation regions on the entrance slit of the monochromator or else imaged the radiation from one of the observation regions on the monochromator slit and imaged the other radiating path on a photomultiplier detector.

In the first case, radiation from one of the paths was directed through the high-frequency light chopper (see Section IV) before entering the slit. The divergence angle of the two beams at the monochromator slit was small enough to fall well within the full aperture of the instrument.

The condensing optics (as well as the collimating system and the spectrometer proper) were fully enclosed; major portions of the optical path could then be flushed free of atmospheric water vapor and carbon dioxide. The light-tight cover served to reduce the magnitude of the background scattered light falling on the radiation detectors. A photomultiplier tube and associated circuitry were placed within the framework of the condensing optics for monitoring radiation in the visible region of the spectrum.

The monochromator was mounted adjacent to the condensing optics (see figure 16). The internal construction of the instrument allowed the radiant energy falling on its entrance slit to be focussed either on the thermocouple for gas concentration analysis prior to a test, or to be passed, after dispersion, outside the instrument to an external radiation detector. The InSb infrared radiation detector was mounted in a compartment beside the monochromator in a vertical position and could be cooled easily with liquid nitrogen. The dispersed radiation emerging from the exit slit of the monochromator was focussed with a suitable ellipsoidal mirror on the sensitive area of the detector (see figures 16 and 19).

All mirrors used were front-surface, aluminized, uncoated optics. This was done to extend their useful wavelength range from 0.2 to approximately 6 microns.

A Jefferson Model 969 - 001 - 059 transformer was used to provide power for a 100 watt tungsten strip filament light source. This lamp, operated at a brightness temperature of approximately 2500°K, was used in experiments measuring the absorption of hot gases behind shock fronts. Since the filament was enclosed with a glass envelope, the effective wavelength range over which this lamp could be used extended from approximately 0.35 to about 2 microns.

An Applied Research Laboratory Model SR carbon arc for spectroscopic analysis was adapted for use as a high-energy infrared light source according to a procedure described by Strong (7). The positive electrode was mounted at right angles to the negative electrode; the image of the positive crater then formed an effective blackbody source (see figure 20). National Carbon Co. 8 mm diameter cored projector carbons were used. The arc drew from 8 to 15 amps at 50 to 60 volts and was very stable, especially for the short duration of an experiment (less than a millisecond).

III. AMPLITUDE MODULATING DEVICES FOR SPECTRAL RADIATION IN THE VISIBLE AND INFRARED REGIONS OF THE SPECTRUM

Many applications of shock tube research require an optical device for modulating a beam of radiant energy at a high frequency (see Section IV). In searching for such a device, the optical transmission requirements of the experiment must be borne in mind. Several devices for accomplishing this end are discussed in the following pages.

A. The Kerr-Cell Polarizing Shutter

A Kerr-cell (8) - (16) is an optical shutter that interrupts radiation passing through it by means of its polarizing properties.

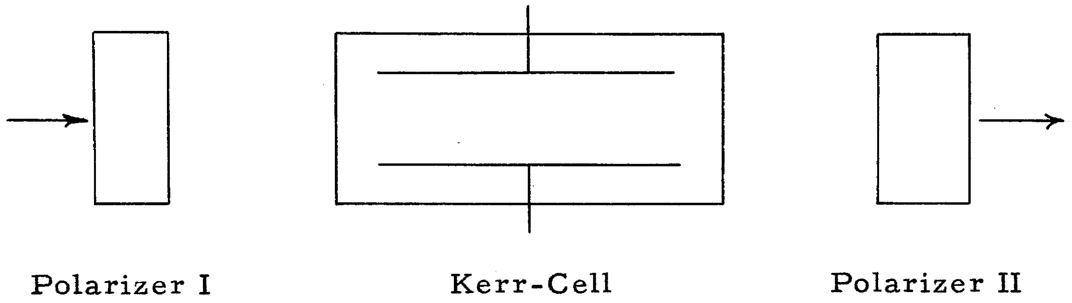

The essential features of a Kerr-cell shutter are illustrated schematically in the preceding sketch. Light emerges from polarizer I after having its electric vector polarized in a specified plane. As the radiation passes through the Kerr-cell with voltage applied to its plates, the plane of polarization is rotated progressively, the radiation going through a sequence of elliptic, circular and elliptic polarizations. The degree of electric vector rotation is a function of the applied voltage, plate length and Kerr-cell material. With a proper combination of these variables, the radiation may be made to emerge from the Kerr-cell plane-polarized, at ninety degrees to its original direction. If polarizer II is crossed with polarizer I, the radiation is then allowed to pass completely through the system. A shutter action may then be obtained by modulating the voltage applied to the Kerr-cell plates in the desired manner.

For a cell with plates of length L cm containing a material with a Kerr constant of K esu with a plate separation of d cm., the transmission, T, through the cell for polarizers crossed at ninety degrees, will be

$$T = \sin^2 \left[(\pi/2)\,(V/300\,d)^2\,(2LK) \right], \tag{1}$$

where V is the voltage applied to the plates and the polarizer losses have been neglected (15). The maximum transmission will be obtained when the argument of the sine term is $\pi/2$, i.e.,

$$V^2\,LK/d^2 = 4.5 \times 10^4 . \tag{2}$$

The Kerr constant for several liquids have been tabulated in Table I. Nitrobenzene has the largest Kerr constant and, therefore, is the most widely used substance for Kerr optical shutters. Using equation 2, it is seen that for a cell of 2 cm length and 0.5 cm plate separation, the "full open" voltage for a nitrobenzene Kerr-cell would be approximately 12,000 volts.

Transmission losses associated with a Kerr-cell, even in the visible region of the spectrum, are generally quite large. The transmission efficiency of a polarizer may be expected to be around 30 per cent (15), giving an overall transmission of roughly 10 per cent. The transmission efficiency of a pair of nicols would be greater than this by about a factor of two.

Of even greater concern is the fact that a 1 cm path of nitrobenzene has practically zero transmission below 4200°A (9), (15) and above 1 micron (18). Figure 21 illustrates this fact. The conclusion, then, is that the Kerr-cell would be suitable as a light modulator for radiation in the visible region of the spectrum, and wholly unsuitable for infrared radiation.

An electro-optic effect is obtained in certain solids, but mechanical difficulties make these materials relatively unsuccessful as shutters (19) - (22). Ammonium dihydrogen phosphate (ADP, $NH_4H_2PO_4$) has an effective Kerr constant of approximately 3×10^{-7} esu (19). The material is brittle, water soluble, and hygroscopic and, hence, very difficult to handle. Since ADP exhibits piezoelectric properties, application of voltage to rotate the plane of polarization in the crystal tends to buckle the bond between the electrodes and the crystal surface. As the result of this effect, the crystals have non-uniform transmission properties. Further difficulties are introduced because the principal optic axis of the crystal must lie along the direction of the applied electric field.

B. The Faraday Polarizing Shutter

A Faraday-cell may be used to modulate a beam of radiant energy in a manner analagous to a Kerr-cell. The Faraday effect involves the phenomenon of magnetorotation of the plane of polarization of certain substances.

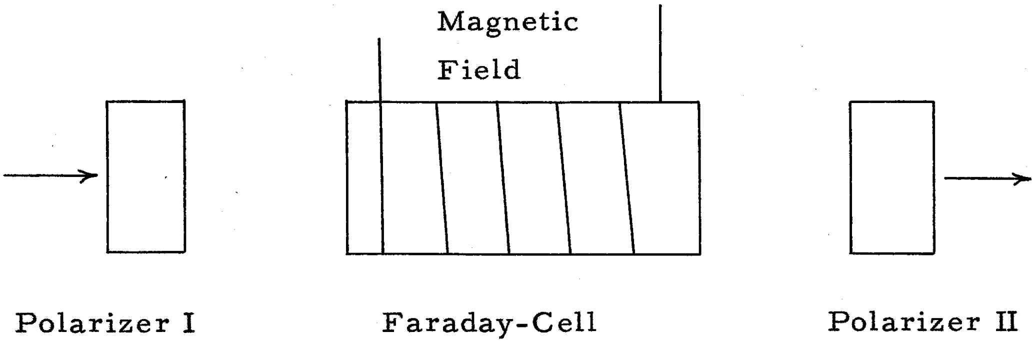

The principal components of a Faraday-cell are pictured schematically above. The operation is similar to a Kerr-cell with the exception that a magnetic field along the optic axis of the cell rotates the plane of polarization. The angular rotation of the electric vector is proportional to the applied field and the cell length for any given material. For a cell of length L cm in an applied field of H gauss, the rotation of the plane of polarization, θ minutes of arc, is (17)

$$\theta = VHL \ . \qquad (3)$$

Where V is the Verdet constant for unit field and cell length.

The Verdet constant for several materials are included in Table II. If a Faraday-cell were to be constructed from a 10 cm quartz rod with polarizers crossed at ninety degrees, it is seen from equation 3 that the applied field must be approximately 33,000 gauss to obtain maximum transmission. This field strength is difficult to obtain for reasonable currents in the cell windings, approximately 3300 ampere turns per cm being required. The maximum transmission through the Faraday cell would be limited to 10 to 20 per cent by the polarizers, as in the case of the Kerr-cell.

C. The Magnetostrictive Shutter

Several mechanical devices for interrupting a beam of light may be considered. The magnetostrictive properties of nickel and high nickel content alloys (24) may be used in a mechanical shutter. Magnetostriction is the term applied to the phenomenon of physical dimension change in ferromagnetic materials under the action of an applied magnetic field. A 45 per cent nickel - 55 per cent iron alloy exhibits a positive magnetostrictive coefficient for all values of the applied field, i. e., the material always expands physically for an increasing magnetic field.

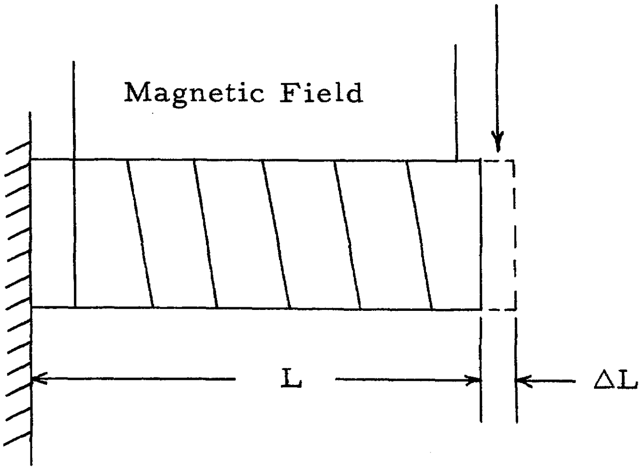

The above figure illustrates the principle of operation of a magnetostrictive shutter. For a material with sound velocity c, the frequency, f, of the fundamental longitudinal vibration is

$$f = c/2L . \tag{4}$$

The 45 Ni-55 Fe alloy has an acoustic velocity in the range of 5000 m/sec. For a frequency of 100 kc, the required length would be 2.5 cm. An applied magnetic field of approximately 1000 gauss leads to a magnetostrictive coefficient of (24)

$$\Delta L/L \simeq 40 \times 10^{-6} . \tag{5}$$

The resulting elongation, ΔL, is then 10^{-4} cm. This change in dimension is much too small to be of practical value for a shutter.

D. The Vibrating Wire Shutter

A vibrating wire, driven by an alternating magnetic field, may also serve as a device for producing amplitude modulation in a beam of radiant energy.

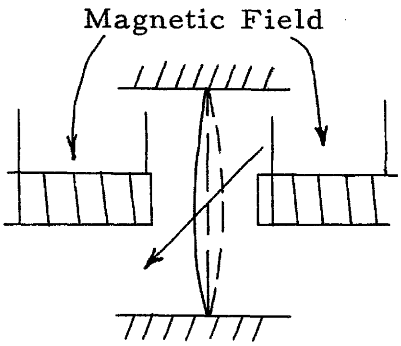

The preceding sketch illustrates schematically the operation of a vibrating-wire shutter. The frequency, f , for the fundamental mode of vibration may be written as

$$f = (1/2L)\sqrt{T/\rho}\ , \qquad (6)$$

where L is the length, T is the axial tension and ρ is the mass per unit length. For a wire of length L ft, tensile strength σ pounds-ft^2, mass density d pound-sec^2-ft^{-4} vibrating at f cycles per sec, equation 6 becomes

$$f = (1/2L)\sqrt{\sigma/d}\ . \qquad (7)$$

A steel wire 0.1 ft long with a maximum allowable stress of 2 x 10^7 pounds per ft^2 would have a fundamental vibration frequency of approximately 6 kc, a figure too low to be of practical importance.

E. The Mechanically Rotated Sector

The problem of adverse optical transmission in a light modulator can be overcome by using a mechanically rotated sector for chopping the radiant energy. A device of this type has been developed for our experimental studies.

The prime mover for the mechanical light chopper was an Airesearch air turbine. This single stage, radial inflow turbine required approximately 3 atmospheres total head to drive it at its maximum speed of 2000 rps. A chopper wheel containing 90 equally spaced radial slots along its periphery was attached to the turbine shaft. The slots had a constant radial separation of 1 mm and a radial height of 5 mm. The slots were 1/4 inch deep in the axial direction, and the chopper wheel diameter was 2 3/4 inches. A maximum chopping frequency of 180 kc was attainable.

IV. OUTLINE OF EXPERIMENTAL PROGRAM

Four distinct types of experiments may be performed with the aid of the optical system discussed in Section II. Figure 22 illustrates the components required to perform a single-double-path experiment (24), (26). By imaging the radiation from one of the regions of observation back on itself, the spherical mirror effectively doubles the radiating path for this section. Since the two regions of observation are coplanar, the physical states of the radiating gases in the two columns defined by the collimating system are the same. For an effective tube diameter of L cm, the spectral radiancy emerging from the single-path will be (27)

$$R_1(\omega) = R^o(\omega) \left[1 - \exp(-P(\omega)pL)\right], \tag{8}$$

measured in units of ergs-cm^{-2}-sec^{-1}- 2π steradian. Here $R^o(\omega)$ is the blackbody radiancy at the wave number ω (cm^{-1}) at the temperature of the radiating gases. $P(\omega)$ is the spectral absorption coefficient in cm^{-1}-atmos^{-1} of a column of radiating gases L cm long at a radiator pressure of p atmos. Correspondingly, the spectral radiancy for the ideal double-path experiment is given by the relation

$$R_2(\omega) = R^o(\omega) \left[1 - \exp(-2P(\omega)pL)\right] . \tag{9}$$

Since it is difficult to make quantitative absolute measurements of the spectral radiancy, it is desirable to use a single-double-path procedure for relative intensity measurements. Quantitative studies may be performed by comparing the detector response for the radiation from the single-path to that for the double-path. By chopping the radiation from one of the paths before directing it to the detector, a single detector may be used to monitor simultaneously the radiant emission from the two paths. The experimentally determined ratio of the spectral radiancies is

$$R_1(\omega)/R_2(\omega) = \left\{1-\exp\left[-P(\omega)pL\right]\right\} \left\{1-\exp\left[-2P(\omega)pL\right]\right\}^{-1} . \qquad (10)$$

Figure 23 illustrates the detector output for a particular experiment. The reactions to be studied by this method must have time-varying rates that are slow compared to the chopper frequency.

It is clear from equation 10 that two types of experimental data may be correlated. If the geometric length L and the absorption coefficient at the wave number ω are known for the chemical species under investigation, then the partial pressure, p, of the radiating species may be followed quantitatively as a function of time. The inverse problem may be investigated, i.e., if the radiating system is not undergoing chemical change then its partial pressure is constant and the spectral absorption coefficient, $P(\omega)$, may be determined as a function of time.

The second type of experiment that can be performed conveniently with the assembled optical system is one whereby the emission from two single-paths is recorded separately on two detectors. The two detectors can be set to monitor radiation at two different wavelength intervals, and time correlation of relative intensities may be made for the resulting data. Harshbarger (1) has used this procedure for the determination of color temperatures.

A modification of the experiment utilizing two radiating paths may be obtained by monitoring the radiation from one path to a given wavelength with one detector, and measuring simultaneous emission and absorption in the other path. Figure 17 shows the optical arrangement for passing chopped, radiant energy through one of the observation regions. It is necessary to modulate the transmitted radiation in order to distinguish it from the internally emitted radiation of the heated gases behind the shock front.

A fourth type of experiment may be performed in which the effects of molecular and solid particle light scattering on the transmitted radiation are determined. The experimental arrangement consists of a detector viewing the chopped, transmitted radiation at right angles to its axis of propagation. Any radiation scattered from the primary beam will have the characteristic chopping frequency modulation and, hence, will be detectable from the continuous background emission.

V. DISCUSSIONS OF THE EXPERIMENTS PERFORMED AND ANALYSES OF THE DATA

The extensive apparatus development program discussed in Sections II and III forms a necessary prerequisite to the completion of an original experimental research program. We have studied the induction time for incipient carbon formation and the activation energy for thermally decomposing acetylene in argon-acetylene mixtures heated by shock waves. All experimental radiation measurements were made by viewing the gases heated by the incident shock wave only. This was done to minimize the effects of turbulence and shock wave-boundary layer interactions which are presumably encountered behind the reflected shock wave.

A. Simultaneous Emission and Absorption Measurements

Radiation measurements in the visible region of the spectrum were made of the simultaneous emission and absorption of transmitted radiant energy by the heated gases and solid particles behind the incident shock front. A 1P28 photomultiplier detector served as receiver. Emission from the acetylene $\Sigma_u^+ - \Sigma_g^+$ parallel band at 3287 cm^{-1} was recorded concurrently using an InSb detector.

The oscilloscope records showed an exponential rate of increase of infrared radiation which reached rapidly a constant value behind the shock wave. There was no measurable decrease in the intensity of the chopped, transmitted, radiation from a tungsten light source (approximately 2500°K brightness temperature) until some time after the infrared radiation had reached its equilibrium value. At this time there was a simultaneous increase in radiation from the heated gases and a decrease in the intensity of the transmitted radiation in the visible region of the spectrum. Figure 24 is a copy of an oscillogram for a simultaneous emission and absorption experiment. The incident shock wave arrived at approximately two divisions from the start of the sweep. The reflected shock wave arrived at approximately 7 1/2 divisions. From these measurements it is clear that the heated gases behind the shock front do not absorb in the visible region of the spectrum until acetylene decomposition occurs. Hence, the absorption is connected with the formation of dissociation products, and not with the thermal excitation of acetylene (28).

It was found experimentally that no detectable radiation could be observed immediately after shock passage anywhere in the spectrum from the visible to approximately 4 microns in the infrared, with the exception of the acetylene fundamental vibration - rotation band centered at 3.04 microns. Special care was taken to observe the spectral regions of the acetylene overtone bands. Furthermore, at the end of the induction time, i.e., the time between the beginning of acetylene radiation (shock arrival) and the onset of visible radiation, emitted energy was seen only in the visible region of the spectrum. However, after the passage of the reflected shock wave through the gases previously heated by the incident shock wave, the temperature rise (approximately two times the temperature behind the incident shock) was sufficient to induce radiation in the entire observable spectral region.

Previous work on carbon formation from acetylene (1), (28) has indicated that the spectral distribution of radiation in the visible region of the spectrum associated with acetylene decomposition is essentially continuous. The present investigations confirm this conclusion qualitatively. For this reason, the emission in the visible region of the spectrum will be assumed to be predominantly due to solid carbon particle radiation. The following analysis may then be applied to obtain an effective activation energy for carbon formation.

The intensity of radiation transmitted through a column of distributed carbon particles L cm in length at a pressure of p_c atmos will be

$$I_t(\omega) = I_o(\omega) \exp\left[-P(\omega) p_c L\right], \tag{11}$$

where $I_o(\omega)$ is the radiation intensity incident on the column of absorbers whose spectral absorption coefficient is $P(\omega)$.

The transmitted energy falling on a radiation detector will then be

$$I_t = \int_{\Delta\omega} I_t(\omega)\, g(\omega)\, d\omega , \tag{12}$$

where $g(\omega)$ is the spectral band-pass function of the detector over the wave number interval $\Delta\omega$. Defining an average value for the absorption coefficient over the interval $\Delta\omega$ as $\overline{P}$ we have, from equations 11 and 12,

$$I_t = \left[\int_{\Delta\omega} I_o(\omega)\, g(\omega)\, d\omega\right] \exp(-\bar{P} p_c L) \ . \tag{13}$$

The integral within the brackets in equation 13 is just the measured incident intensity for no absorption, i. e.,

$$I_o \equiv \int_{\Delta\omega} I_o(\omega)\, g(\omega)\, d\omega \quad . \tag{14}$$

Combining equations 13 and 14 we have the desired relation

$$I_t = I_o \exp(-\bar{P} p_c L) \quad . \tag{15}$$

The time rate of change of carbon particle concentration may be written as

$$dp_c/dt = (-1/PL)\, d[\ln(I_t/I_o)]/dt \ . \tag{16}$$

If the rate of carbon particle formation depends on the acetylene concentration to the order n, then we may assume a rate equation of the Arrhenius form as (29)

$$dp_c/dt = \text{constant}\left[\exp(-E/RT)\right](p_{C_2H_2})^n \ , \tag{17}$$

where E is the activation energy in cal-mole^{-1}, R is the molar gas constant in cal-mole^{-1}-(^{o}K)$^{-1}$ and T is the temperature in ^{o}K. Taking the natural logarithm of both sides of equation 17, we get

$$\ln\left[dp_c/dt\right] = \text{constant} - (E/RT) + \ln(p_{C_2H_2})^n \quad .$$

Differentiating both sides with respect to T and then combining terms we find

$$d\left\{\ln\left[dp_c/dt\right]\right\}/dT = (E/RT^2) + d\left[\ln(p_{C_2H_2})^n\right]/dT\ .$$

Since the operator $d/dT = (-1/T^2)d/d(1/T)$, we obtain

$$(-1/T^2)d\left\{\ln\left[(dp_c/dt)/(p_{C_2H_2})^n\right]\right\}/d(1/T) = E/RT^2\ ,$$

i.e.,

$$E = -\ 2.303\,Rd\left\{\log\left[(dp_c/dt)/(p_{C_2H_2})^n\right]\right\}/d(1/T)\ . \qquad (18)$$

Combining equations 16 and 18 we get

$$E = -\ 2.303\,Rd\left\{\log\left[\left(-1/\overline{P}L(p_{C_2H_2})^n\right)d\left(\ln(I_t/I_o)\right)/dt\right]\right\}/d(1/T)\ .$$

If we assume that the mean value of the absorption coefficient, $\overline{P}$, is independent of temperature in the range considered, we may finally obtain

$$E = -\ 2.303\,Rd\left\{\log\left[\left(-1/(p_{C_2H_2})^n\right)\ d\left(\ln(I_t/I_o)\right)/dt\right]\right\}/d(1/T)\ . \qquad (19)$$

Equation 19 is the basic relation used by us to correlate the data from simultaneous emission and absorption experiments. In figure 23, I_o is the peak-to-peak amplitude of the chopped radiation prior to acetylene excitation and decomposition. The transmitted intensity, I_t, corresponds to the vertical separation of the upper and lower envelopes of the chopped signal. The quantity $\ell n(I_t/I_o)$ was computed from the data for 10 microsecond intervals and then plotted versus the time. In all calculations the laboratory time was converted to particle time by multiplying with the density ratio across the incident shock wave.

In figures 25 and 26 we have plotted the function

$$A_n \equiv -\log \left\{ \left[-1/(p_{C_2H_2})^n \right] d\left[\ell n(I_t/I_o) \right]/dt \right\}$$

as a function of (1/T) for n = 1 and 2, respectively. In these cases the term $d\left[\ell n(I_t/I_o)\right]/dt$ has been evaluated for the initial increase in absorption. Mixtures of 98 per cent of A - 2 per cent of C_2H_2 and 95 per cent of A - 5 per cent of C_2H_2 were used for these experiments. The total pressure behind the incident shock wave ranged from approximately one to five atmospheres, corresponding to temperatures between 1150 and 2000°K. The points for experiments using 95 per cent of A - 5 per cent of C_2H_2 mixtures have been included by adding a constant factor to the respective ordinates in order to adjust the absolute scales of the two sets of data. It is seen that there is no systematic deviation between the data for the two separate mixtures.

According to equation 19 the slope of a straight line going through the data of A_n versus (1/T) should equal E/2.303R . The experimental scatter is such as to prevent an unambiguous choice of the order (with respect to C_2H_2) of the decomposition reaction. However, reference to figures 25 and 26 suggests that the scatter of experimental data in plots of A_n versus $(1/T)$ is somewhat smaller for $n = 1$ with $E = 26$ kcal/mole than for $n = 2$ with $E = 33$ kcal/mole.

It should be noted that the value $n = 1$ does not necessarily indicate a monomolecular decomposition reaction for acetylene. Thus, the decomposition process may well be bimolecular and proceed as the result of collisions between argon and acetylene. The large excess of argon in the argon-acetylene mixtures would make such a process appear to be first order with respect to acetylene, however.

The 1943 paper of Franck-Kamenetsky (30) places the activation energy for acetylene decomposition in the temperature range 400 to 700°C at 29.9 kcal/mole, based on a second order acetylene pressure dependence. Reference to this paper shows that most of the experimental data may be fitted adequately by anything from a first to a third order dependence, although a second order dependence is considered by the author to be most satisfactory.

The activation energies obtained in the work of Aten and Greene (28) fall in this same range, although values of E from 20 to 60 kcal/mole are compatible with the wide scatter of the data presented by these authors.

It is highly doubtful whether data of the type plotted in figures 25 and 26 can be improved sufficiently to allow a more careful prediction of the activation energy than is now possible. It is therefore felt that the values of E quoted here are within ± 10 per cent of the actual value.

B. The Induction Time for Incipient Carbon Formation

Measurements of the induction time for incipient carbon formation from argon-acetylene mixtures were made by recording simultaneously emission from the fundamental vibration-rotation band of acetylene at 3287 cm^{-1} and the spectrally integrated emission from solid carbon particles in the visible region of the spectrum. The spectral resolution in the infrared was approximately 30 cm^{-1}.

The oscillograms showed the familiar rise and levelling off of the infrared radiation behind the incident shock wave. The level of radiation from the infrared did not change following the onset of radiation from the visible region of the spectrum. Figure 27 is a reproduction of an oscilloscope record which illustrates this behavior. The vertical scale for the signal which is proportional to the visible emission has been increased twentyfold over the corresponding scale in figure 24. This change was made in order to allow a more precise determination of the induction time than was possible with the simultaneous emission and absorption experiments.

The induction time is connected in some manner with the time for the molecular vibrations of acetylene to become large enough to induce dissociation. It seems reasonable to postulate that an effective activation energy for acetylene dissociation may be computed from the data. If we assume that at the onset of visible radiation the minimum detectable amount of emission always corresponds to the same amount of carbon being formed for all conditions of temperature and pressure behind the incident shock wave, then we may write (compare equation 17)

$$(\Delta p_c)_{\text{initial}} \simeq \text{const.} = \text{const.}\left[\exp(-E_D/RT)\right](p_{C_2H_2})^n \, \Delta\tau, \qquad (20)$$

where E_D is the activation energy for acetylene dissociation in cal-mole^{-1} and $\Delta\tau$ is the induction time in sec (corrected for the difference between laboratory time and particle time behind the incident shock wave). Taking the natural logarithm of both sides in equation 20 and differentiating with respect to T gives

$$E_D = 2.303\,R\,d\left\{\log\left[(p_{C_2H_2})^n \, \Delta\tau\right]\right\}/d(1/T) . \qquad (21)$$

The experimental data for induction time experiments have been correlated by means of equation 21. In figures 28, 29 and 30 $B_n \equiv \log\left[(p_{C_2H_2})^n \, \Delta\tau\right]$ is plotted as a function of $(1/T)$ for $n = 1$, 1.5 and 2, respectively. Mixtures of 95 per cent of A - 5 per cent of C_2H_2 were used for these experiments. The ranges of total pressures and temperatures behind the incident shock wave were the same as for the data plotted in figures 25 and 26. According to equation 21 the slope of B_n versus $(1/T)$ should equal the quantity $E_D/2.303\,R$. A straight line fit to the data presented in figures 28, 29 and 30 leads to the activation energies for acetylene dissociation of 10, 13 and 16 kcal/mole for $n = 1$, 1.5 and 2 respectively.

No clearcut distinction can be made regarding the correct choice of the reaction order n, although it appears that the scatter for $n = 1$ or 1.5 is somewhat less than for $n = 2$.

The values of E_D correspond closely to the energy of a vibrational quantum in the experimentally observed $\Sigma_n^+ - \Sigma_g^+$ parallel band of acetylene. This observation suggests that the induction time is closely related to the vibrational relaxation time.

The measured shock velocities for the tests in this series of experiments are plotted in figure 31 as a function of initial pressure ratio (p_4/p_1) across the diaphragm and compared with the theoretical prediction in order to illustrate the reproductibility of the experimental apparatus.

C. Impurity and Inert Gas Radiation

Tests were conducted to determine if impurity or inert gas radiation contributed to the measured emission in the pressure and temperature interval considered. Pure argon was heated by shock waves to reproduce the conditions of the previous experiments. Spectral measurements in the visible region of the spectrum revealed no detectable radiation until the temperature behind the incident shock wave exceeded approximately 2400°K. Infrared emission was not observed at all.

D. Molecular and Solid Particle Light Scattering Effects

Further tests were made to determine if molecular or solid particle light scattering contributed to the reduction of the transmitted radiation intensity in the simultaneous emission and absorption experiments. There was no measurable scattering at right angles to the chopped, transmitted radiation in the visible region of the spectrum.

The light source and optical geometry for these tests were identical to those for the emission and absorption experiments. However, the sensitivity of the recording circuitry for the photomultiplier measuring scattered light was ten times greater than that of the circuitry for the primary transmitted radiation intensity. Hence, it is felt that light scattering had no influence on the measurements which were used to estimate effective activation energies.

E. Infrared Detector Time Characteristics

In the experiments discussed so far, the InSb infrared detector has been effectively used only as a device for detecting the arrival of the shock wave at the plane of the observation region. The time behavior of the radiation profile for the acetylene fundamental vibration-rotation band (figures 24 and 27) definitely indicated a type of relaxation effect. If the infrared detector had a time response of approximately 1 microsecond, then a quantitative measure of the vibrational relaxation time would be contained in the data. Unfortunately, the time constant of the cell was nearer to 10 microseconds. This value for the time constant was determined by examining the detector output for various frequencies of applied, chopped radiation. At a modulation frequency of 100 kc, the peak-to-peak amplitude of the signal was reduced to 50 per cent of its value for very low frequencies (several kc), and the square applied waveform was distorted to a sawtooth shape.

Because of this effective band-pass limit for high frequencies, the experimentally observed times for radiation equilibration in the infrared were largely fixed by the nature of the detector and not by the vibrational relaxation of the acetylene molecule. This inherent detector time response also prohibits the determination of the activation energy for acetylene decomposition from simultaneous emission and absorption experiments in the infrared region of the spectrum.

PART II.

AN ANALYSIS OF EQUILIBRIUM INFRARED GAS EMISSIVITIES FOR DIATOMIC MOLECULES BASED ON A JUST-OVERLAPPING ROTATIONAL LINE MODEL

VI. INTRODUCTION

Methods for the theoretical calculation of equilibrium infrared gas emissivities from spectroscopic data have been developed for diatomic and for polyatomic molecules (see references 27 or 31 for a detailed bibliography). An exact prediction of infrared gas emissivities requires detailed knowledge of the rotational line shape in vibration-rotation bands and numerical calculations allowing for partial overlapping between spectral lines. Fortunately, it is sometimes possible to justify well-defined simplifying assumptions which greatly reduce the analytical complexity of the problem. Two extreme cases permit simple analytical solutions, viz., (a) high pressures which smear out the fine structure of vibration-rotation bands, and (b) low pressures which allow a treatment based on a non-overlapping spectral line model (32) - (34).

In the completely overlapped rotational line model, no detailed information about the line shape is required other than the knowledge that the effective widths of the lines exceed their spectral spacing. In the second case, where the rotational lines are assumed to be completely isolated, the line shape is normally chosen to have a dispersion contour at low temperatures and combined Doppler and collision broadening at elevated temperatures.

In the following section infrared emissivity predictions for the molecules CO and $HC\ell$ will be made on the basis of a model which has been used for the description of band contours in absorption at elevated pressures (27) and for the correlation of empirically determined emissivities of water vapor (35). We expect that the just-overlapping line model will have roughly the same range of validity as a rectangular box approximation for vibration-rotation bands, but may possibly be somewhat better for moderate pressures and optical depths.

VII. INTEGRATED LINE AND BAND INTENSITIES

A. Isolated Line Intensities

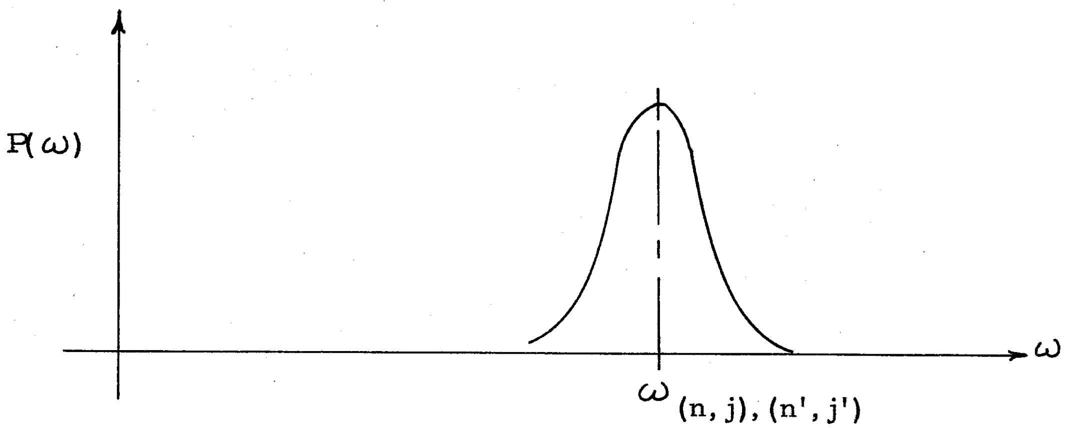

Consider the contour of an isolated rotational line centered at the wave number $\omega_{(n,j),(n',j')}$ in a vibration-rotation band for the vibrational transition n → n' and the rotational transition j → j' (see the preceding sketch). The integrated intensity for the spectral line belonging to a diatomic molecule without Q-branch is defined as (27)

$$S_{(n,j),(n',j')} = \int_{\Delta\omega_{(n,j),(n',j')}} P(\omega)_{(n,j),(n'j')}\, d\omega \tag{1}$$

and is known to be given in first approximation by the following basic expression:

$$S_{(n,j),(n',j')} = (8\pi^3/3hc)\left|R_{n,n'}\right|^2 \left[N_{n,j}/p\right]\left[\omega_{(n,j),(n',j')}/(2j+1)\right] \left[j\,\delta_{j-1,j'} + (j+1)\,\delta_{j+1,j'}\right]\left[1-\exp(-hc\omega_{(n,j),(n',j')}/kT\right], \tag{2}$$

where (n, j) are the vibrational and rotational quantum numbers of the lower state, respectively, (n', j') are the corresponding quantum numbers of the upper state, $N_{n,j}$ is the number of molecules per cm^3 in the lower state, p is the pressure in atmos of the absorbing (or emitting) species, $P(\omega)$ is the spectral absorption coefficient of the line in cm^{-1}-$atmos^{-1}$, $\Delta\omega_{(n,j),(n',j')}$ is the wave number interval over which the absorption coefficient is sensibly different from zero, $|R_{n,n'}|^2$ is the square of the vibrational matrix element for the given transition, and $\delta_{j,j'}$ is the Kronecker delta. The Kronecker delta appears since there are two possible rotational transitions (corresponding to the P- and R-branches) associated with every value of the quantum number j (viz., $j \pm 1$).

From statistical mechanics we may write the ratio of the number of molecules per cm^3 in the state (n, j) to the total number of molecules per cm^3, N_T, as (36)

$$N_{n,j}/N_T = \left[(2j+1)/Q\right] \exp(-E_{n,j}/kT) \qquad (3)$$

where Q is the total internal partition function and $E_{n,j}$ is the energy of the state (n, j). Both Q and $E_{n,j}$ are evaluated with respect to a fixed reference energy level which is usually chosen to be the state of lowest energy.

If we substitute the value of $N_{n,j}$ from equation 3 into equation 2, we obtain

$$S_{(n,j),(n',j')} = (8\pi^3/3hc)\left|R_{n,n'}\right|^2 (N_T/p)\left[\omega_{(n,j),(n',j')}/Q\right]$$
$$\left[\exp(-E_{n,j}/kT)\right]\left[1-\exp(-hc\,\omega_{(n,j),(n',j')}/kT)\right]$$
$$\left[j\delta_{j-1,j'} + (j+1)\,\delta_{j+1,j'}\right]. \tag{4}$$

The variation with temperature and pressure of the number of molecules per unit volume at unit pressure may be obtained by noting that, for ideal gases, the number density varies inversely with the temperature. Hence

$$N_T/p = 273.1\ N_o/T \tag{5}$$

where N_o is the total number of molecules per cm^3 at S.T.P. Combining equations 4 and 5 we get

$$S_{(n,j),(n',j')} = (8\pi^3/3hc)\left|R_{n,n'}\right|^2 (273.1\ N_o/T)\left[\omega_{(n,j),(n',j')}/Q\right]$$
$$\left[\exp(-E_{n,j}/kT)\right]\left[1-\exp(-hc\,\omega_{(n,j),(n',j')}/kT)\right]$$
$$\left[j\delta_{j-1,j'} + (j+1)\,\delta_{j+1,j'}\right]. \tag{6}$$

B. Approximate Line and Band Intensities

In the temperature range of 300 to 3000°K, most diatomic molecules have appreciable contributions to their equilibrium infrared gas emissivity only in the region of the fundamental $(n \rightarrow n+1)$

vibration-rotation bands and the first overtone (n $\rightarrow$ n+2) bands. Since the integrated intensities for entire vibration-rotation bands are often available in the published literature, it is convenient to express the intensity per line in terms of the band intensity. This connection can be made relatively easily when certain approximations are introduced into equation 6.

If we neglect the anharmonic terms for the vibrational energy and the interaction terms between vibrational and rotational energy, the total energy of a state for a given set of quantum numbers may be written as the sum of a rotational energy and a vibrational energy. The rotational energy levels for a diatomic molecule are, in first approximation (37),

$$E_j = hcB_e j(j+1), \quad j = 0, 1, 2, \cdots, \qquad (7)$$

where B_e is the equilibrium rotational constant in cm^{-1} defined as $B_e = h/8\pi^2 cI_e$, I_e being the equilibrium moment of inertia of the molecule in units of $g\text{-}cm^2$, and j is the rotational quantum number. We may express the vibrational energy levels as

$$E_n = (n+\tfrac{1}{2})\, hc\,\omega_e, \quad n = 0, 1, 2, \cdots, \qquad (8)$$

where ω_e is the classical transition wave number for a harmonic oscillator in cm^{-1}.

The total internal partition function, Q, may be written as the product of the vibrational and rotational partition functions Q_V and Q_R. The statistical weight for a vibrational energy level is unity and, therefore, the vibrational partition function is given by

$$Q_V = \sum_{n=0}^{\infty} \exp(-E_n/kT) = \sum_{n=0}^{\infty} \exp\left[-(n+\tfrac{1}{2})\,hc\,\omega_e/kT\right] . \qquad (9)$$

It is readily shown (36) that the sum in equation 9 reduces to

$$Q_V = \exp(-hc\,\omega_e/2kT)\left[1-\exp(-hc\,\omega_e/kT)\right]^{-1} . \qquad (10)$$

The statistical weight for a rotational energy level is (2j+1) and, hence, the rotational partition function takes the form

$$Q_R = \sum_{j=0}^{\infty} (2j+1)\exp(-E_j/kT) = \sum_{j=0}^{\infty} (2j+1)\exp\left[-hcB_e j(j+1)/kT\right]. \qquad (11)$$

This sum may be evaluated by use of the Euler-Maclaurin summation formula to give

$$Q_R = kT/hcB_e . \qquad (12)$$

In equation 6, $\omega_{(n,j),(n',j')}$ may be replaced, approximately, by the wave number at the center of the band, $\omega^{*}_{n,n'}$, and the energy level of the lower state may be expressed as

$$E_{n,j} = E_n + E_j . \qquad (13)$$

Making the approximations specified in equations 7 to 11, it is seen that equation 6 takes the form

$$S_{(n,j),(n',j')} = (8\pi^3/3hc)\,\omega^{*}_{n,n'}\,(273.1\ N_o/T)\,\left|R_{n,n'}\right|^2$$

$$\left[1-\exp(-hc\,\omega^{*}_{n,n'}/kT)\right]\left[1-\exp(-hc\,\omega_e/kT)\right]$$

$$\left[\exp\left(-nhc\,\omega_e/kT\right)\right]$$

$$\left[j\delta_{j-1,j} + (j+1)\,\delta_{j+1,j'}\right]\left[\exp\left(-hcB_e j(j+1)/kT\right)\right]\left[Q_R\right]^{-1}. \quad (14)$$

The integrated intensity for the vibration-rotation band corresponding to the transition n → n' is given by

$$\alpha_{n,n'} = \sum_{j=0}^{\infty}\sum_{j'=0}^{\infty} S_{(n,j),(n',j')}$$

$$\simeq (8\pi^3/3hc)\,\omega^{*}_{n,n'}\,(273.1\ N_o/T)\,\left|R_{n,n'}\right|^2$$

$$\left[1 - \exp(-hc\,\omega^{*}_{n,n'}/kT)\right]\left[1 - \exp(-hc\,\omega_e/kT)\right]$$

$$\left[\exp\left(-nhc\,\omega_e/kT\right)\right]\left[Q_R\right]^{-1}$$

$$\sum_{j=0}^{\infty}\left\{\exp\left[-hcB_e j(j+1)/kT\right]\right\}\sum_{j'}\left\{j\delta_{j-1,j'}+(j+1)\delta_{j+1,j'}\right\}. \quad (15)$$

In equation 15,

$$\sum_{j'=0}^{\infty}\left\{j\delta_{j-1,j'} + (j+1)\,\delta_{j+1,j'}\right\} = 2j+1\ ,$$

and we get, finally,

$$\alpha_{n,n'} \simeq (8\pi^3/3hc)\omega^*_{n,n'}\,(273.1\ N_o/T)\left|R_{n,n'}\right|^2$$
$$\left[1 - \exp(-hc\omega^*_{n,n'}/kT)\right]\left[1 - \exp(-hc\,\omega_e/kT)\right]$$
$$\left[\exp(-nhc\,\omega_e/kT)\right] \qquad (16)$$

where we have used the definition for the rotational partition function given in equation 11.

When we speak of the fundamental vibration-rotation bands we refer to that collection of bands localized in a spectral region characterized by the transitions $n \rightarrow n+1$. Similarly, the first overtone bands refer to the collection of bands characterized by the transitions $n \rightarrow n+2$. If vibration-rotation interactions and anharmonicity terms are neglected, band centers will be located at integral multiples of the classical wave number, ω_e, and all the transitions of the form $n \rightarrow n+m$, where m is an integer, will be centered at $m\omega_e$.

The experimentally determined integrated intensities for the fundamental and first overtone bands include the contributions of all bands with changes in the vibrational quantum numbers $n \longrightarrow n+1$ and $n \rightarrow n+2$, respectively, at room temperature. In order to make predictions for emissivities at elevated temperatures, it is necessary to estimate the temperature dependence of the integrated intensities. To the order of approximation that the vibration-rotation interactions and anharmonicities are negligible, we may use the expression for the harmonic oscillator matrix element for the case m = 1. This gives us (27)

$$\left|R_{n,\,n+1}\right|^2 = (\mu_1^2/2\alpha)(n+1) \qquad (17)$$

where μ_1 is the linear term in the dipole moment expansion of the molecule, and $\alpha = (4\pi^2 m_r c\,\omega_e/h)$, m_r being the reduced mass of the molecule. If we let $\omega^*_{n,\,n+1} \simeq \omega_e$, we may write

$$\sum_{n=0}^{\infty} \alpha_{n,\,n+1} \simeq (8\pi^3/3hc)(273.1\ N_o/T)\omega_e$$

$$\left[1 - \exp(-hc\,\omega_e/kT)\right]^2$$

$$(\mu_1^2/2\alpha) \sum_{n=0}^{\infty} (n+1)\exp(-nhc\,\omega_e/kT)\ .$$

But, since

$$\sum_{n=0}^{\infty} (n+1)\exp(-nhc\,\omega_e/kT) = \left[1 - \exp(-hc\quad {}_e/kT)\right]^{-2}\ ,$$

we obtain

$$\sum_{n=0}^{\infty} \alpha_{n,\,n+1} \simeq (8\pi^3/3hc)(273.1\ N_o\,\omega_e/T)\,(\mu_1^2/2\alpha)\ . \qquad (18)$$

Crawford and Dinsmore (38) have computed the correction terms to equation 18 when vibration-rotation interactions are considered.

It is seen from equation 16 that for sufficiently low values of the temperature, the only contribution to the integrated intensity of the fundamental comes from the transition (0, 1), i.e.,

$$\sum_{n=0}^{\infty} \alpha_{n,n+1} \approx \alpha_{0,1} . \tag{19}$$

For higher values of the temperature, more bands become populated in the region of the fundamental, and anharmonicities as well as vibration-rotation interaction terms become relatively more important. One effect of the interactions is the shift of the line centers for one band with respect to another. This shift is pictured schematically in the following sketch.

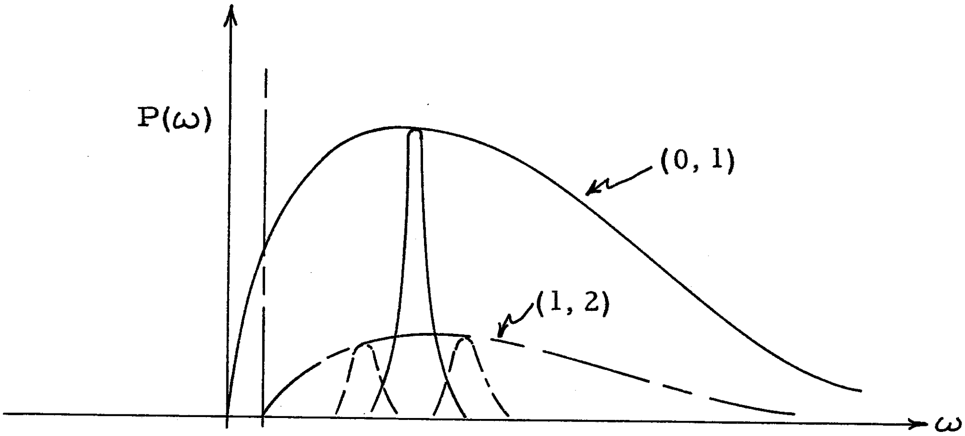

The above sketch shows that two adjacent, just-overlapped, lines in the (0, 1) band may be straddled by the corresponding lines in the (1, 2) band. Since it is the intent in the present analysis to predict emissivities for a just-overlapping line model, it is seen that extensive overlapping would complicate the problem. In fact, the box method, i.e., the completely overlapping line treatment, would be preferable if the individual lines lose their identity. For this reason, we will consider only the temperature range for which the following approximations hold:

$$\sum_{n=0}^{\infty} \alpha_{n,n+1} \approx \alpha_{0,1}$$

and (20)

$$\sum_{n=0}^{\infty} \alpha_{n,n+2} \approx \alpha_{0,2} ,$$

i.e., we will consider only those transitions whose lower state vibrational quantum number is $n = 0$.

Using the approximations given in equation 20, we may rewrite equation 14 as

$$S_{(0,j),(n',j')} \approx \alpha_{0,n'}\left[j\delta_{j-1,j'} + (j+1)\,\delta_{j+1,j'}\right] \left\{\exp\left[-hcB_e j(j+1)/kT\right]\right\}\left\{hcB_e/kT\right\} . \tag{21}$$

Since the quantity hcB_e/k in the rotational population factor is of the order of unity for most diatomic molecules, the exponential in equation 21 will not become negligibly small for temperatures of the order of a thousand degrees until the rotational quantum number j is approximately equal to 40. This means that at elevated temperatures large numbers of lines have appreciable intensities, and we are justified in making the approximations

$$j(j+1) \approx j^2$$

and

$$j+1 \approx j \ .$$

With these approximations, equation 21 becomes

$$S_{(0,j),(n',j')} \approx \alpha_{0,n'} (jhcB_e/kT) \left[\exp(-hcB_e j^2/kT) \right], \tag{22}$$

where $S_{(0,j),(n',j')}$ is the line intensity for either of the transitions $j \rightarrow j \pm 1$.

C. Average Absorption Coefficients

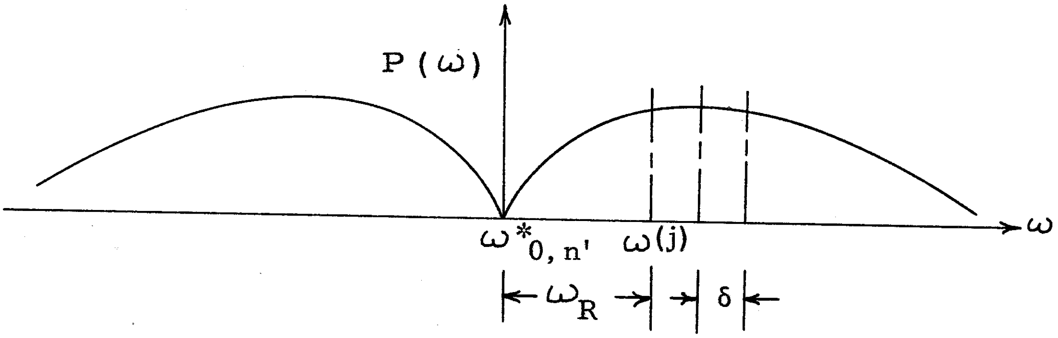

In the above sketch for the spectral distribution of rotational lines in a vibration-rotation band having only an R- and a P-branch (37), the separation of the line corresponding to the transition $j \rightarrow j - 1$ from the band center, $\omega^*_{0,n'}$, is ω_R. To the approximation that the rotational and vibrational energy levels are separable, this spacing is given by

$$\omega_R = (1/hc)\left[E_j - E_{j-1}\right]$$

$$= B_e j(j+1) - B_e (j-1)j$$

or

$$\omega_R = 2B_e j \qquad (23)$$

where we have used the energy relation of equation 7. From equation 23 it is seen that the spacing between rotational lines is given by

$$\delta = \omega_R(j) - \omega_R(j-1)$$

$$= 2B_e \, . \qquad (24)$$

We say that the rotational lines are just-overlapping when the effective width of the individual lines will be equal to the line spacing δ . For this situation an effective average absorption coefficient for a rotational line in the vibration-rotation band under consideration may be defined as

$$\overline{P}_{(0,j),(n',j')} = S_{(0,j),(n',j')}/\delta \, . \qquad (25)$$

The present formulation allows the absorption coefficient to vary over the band, without requiring a knowledge of the detailed contour of the individual lines. In effect, each line is replaced by a box of width δ cm^{-1} and height $\overline{P}_{(0,j),(n',j')}$ cm^{-1}-atmos^{-1} .

Making the substitution

$$\gamma \equiv hcB_e/kT \ , \tag{27}$$

and combining equations 22 to 25, we get

$$\overline{P}_{(0,j),(n',j')} = \alpha_{0,n'} (\omega_R/4B_e^2)\gamma\left[\exp(-\gamma\omega_R^2/4B_e^2)\right] . \tag{28}$$

The expression for the local average absorption coefficient given in equation 28 may be compared with the experimentally determined values for CO reported by Penner and Weber (39). The necessary spectroscopic constants for CO (and HCℓ) are given in Table III (27), (40) and (41). The values of the physical constants used for calculations are also included in Table III. The absorption coefficient $\overline{P}_{(0,j),(1,j')}$ for the fundamental vibration-rotation band, and the absorption coefficient $\overline{P}_{(0,j),(2,j')}$ for the first overtone band of CO at 300°K are plotted in figures 32 and 33, respectively, and compared with the experimental results (39). The variable $\omega = \omega_R + \omega^*_{0,n'}$ (see the sketch following equation 22) has been used. The predicted band contours are symmetric since no vibration-rotation interaction terms have been considered. The fit to the experimentally determined curves is seen to be good; for this reason, emissivity predictions using the just-overlapping rotational line model are expected to yield acceptable results for properly chosen conditions of pressure and optical depth.

VIII. THE ENGINEERING EMISSIVITY

A. Integral Representation

The engineering emissivity, ϵ, of a group of distributed radiators is defined as

$$\epsilon = \left\{ \int_0^\infty R^\circ(\omega) \left[1 - \exp(-P(\omega)X)\right] d\omega \right\} \Big/ \left\{ \int_0^\infty R^\circ(\omega) d\omega \right\} \tag{29}$$

where $R^\circ(\omega)$ is the blackbody radiancy and X is the optical depth of the radiators. The integral in the denominator has the value

$$\int_0^\infty R^\circ(\omega) d\omega = \sigma T^4 \tag{30}$$

where σ is the Stefan-Boltzmann constant in units of erg-cm^{-2}-sec^{-1}-$(^\circ K)^{-4}$. If we consider the emissivity of a single vibration-rotation band centered at $\omega^*_{0,n'}$, with two equal branches, then ϵ takes the form

$$\epsilon = 2(\bar{R}^\circ / \sigma T^4) \int_{\omega^*_{0,n'}}^\infty \left[1 - \exp(-P|\omega - \omega^*_{0,n'}| X)\right] d\omega$$

where $\bar{R}^\circ$ is the average value of the blackbody radiancy which is conveniently evaluated at the band center. Making the substitution $\omega_R = \omega - \omega^*_{0,n'}$, we get

$$\epsilon = 2(\bar{R}^\circ / \sigma T^4) \int_0^\infty \left[1 - \exp(-P(\omega_R) X)\right] d\omega_R . \tag{31}$$

The value of $P(\omega_R)$ in equation 31 is given by equation 28. Making the indicated substitution and letting

$$\xi = \sqrt{\gamma}\,\omega_R/2B_e \tag{32}$$

we get

$$\epsilon = 2(\bar{R}^o/\sigma T^4)(2B_e/\sqrt{\gamma}) \int_0^\infty \left\{1-\exp\left[-(\alpha_{0,n'}X\sqrt{\gamma}/2B_e)\,\xi\exp(-\xi^2)\right]\right\} d\xi$$

or

$$\epsilon = 4(\bar{R}^o/\sigma T^4)(\sqrt{\gamma}\,kT/hc) \int_0^\infty \left\{1-\exp\left[-K\xi\exp(-\xi^2)\right]\right\} d\xi \tag{33}$$

where

$$K = \alpha_{0,n'}X\sqrt{\gamma}\,/2B_e \tag{34}$$

and use has been made of equation 27.

Equation 33 is the basic formulation used for the evaluation of equilibrium infrared gas emissivities for the just-overlapping line model. For very small values of the parameter K, the integral is conveniently evaluated by expanding the exponential and keeping only the linear terms. Denoting the integral by I, we have in this case

$$I \equiv \int_0^\infty \left\{1-\exp\left[-K\xi\exp(-\xi^2)\right]\right\} d\xi$$

$$\simeq \int_0^\infty K\xi\exp(-\xi^2)d\xi = K/2, \quad K \ll 1 . \tag{35}$$

Combining equations 33 to 35 we get

$$\epsilon = (\bar{R}^o/\sigma T^4)\,\alpha_{0,n'}X, \quad K << 1 . \tag{36}$$

It should be noted that the form of ϵ given in equation (36) can be derived from the basic definition of ϵ given in equation 29 for $P(\omega)X << 1$, viz.,

$$\epsilon \simeq (\bar{R}^o/\sigma T^4) \int_0^\infty P(\omega)X d\omega$$

$$= (\bar{R}^o/\sigma T^4)\alpha X, \quad P(\omega)X << 1 .$$

B. Infinite Series Representation

The integral, I, may be evaluated in terms of an infinite summation of known functions. We note that

$$\exp\left[-K\xi\exp(-\xi^2)\right] = \sum_{n=0}^{\infty}\left[(-1)^n/(n)!\right]K^n\xi^n\exp(-n\xi^2)$$

and

$$1-\exp\left[-K\xi\exp(-\xi^2)\right] = \sum_{n=1}^{\infty}\left[(-1)^{n+1}/(n)!\right]K^n\xi^n\exp(-n\xi^2) . \tag{37}$$

Therefore,

$$I = \sum_{n=1}^{\infty}\left[(-1)^{n+1}/(n)!\right]K^n\int_0^\infty \xi^n\exp(-n\xi^2)\,d\xi . \tag{38}$$

Let

$$I_n \equiv \int_0^\infty \xi^n \exp(-n\xi^2)d\xi \tag{39}$$

and make the change of variable

$$\xi = \sqrt{t/n}\ .$$

Then

$$I_n = \int_0^\infty (t/n)^{n/2} \left[\exp(-t)\right] (1/2\sqrt{nt})\, dt$$

$$= (1/n)^{(n+1)/2}\ (1/2) \int_0^\infty (t)^{(n-1)/2} \exp(-t)dt$$

or

$$I_n = (1/2)\ n^{-(n+1)/2}\ \Gamma\left[(n+1)/2\right] \tag{40}$$

where $\Gamma(z)$ is the gamma function of argument z (42). Combining equations 38 to 40 we get

$$I = (1/2) \sum_{n=1}^{\infty} \left[(-1)^{n+1}/(n)!\right] K^n\ n^{-(n+1)/2}\ \Gamma\left[(n+1)/2\right]\ . \tag{41}$$

The expression for I in equation 41 is suitable for numerical evaluation for reasonably small values of K, i.e., $K \leq 7$. The first nine terms of the series give the polynomial expression

$$I \simeq 0.500\left\{K+18.5\text{x}10^{-3}\,K^{3}+13.3\text{x}10^{-5}\,K^{5}+4.95\text{x}10^{-7}\,K^{7}+1.12\text{x}10^{-9}\,K^{9}\right\}$$
$$-\,0.887\left\{8.84\text{x}10^{-2}\,K^{2}+9.76\text{x}10^{-4}\,K^{4}+4.92\text{x}10^{-6}\,K^{6}+1.41\text{x}10^{-8}\,K^{8}\right\}\,. \quad (42)$$

It is interesting to note that the terms in the sum of equation 41 approach asymptotically the terms in a series tabulated by Ladenburg (44). This may be seen by using the Stirling approximation for the gamma function for large values of the argument (43), viz.

$$\Gamma(z) \simeq \sqrt{2\pi}\,\left(z^{z-\frac{1}{2}}\right)\exp(-z)\,.$$

Substitution for $\Gamma(z)$ in the nth term, T_n, in equation 41 then shows that

$$T_n^{*} = \lim_{n\to\infty}\left(T_n\right) = \sqrt{\pi/2}\,\left[(-1)^{n+1}\,(K/\sqrt{2e}\,)^{n}\Big/ n^{1/2}(n)!\right]\,. \quad (43)$$

The sum $\sum_{n=1}^{\infty}\left(T_n^{*}\right)$ arises in the treatment of pure Doppler broadening for individual spectral lines and has been tabulated by Ladenburg (44). However, numerical comparison of Ladenburg's results for $\sum_{n=1}^{\infty}\left(T_n^{*}\right)$ with I given by equation 41 shows that I differs appreciably from $\sum_{n=1}^{\infty}\left(T_n^{*}\right)$ depending on the value of K, agreement being actually better for small than for large values of K. This discrepancy is the result of the fact that the value of I actually depends on the first few terms of the rapidly oscillating series for all values of K. Exact asymptotic limits are readily obtained for I when K goes to zero or becomes very large.

Applications to specific molecules in the following text will show that values of K of $\mathcal{O}(100)$ are encountered in practice and, therefore, it is desirable to obtain an exact evaluation of I if comparisons with experimental data are to be made.

C. Numerical Integration of the Exact Expression for I

The Datatron digital computer model 204 was used to evaluate I; a Simpson's Rule program was employed. The results of these computations are tabulated in Table IV and plotted in figures 34 and 35.

The values of I for $0.1 \leq K \leq 1.0$ have been computed from the approximate form given in equation 42 and plotted in figure 36.

For values of $K < 0.1$, the linear form of equation 35 is adequate.

D. CO and HCℓ Emissivity Predictions

Predictions of the engineering emissivity, ϵ , may now be made for specific molecules. In particular, calculations for the molecules CO and HCℓ will be given here.

The blackbody function $\overline{R}^{o}$ in equation 33 is to be evaluated at the band center for the fundamental and first overtone of both molecules. The band centers do not actually fall at multiples of the classical wave number ω_e, but are slightly shifted in proportion to the magnitude of the anharmonic interactions. For the purposes of these calculations, the actual band centers, i.e., the location of the rotationless transitions, will be used. The symbol ω^{*}_{F} will be used to designate the actual band center for the fundamental vibration-rotation band, while ω^{*}_{O} will be used to designate the location of the first overtone band center.

The band centers may be calculated from the term values for an anharmonic vibrating rotator (37)

$$E_{nj}/hc = \omega_e(n+\tfrac{1}{2}) - \omega_e X_e (n+\tfrac{1}{2})^2 + \omega_e y_e (n+\tfrac{1}{2})^3$$

$$+ B_e j(j+1) - \alpha_e(n+\tfrac{1}{2})j(j+1) - D_e j^2(j+1)^2 \ . \tag{44}$$

Thus

$$\left.\begin{aligned} \omega^*_F &= E_{1,0}/hc - E_{0,0}/hc \ , \\ \text{and} \qquad & \\ \omega^*_O &= E_{2,0}/hc - E_{0,0}/hc \ . \end{aligned}\right\} \tag{45}$$

The values of ω^*_F and ω^*_O for CO and HCℓ are included in Table III.

In equation 33 let

$$A \equiv 4\,(\bar{R}^o/\sigma T^4)(\sqrt{\gamma}\, kT/hc)$$

$$= 8\pi hc^2 \omega^{*3} \left[\exp(hc\omega^*/kT)-1\right]^{-1} (\sigma T^{7/2})^{-1}$$

$$\sqrt{B_e k/hc}$$

or

$$A = 2.199\,\omega^{*3}(\sqrt{B_e}/T^{7/2})\left[\exp(1.439\,\omega^*/T)-1\right]^{-1} \ . \tag{46}$$

The values of A for the fundamental and first overtone of CO and HCℓ are given in Table V for various temperatures.

The parameter K given in equation 34 becomes

$$K = (\alpha_{0,n'} X/2B_e)\sqrt{hcB_e/kT}$$

or

$$K/X = 0.600\,(\alpha_{0,n'}/\sqrt{B_e T})\ . \qquad (47)$$

The quantity K/X is tabulated in Table V for the same cases as the quantity A.

The engineering emissivity, ϵ, is now obtained for any optical depth, X, as the product of the quantities A and I. For the CO molecule, ϵ has been computed for X = 0.3, 1, 2, and 10 cm-atm, while ϵ has been computed for the HCℓ molecule for X = 1, 5 and 20 cm-atm. The results are plotted in figures 37 to 43, respectively. For comparison purposes, the limiting emissivities ϵ_L (in which the spectrum of an entire vibration-rotation band is approximated by a box defined by an average effective absorption coefficient and an average effective bandwidth) and ϵ_{NO} (obtained from the model of non-overlapping rotational lines in which the rotation lines are assumed to have a dispersion contour) have been included in figures 37 to 43. The emissivity contributions from the fundamental and first overtone bands have been added to give the total engineering emissivity plotted in the figures.

E. Comparison of Emissivity Predictions for Several Different Models

In figures 37 to 40 the experimental data of Ullrich for CO have been included. It is seen that the temperature dependence of the box approximation (limiting emissivity) and the just-overlapping line approximation are nearly identical, the latter providing a better fit to the experimental data at the largest optical depth considered. It is to be expected that the emissivities obtained from the just-overlapping line model will be close to those derived from the box approximation. The just-overlapping line model is, however, less artificial since it does not involve an arbitrary definition for the "effective band-width". In all cases considered, the emissivities predicted from the non-overlapping line model consistently underestimate the observed emissivity. For the highest temperatures, the experimentally determined emissivity values are believed to be excessively high because of the formation of CO_2 .

REFERENCES

1. Harshbarger, F.: Ph.D. Thesis, California Institute of Technology, (June, 1957).

2. Bennett, E. N.: Ae.E. Thesis, California Institute of Technology, (June, 1956).

3. Rabinowicz, J., Jessey, M. E., and Bartsch, C. A.: J. Appl. Phys. 27, 97 (1956).

4. Lukasiewicz, J.: "Shock Tube Theory and Applications," NAEC Report 15, Ottawa,(1952).

5. Innes, K. K.: J. Chem. Phys., 22, 863 (1954).

6. Perkin-Elmer Instruction Manual, Vol. 1, Perkin-Elmer Corp., Norwalk, Conn., (1952).

7. Strong, J.: Procedures in Experimental Physics, Ch. 9, Prentice-Hall, Inc., Englewood Cliffs, N. J., (1956).

8. Kingsbury, E. F.: Rev. Sci. Instr., 1, 22 (1930).

9. Beams, J. W.: Rev. Sci. Instr., 1, 780 (1930).

10. White, H. J.: Rev. Sci. Instr., 6, 22 (1935).

11. Washburn, H. W.: Phys. Rev., 39, 688 (1932).

12. Dunnington, F. G.: Phys. Rev., 38, 1506 (1931).

13. Brown, F. L. and Beams, Jr., J. W.: J. Opt. Soc. Am., 11, 11 (1925).

14. Beams, J. W.: J. Opt. Soc. Am., 13, 597 (1926).

15. Zarem, A. M., Marshall, F. R. and Poole, F. L.: Elec. Eng., 68, 282 (1949).

16. Zarem, A. M. and Marshall, F. R.: Rev. Sci. Instr., 21, 514 (1950).

17. Jenkins, F. A. and White, H. E.: Fundamentals of Physical Optics, Ch. 19, McGraw-Hill Book Co., Inc., New York (1937).

18. Goblentz, W. W.: Investigations of Infra-Red Spectra, pp. 86, 251, Carnegie Institution of Washington, Washington, (1905).

19. Carpenter, R.: J. Opt. Soc. Am., 40, 225 (1950).

20. Gunter, Jr., R. C.: J. Opt. Soc. Am. 38, 419 (1948).

21. Billings, B. H.: J. Opt. Soc. Am., 39, 797 (1949).

22. Billings, B. H.: J. Opt. Soc. Am., 39, 802 (1949).

23. Monk, G. S.: Light; Principles and Experiments, Appendix, McGraw-Hill Book Co., Inc., New York (1937).

24. The International Nickel Co., Inc., Iron-Nickel Alloys for Magnetic Purposes, Sect. 8, data sheet B, New York, (1949).

25. Penner, S. S. and Bjornerud, E. K.: J. Chem. Phys., 23, 143 (1955).

26. Hooker, W., Lapp, M., Weber, D., and Penner, S. S.: J. Chem. Phys., 25, 1087 (1956).

27. See, for example JP-202 Class Notes, California Institute of Technology., Pasadena.

28. Aten, C. F. and Greene, E. F.: Faraday Soc. Disc., 22, 162 (1956).

29. Penner, S. S.: Chemical Reactions in Flow Systems, Chap. 1, Butterworths Scientific Publications, London, (1955).

30. Franck-Kamenetsky: Acta Physicochim., 18, 148 (1943).

31. Penner, S. S. and Thomson, A.: "Determination of Equilibrium Infrared Emissivities from Spectroscopic Data," Technical Report No. 25, Contract Nonr-220(03), NR 015-401, California Institute of Technology, Pasadena, (1957).

32. Penner, S. S.: J. Appl. Phys., 21, 685 (1950).

33. Penner, S. S.: J. Appl. Mech., 18, 53 (1951).

34. Penner, S. S.: J. Appl. Phys., 23 , 825 (1952).

35. Thomson, A.: "An Approximate Analytic Expression for the Engineering Emissivity of Water Vapor II," Technical Note No. 5, Contract AF 04(645)-24, Gruen Applied Science Labs., Inc., Pasadena (1957).

36. Mayer, J. E. and Mayer, M. G.: Statistical Mechanics, Chap. 6, John Wiley and Sons, Inc., New York, (1950).

37. Herzberg, G., Spectra of Diatomic Molecules, Chap. 3, D. Van Nostrand Co., Inc., Princeton, (1955).

38. Crawford, B. L., Jr. and Dinsmore, H. L.: J. Chem. Phys., 18, 983, 1682 (1950).

39. Penner, S. S. and Weber, D.: J. Chem. Phys., 19, 807 (1951).

40. Herzberg, G.: loc. cit., appendix.

41. Plyler, E. K., Benedict, W. S. and Silverman, S.: J. Chem. Phys., 20, 175 (1952).

42. Dwight, H. B.: Tables of Integrals, The Macmillan Co., New York (1953).

43. Morse, P. M. and Feshbach, H.: Methods of Theoretical Physics, Chap. 4, McGraw-Hill Book Co., Inc., New York, (1953).

44. Ladenburg, R.: Z. Physik, 65, 200 (1930).

TABLE I. Kerr constants for several chemical compounds.

Material	Kerr constant (esu)	Reference
Nitrobenzene ($C_6H_5NO_2$)	400×10^{-7} 346×10^{-7}	15 9
Nitrotoluene ($NO_2C_6H_4CH_3$)	122×10^{-7}	9
Acetone (C_3H_6O)	16×10^{-7}	15
Carbon disulphide (CS_2)	3.36×10^{-7} 3.21×10^{-7} 3.6×10^{-7}	9 17 15
Benzene (C_6H_6)	$.60 \times 10^{-7}$	9

TABLE II. Verdet constants for several chemical compounds.

Material	Verdet constant (minutes of arc) gauss^{-1} -cm^{-1}	Reference
Water	.0131 .0130	17 23
Glass (phosphate crown)	.0161	17
Glass (light flint)	.0317	17
Glass (heavy flint)	.0647	23
Carbon disulphide (CS_2)	.0423 .0441	17 23
Quartz ($\perp$ to axis)	.0166	17
Ethyl alcohol (CH_3CH_2OH)	.0107	23
Benzene (C_6H_6)	.0297	23
Atmosphere	6.83×10^{-6}	23
Carbon dioxide (CO_2)	13.0×10^{-6}	23

TABLE III. Spectroscopic constants of CO and HCℓ and the physical constants used in computations.

Spectroscopic constant	$C^{12}O^{16}$	$H^1Cℓ^{35}$
ω_e, cm^{-1}	2169.81	2989.74
B_e, cm^{-1}	1.93130	10.5909
$\omega_e x_e$, cm^{-1}	13.284	52.05
$\omega_e y_e$, cm^{-1}	0.010	0.056
α_e, cm^{-1}	0.017543	0.3019
D_e, cm^{-1}	$5.95x10^{-6}$	$5.32x10^{-4}$
$\alpha_{0,1}$, cm^{-2}-atm^{-1}	70750/T	44540/T
$\alpha_{0,2}$, cm^{-2}-atm^{-1}	496/T	1096/T
ω_F^*, cm^{-1}	2143.27	2885.82
ω_O^*, cm^{-1}	4260.08	5668.04
h, erg sec	$6.6237x10^{-27}$	
c, cm-sec^{-1}	$2.99776x10^{10}$	
k, erg-$(^oK)^{-1}$	$1.38033x10^{-16}$	
σ, erg-cm^{-2}-sec^{-1}-$(^oK)^4$	$0.567x10^{-4}$	

TABLE IV. The quantity $I = \int_0^\infty \left\{1-\exp\left[-K\xi\exp(-\xi)^2\right]\right\}d\xi$ vs K as computed by exact numerical integration.

K	I	K	I
1	.4301	52	2.268
2	.7488	54	2.278
4	1.171	56	2.287
6	1.426	58	2.296
8	1.591	60	2.305
10	1.705	62	2.313
12	1.789	64	2.320
14	1.854	66	2.328
16	1.906	68	2.335
18	1.949	70	2.342
20	1.987	72	2.349
22	2.019	74	2.355
24	2.047	76	2.362
26	2.073	78	2.368
28	2.096	80	2.374
30	2.117	82	2.380
32	2.136	84	2.385
34	2.153	86	2.391
36	2.170	88	2.396
38	2.185	90	2.401
40	2.199	92	2.406
42	2.212	94	2.411
44	2.225	96	2.416
46	2.237	98	2.421
48	2.248	100	2.425
50	2.258	120	2.477

TABLE V. The function A (see equation 46) and the parameter K/X (see equation 47) used in emissivity calculations.

T, °K		300	500	750	1000	1500	2000	3000
CO fundamental	A	2.22^{-3}	2.23^{-2}	4.28^{-2}	4.49^{-2}	3.36^{-2}	2.26^{-2}	1.13^{-2}
	K/X	5.90	2.73	1.49	9.60^{-1}	5.25^{-1}	3.42^{-1}	1.87^{-1}
CO overtone	A	6.97^{-7}	3.84^{-4}	5.70^{-3}	1.60^{-2}	3.05^{-2}	3.21^{-2}	2.37^{-2}
	K/X	4.14^{-2}	1.91^{-2}	1.05^{-2}	6.75^{-3}	3.68^{-3}	2.39^{-3}	1.30^{-3}
HCℓ fundamental	A	3.36^{-4}	1.48^{-2}	5.75^{-2}	8.49^{-2}	8.66^{-2}	6.81^{-2}	3.85^{-2}
	K/X	1.58	7.35^{-1}	4.01^{-1}	2.59^{-1}	1.42^{-1}	9.20^{-2}	5.00^{-2}
HCℓ overtone	A	4.31^{-9}	3.90^{-5}	2.09^{-3}	1.17^{-2}	4.31^{-2}	6.27^{-2}	6.24^{-2}
	K/X	3.89^{-2}	1.81^{-2}	9.90^{-3}	6.40^{-3}	3.50^{-3}	2.27^{-3}	1.23^{-3}

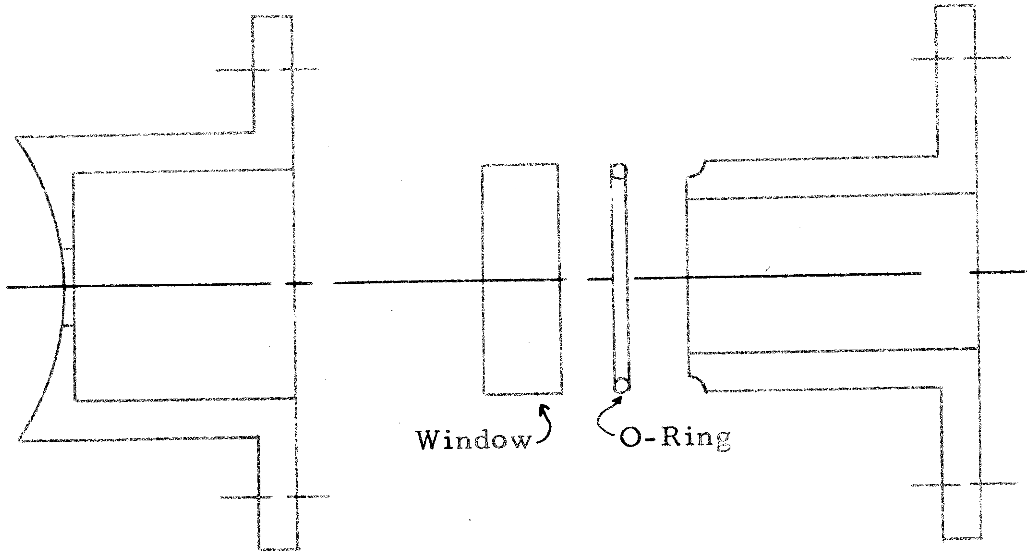

Fig. 1. Cross-section of a removable mount for windows and heat gauges in the shock tube.

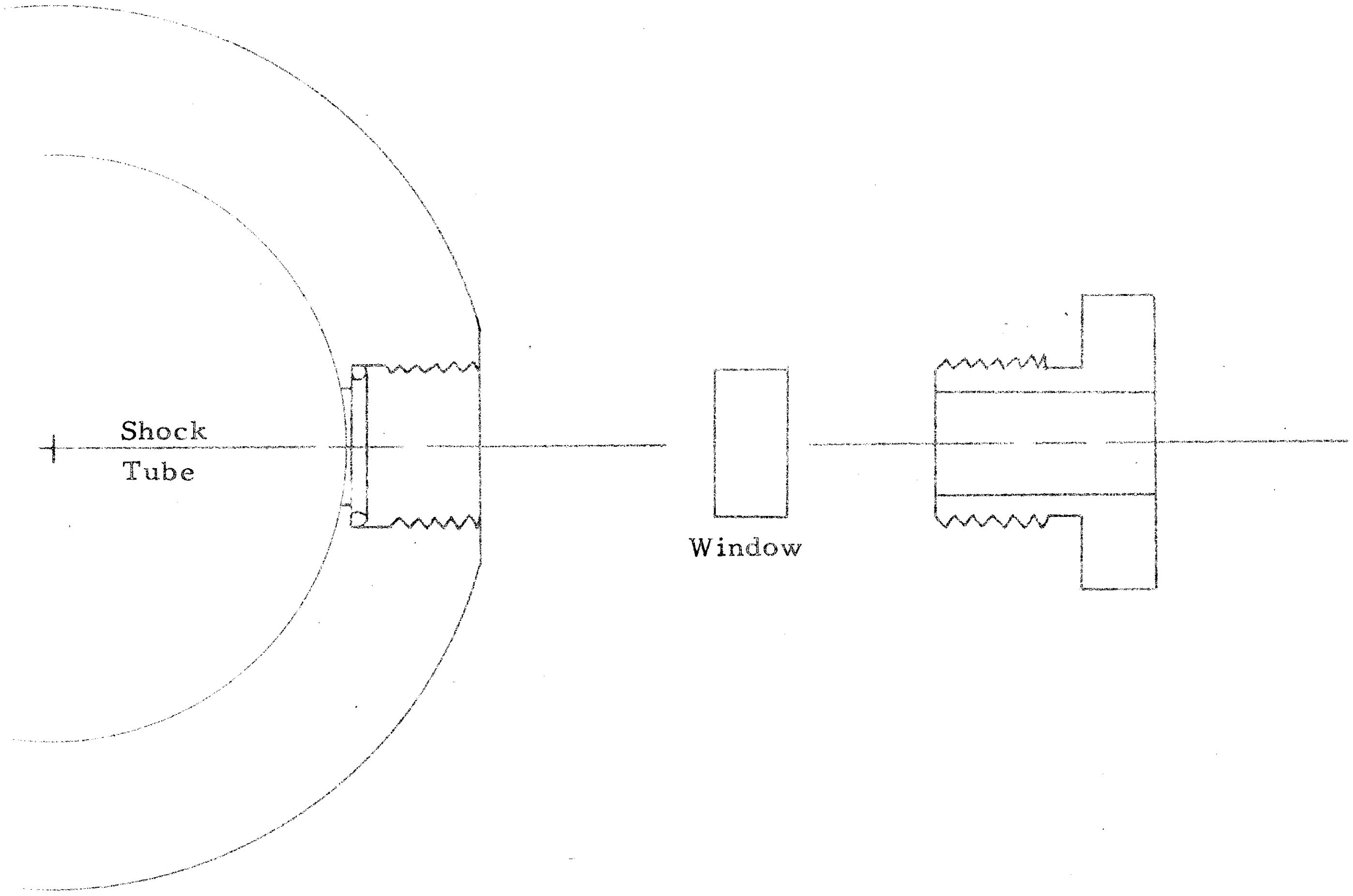

Fig. 2. Cross-section of a window adapter in the observation section of the shock tube.

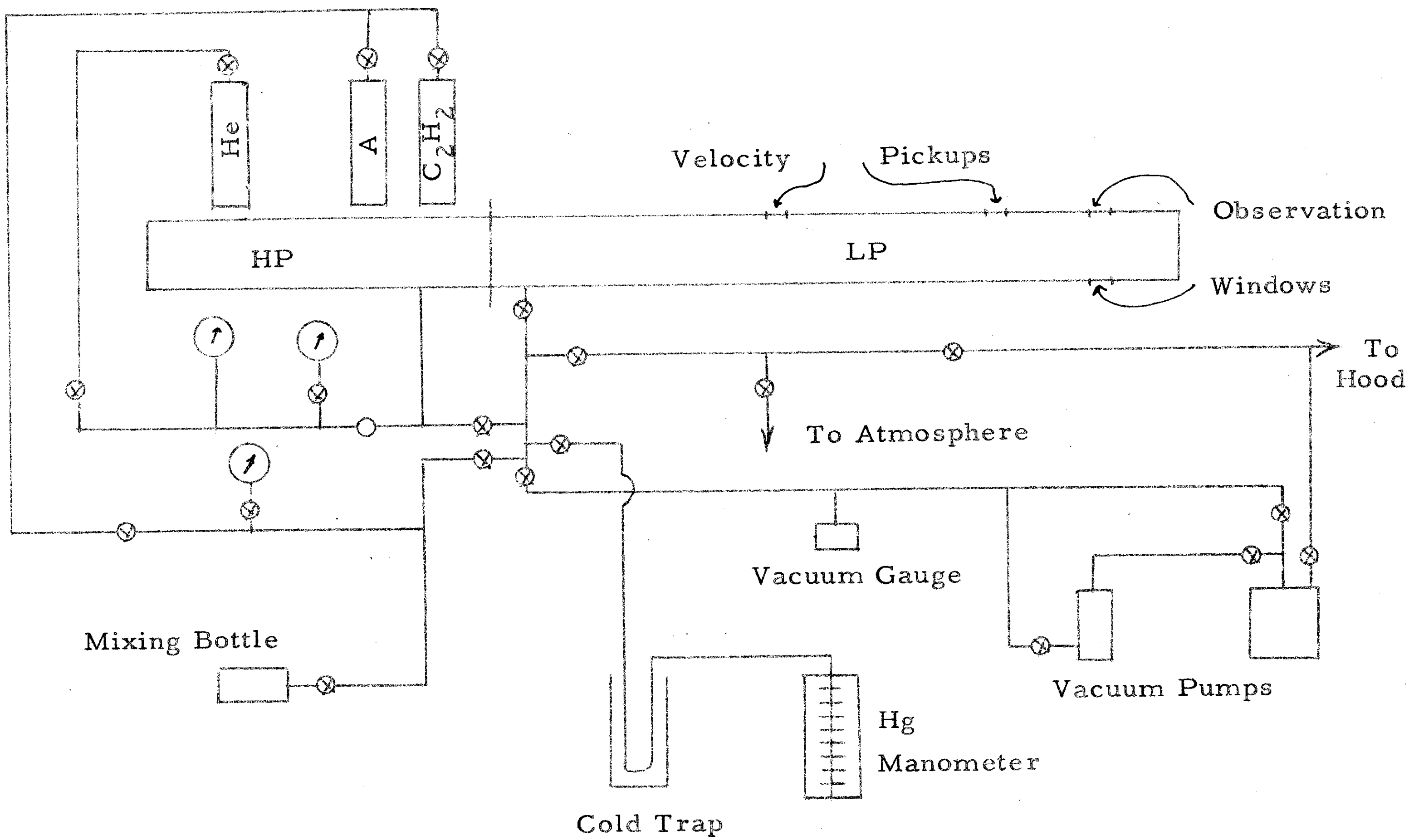

Fig. 3. Block diagram of the shock tube and the associated manifold system.

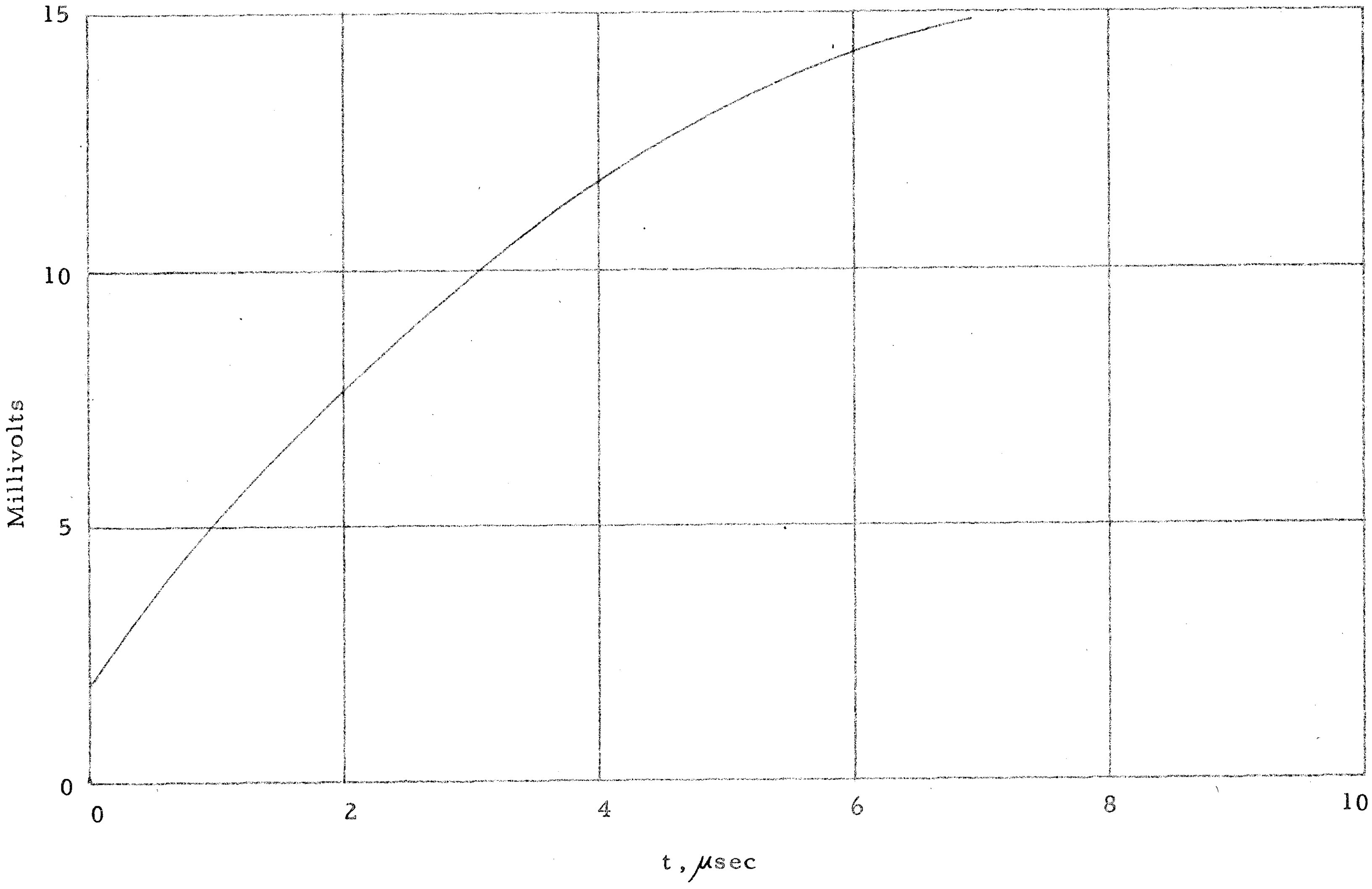

Fig. 4. Tracing of an oscillogram of the voltage output of a heat gauge behind an incident shock wave.

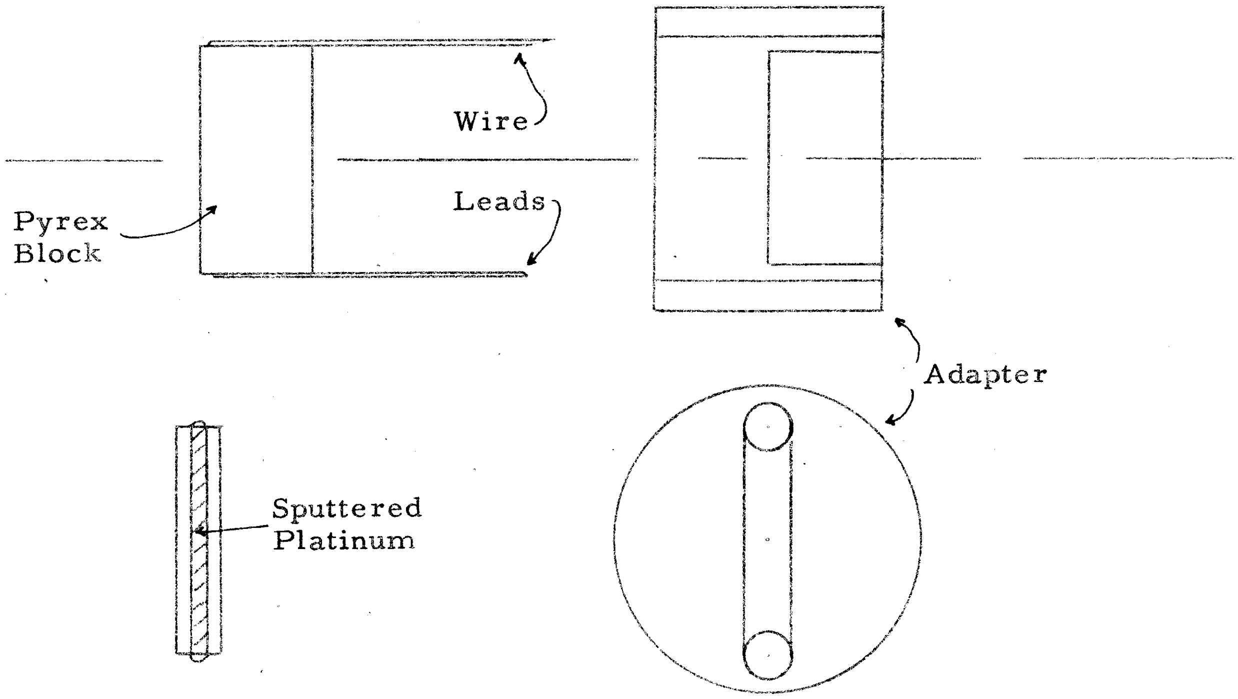

Fig. 5. Schematic of a heat gauge and its adapter. The adapter is placed in the mount shown in figure 1.

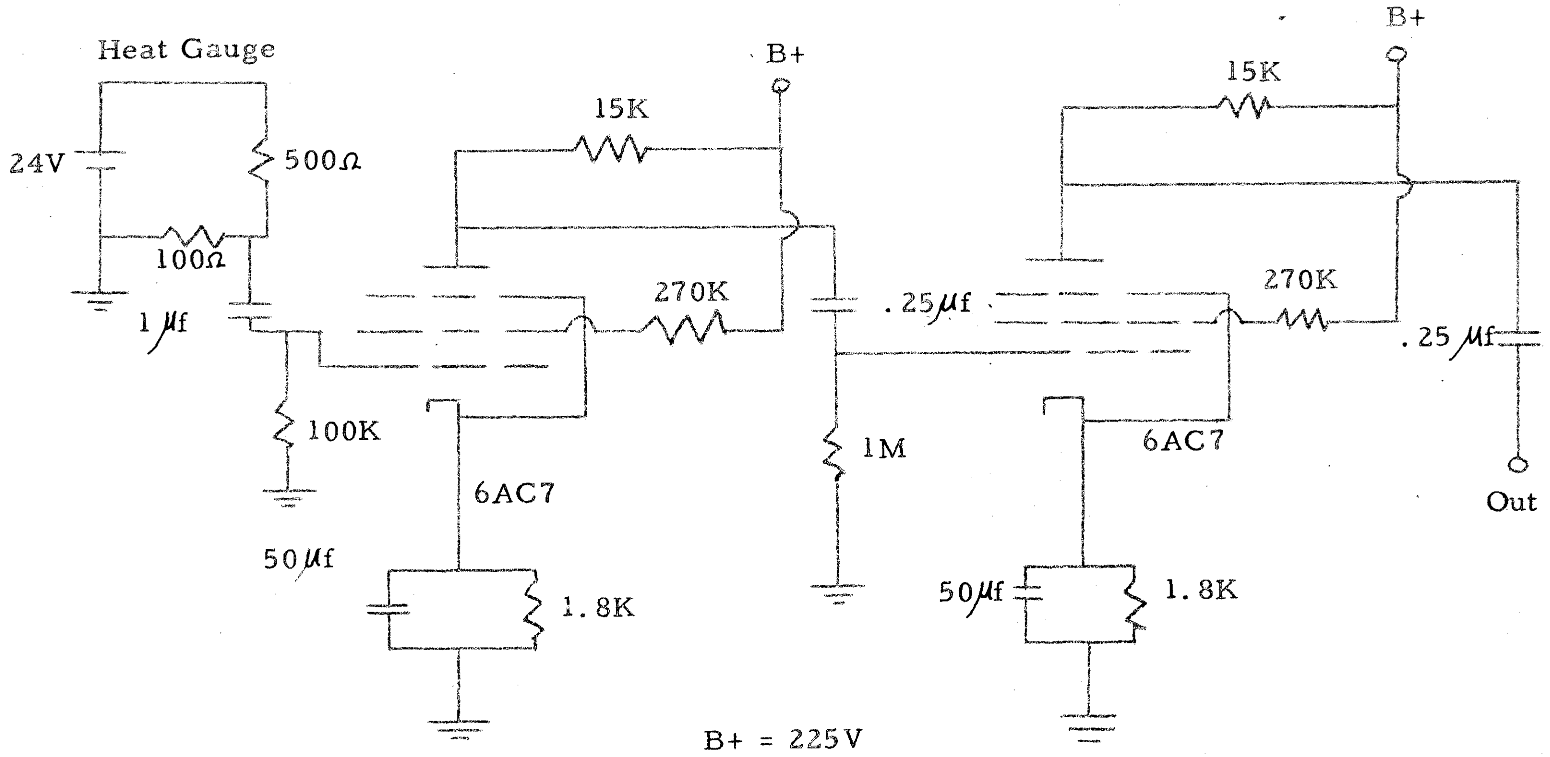

Fig. 6. Bias circuit and amplifier stages for a heat gauge used in shock velocity measurements.

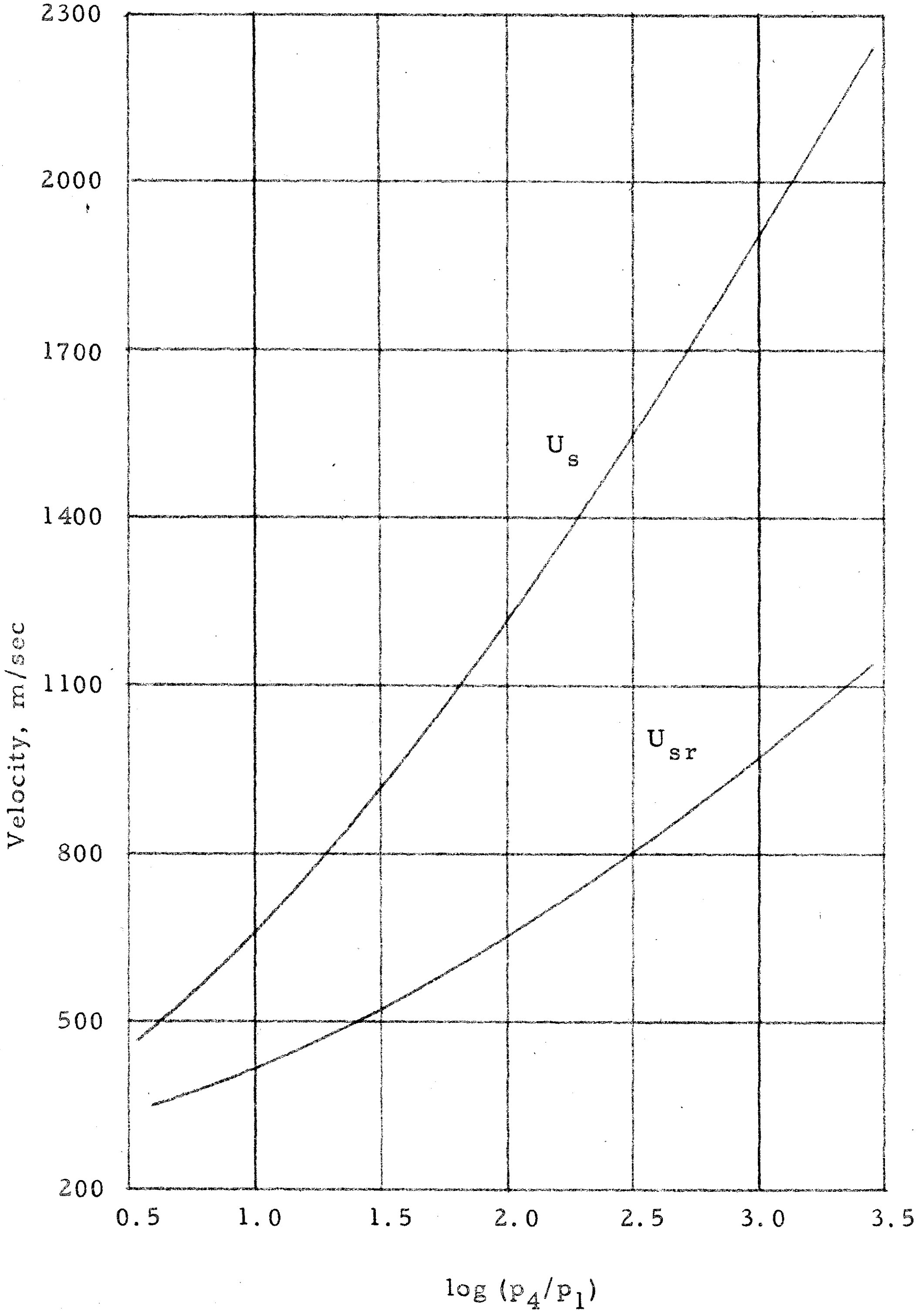

Fig. 7. Incident and reflected shock velocities vs. log (p_4/p_1) for a mixture of 95 per cent of A - 5 per cent of C_2H_2; $\gamma = 5/3$ [from Bennett (2)]. The driver gas is helium.

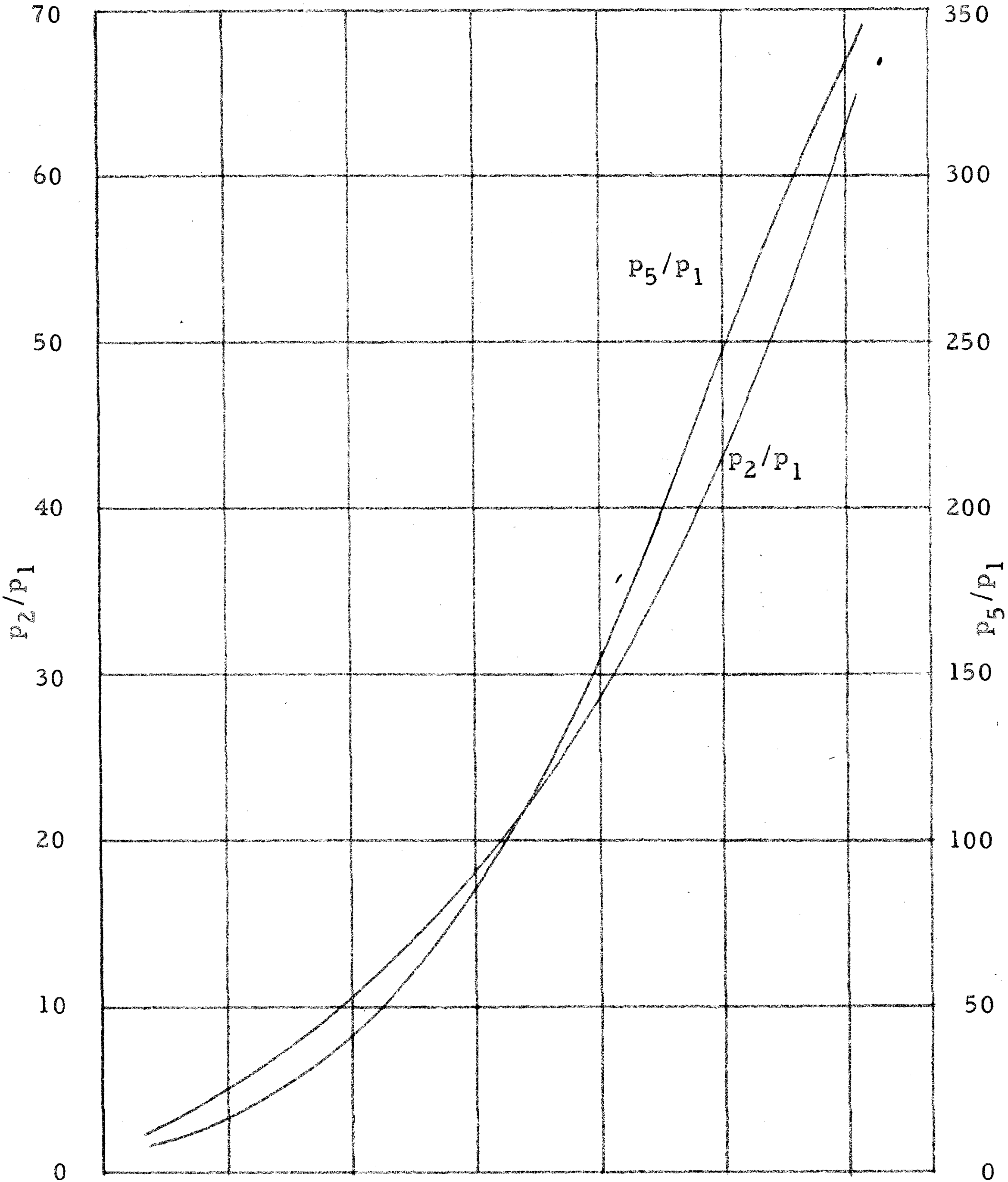

Fig. 8. Pressure ratios p_2/p_1 and p_5/p_1 vs log (p_4/p_1) for for a mixture of 95 per cent of A - 5 per cent of C_2H_2; $\gamma = 5/3$ [from Bennett (2)].

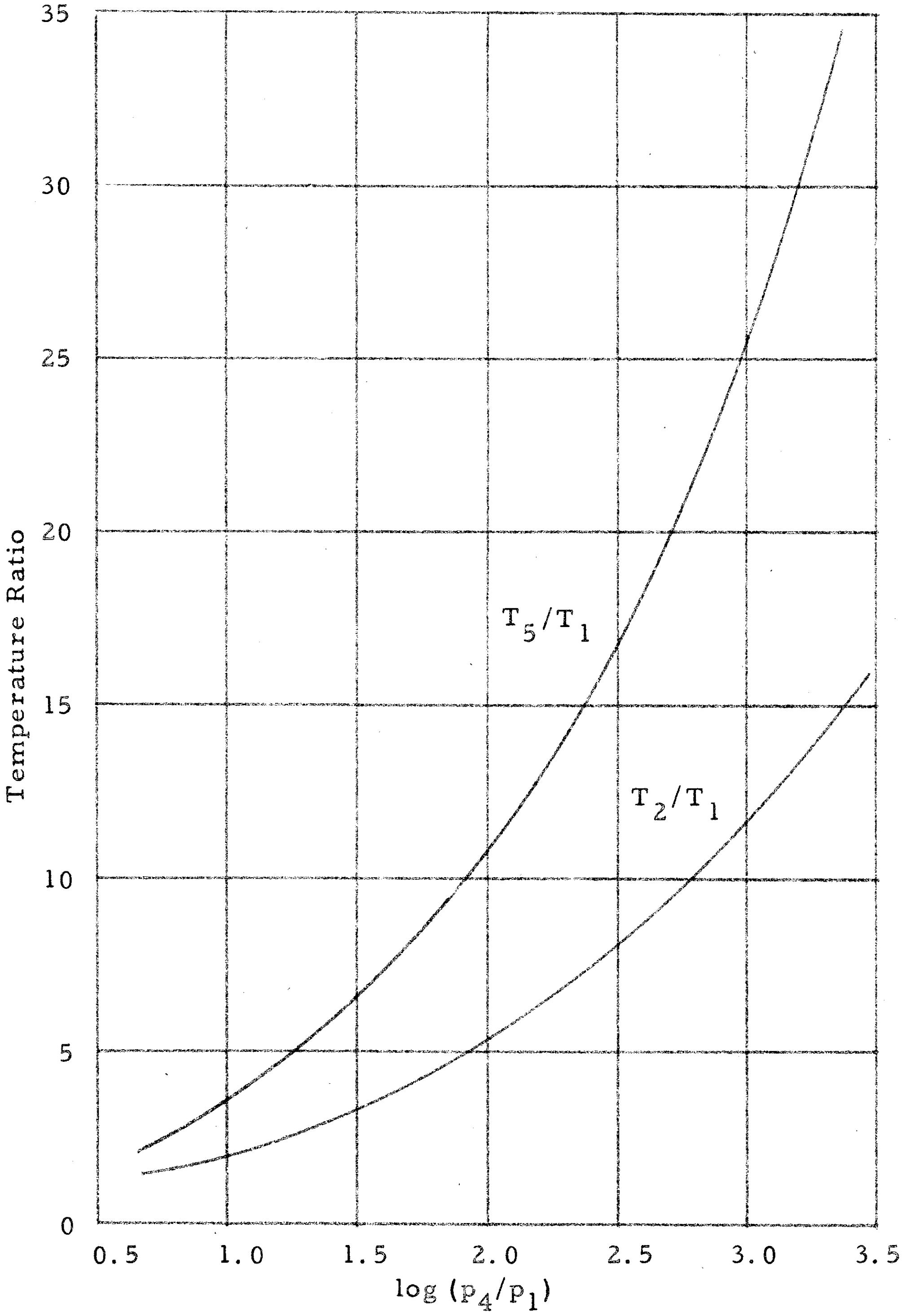

Fig. 9. Temperature ratios T_2/T_1 and T_5/T_1 vs log (p_4/p_1) for a mixture of 95 per cent of A - 5 per cent of C_2H_2; $\gamma = 5/3$ [from Bennett (2)].

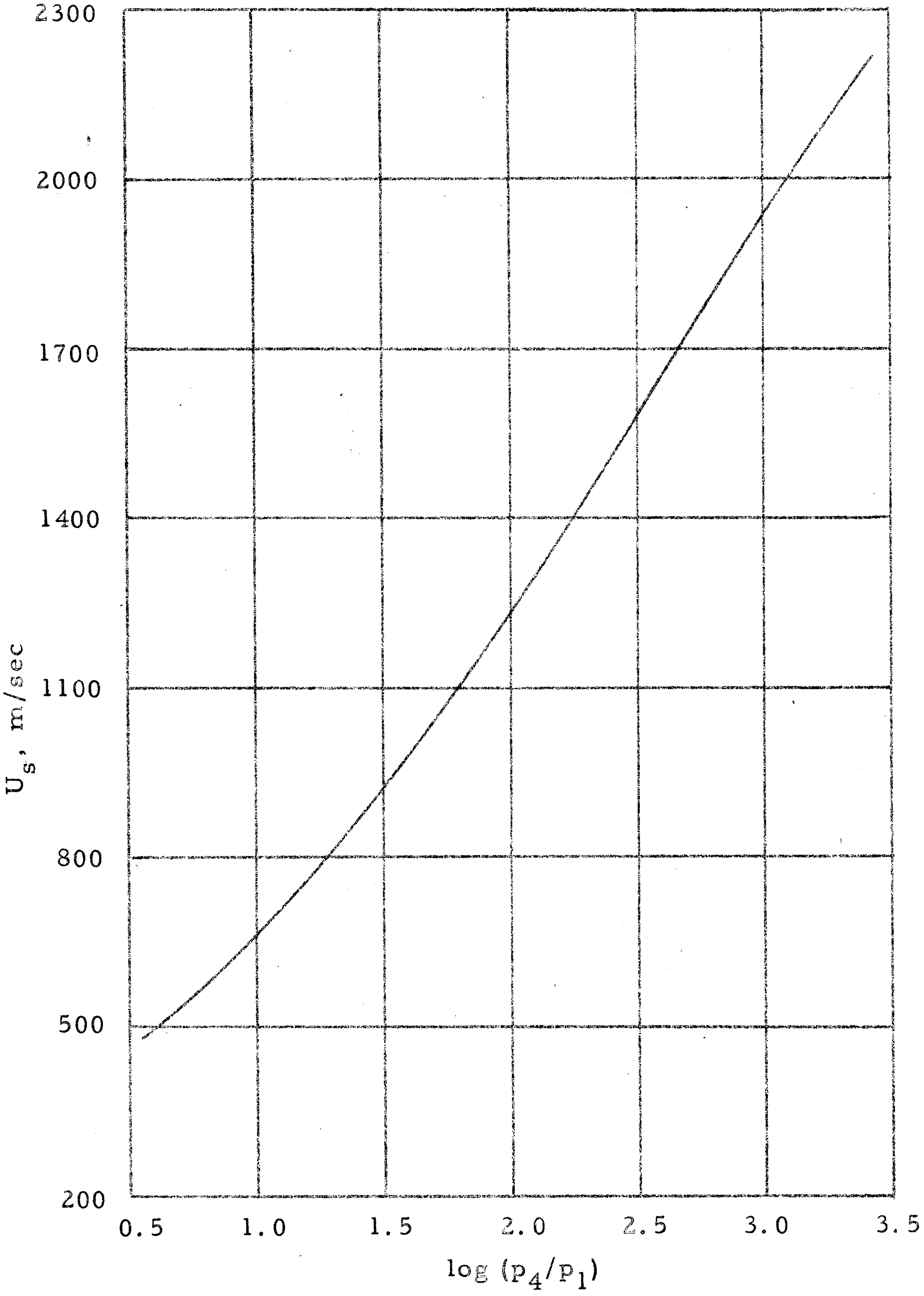

Fig. 10. Incident shock velocity vs log (p_4/p_1) for argon; $\gamma = 5/3$ [from Lukasiewicz (4)]. The driver gas is helium.

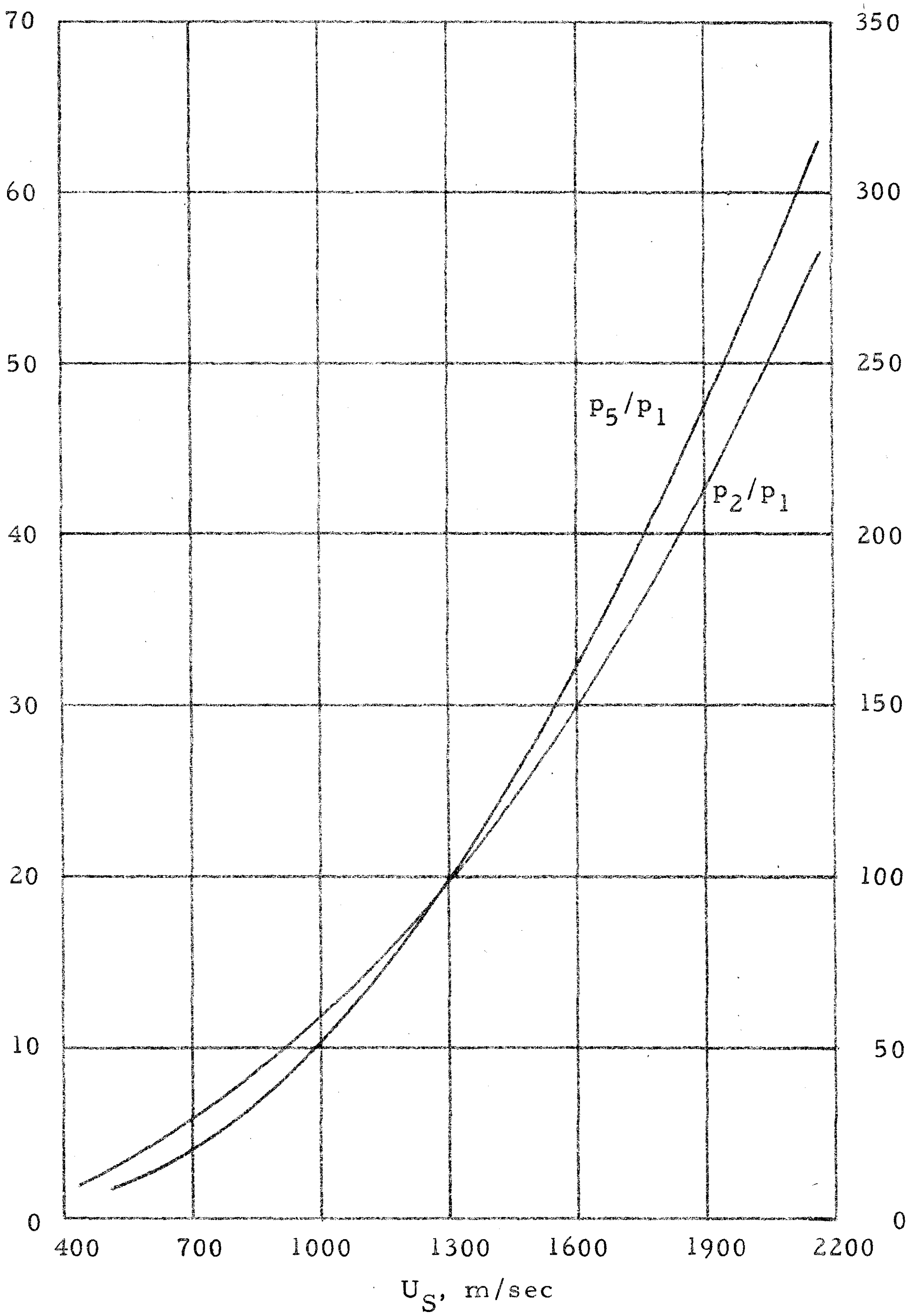

Fig. 11. Pressure ratios p_2/p_1 and p_5/p_1 vs incident shock velocity, U_s, for argon; $\gamma = 5/3$ [from Lukasiewicz (4)].

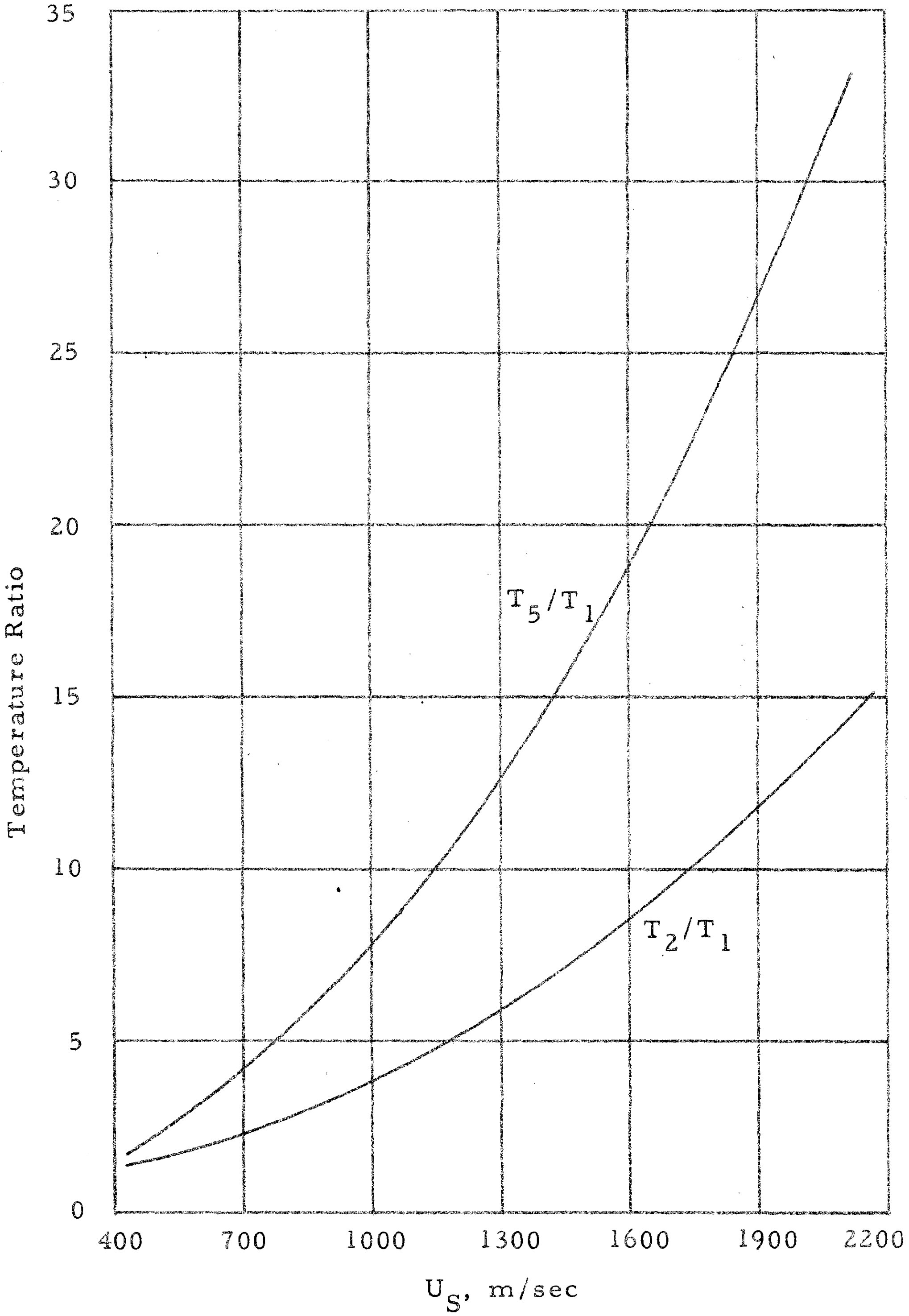

Fig. 12. Temperature ratios T_2/T_1 and T_5/T_1 vs incident shock velocity, U_s, for argon; $\gamma = 5/3$ [from Lukasiewicz (4)].

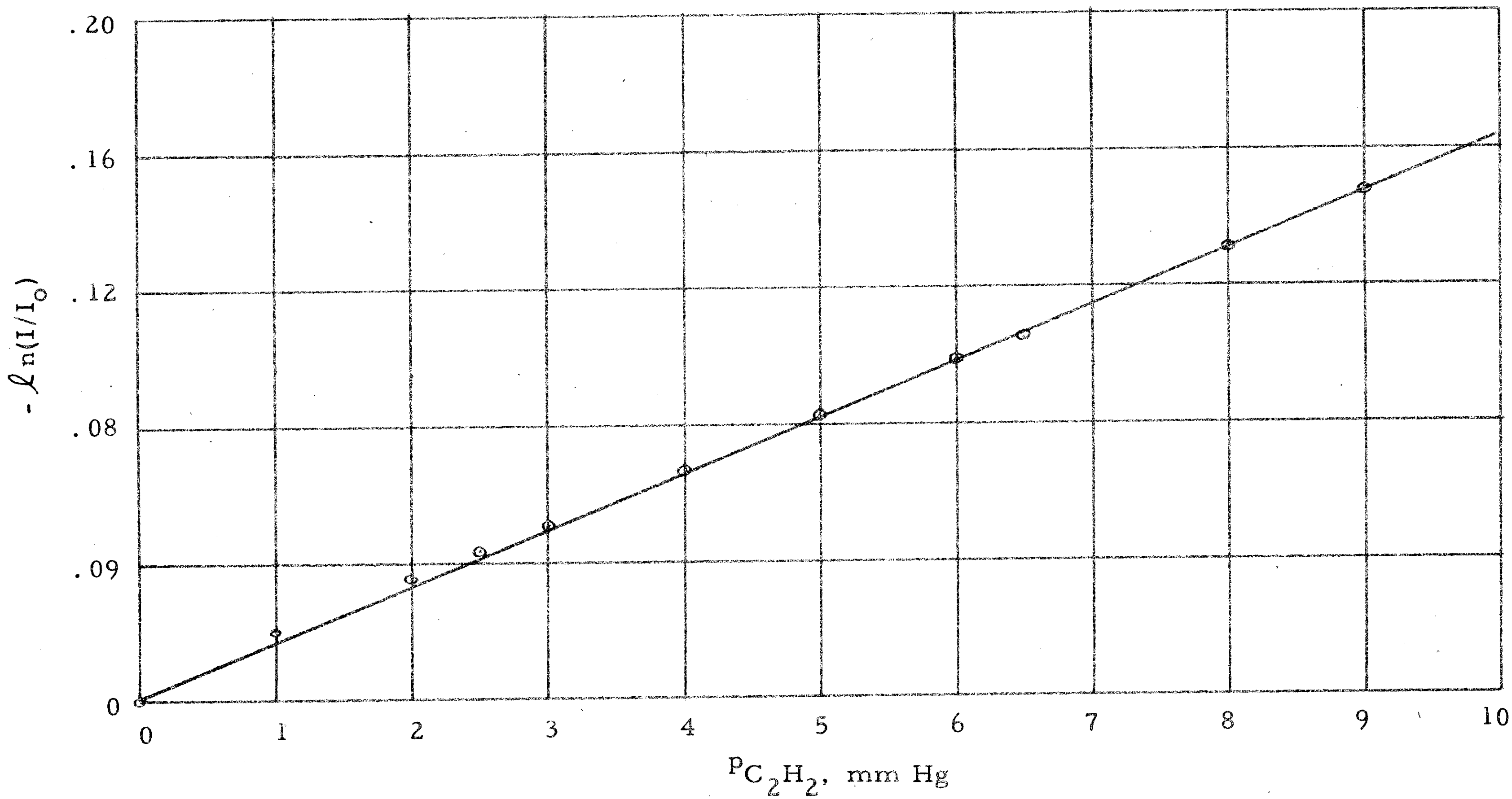

Fig. 13. Logarithm of the fractional transmission vs. acetylene partial pressure as determined by the quantitative infrared analysis described in section II C.

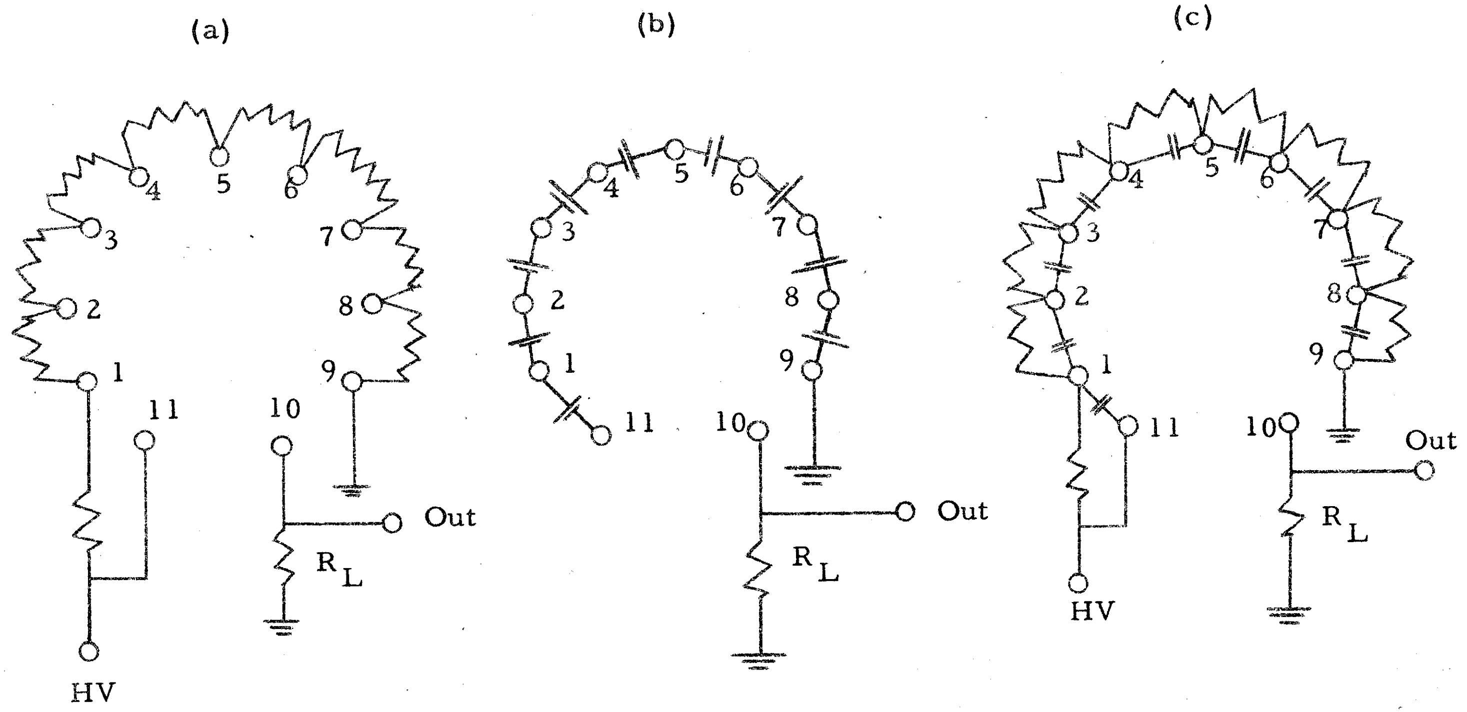

Fig. 14. Circuits for the stage-to-stage voltage dividers of photomultiplier tubes. R_L = 2K; all other resistors = 100 K; all capacitors = 0.1 μf; all batteries = 112 V; HV = 900 VDC.

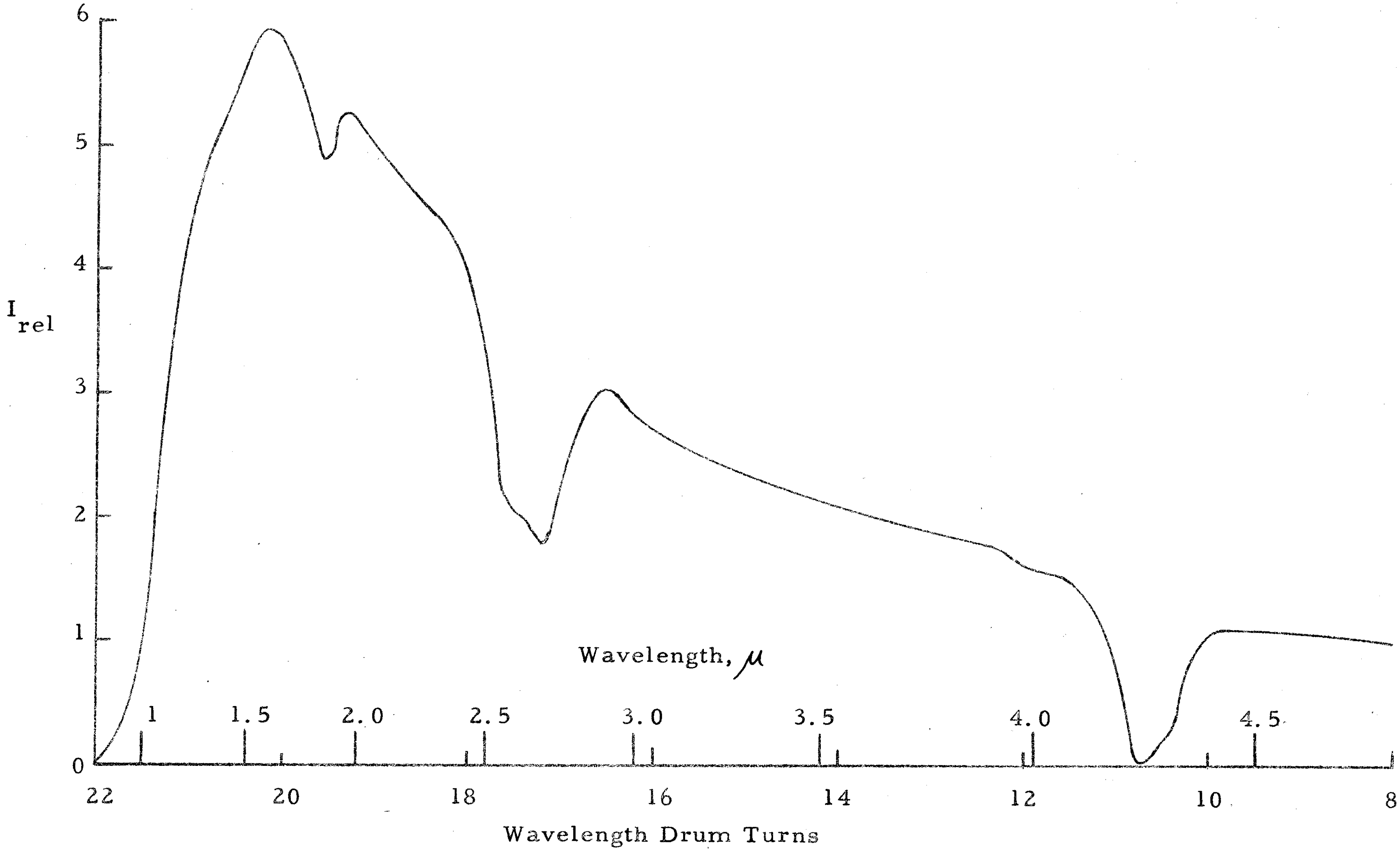

Fig. 15. Relative spectral response of an InSb infrared detector cooled to the temperature of liquid introgen. Atmospheric water vapor and CO_2 absorption bands are superposed on the $2000^{o}K$ blackbody distribution.

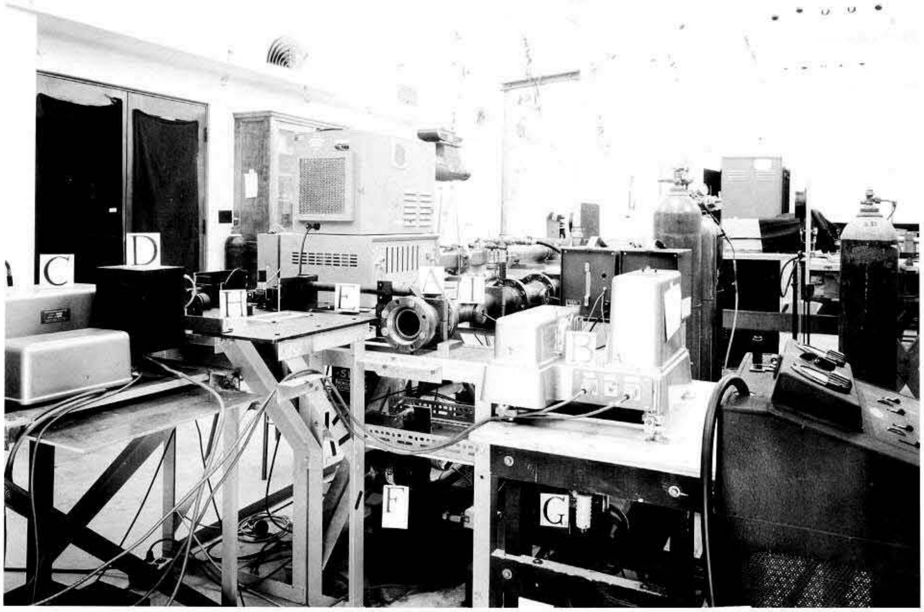

Fig. 16. Photograph of the assembled shock-tube facility with the major parts labeled.

A. Low-pressure end of the shock tube.
B. Perkin-Elmer infrared source optics and 13 cycles chopper.
C. Perkin-Elmer infrared monochromator.
D. Compartment for indium-antimonide infrared detector.
E. Single- and double-path collimating systems.
F. The 180 kc mechanical light chopper.
G. Carbon arc source.
H. Condensing optics for monochromator slit.
I. Shock velocity measuring station.

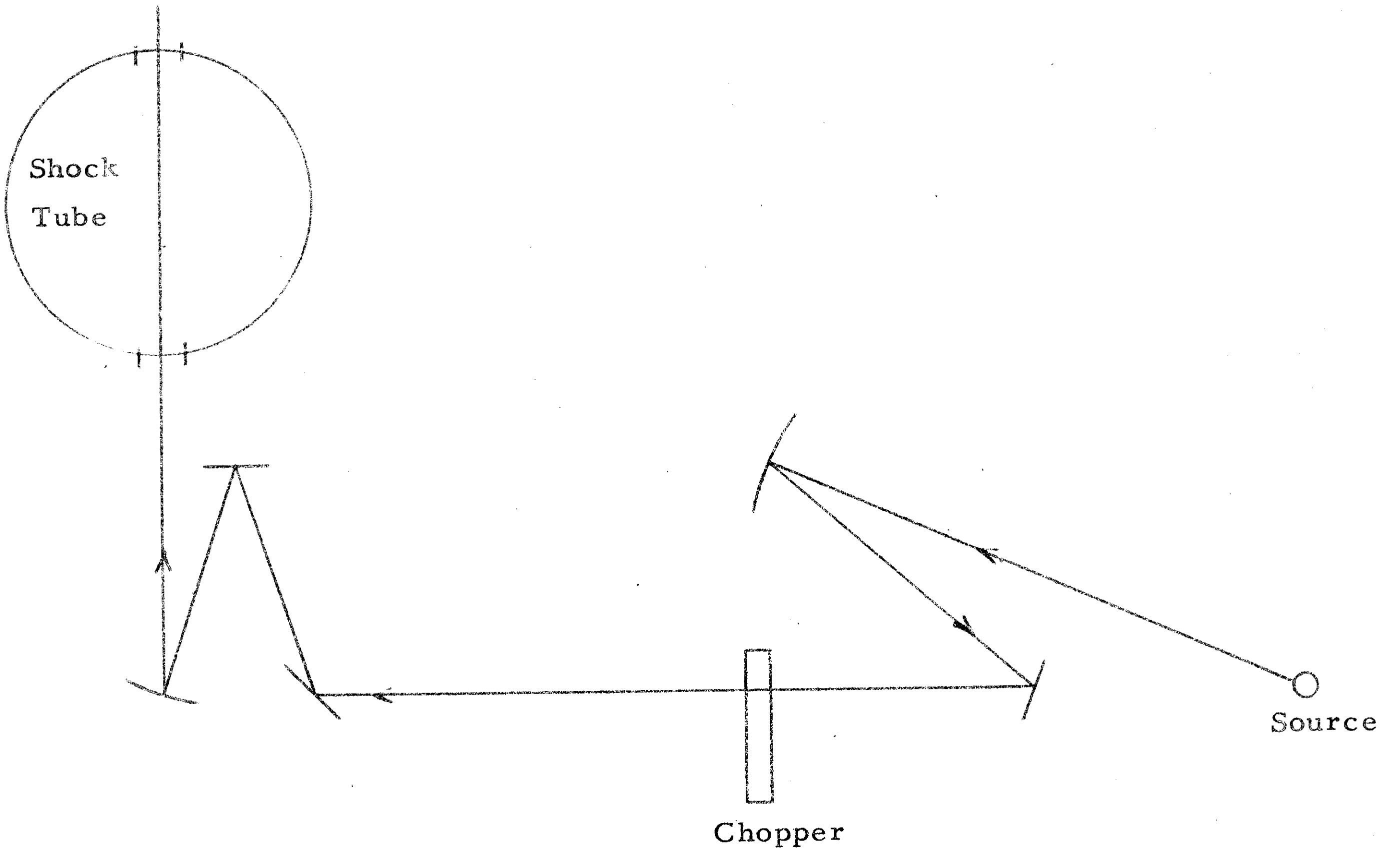

Fig. 17. Schematic of the light source and mechanical chopper optics for a simultaneous emission and absorption experiment.

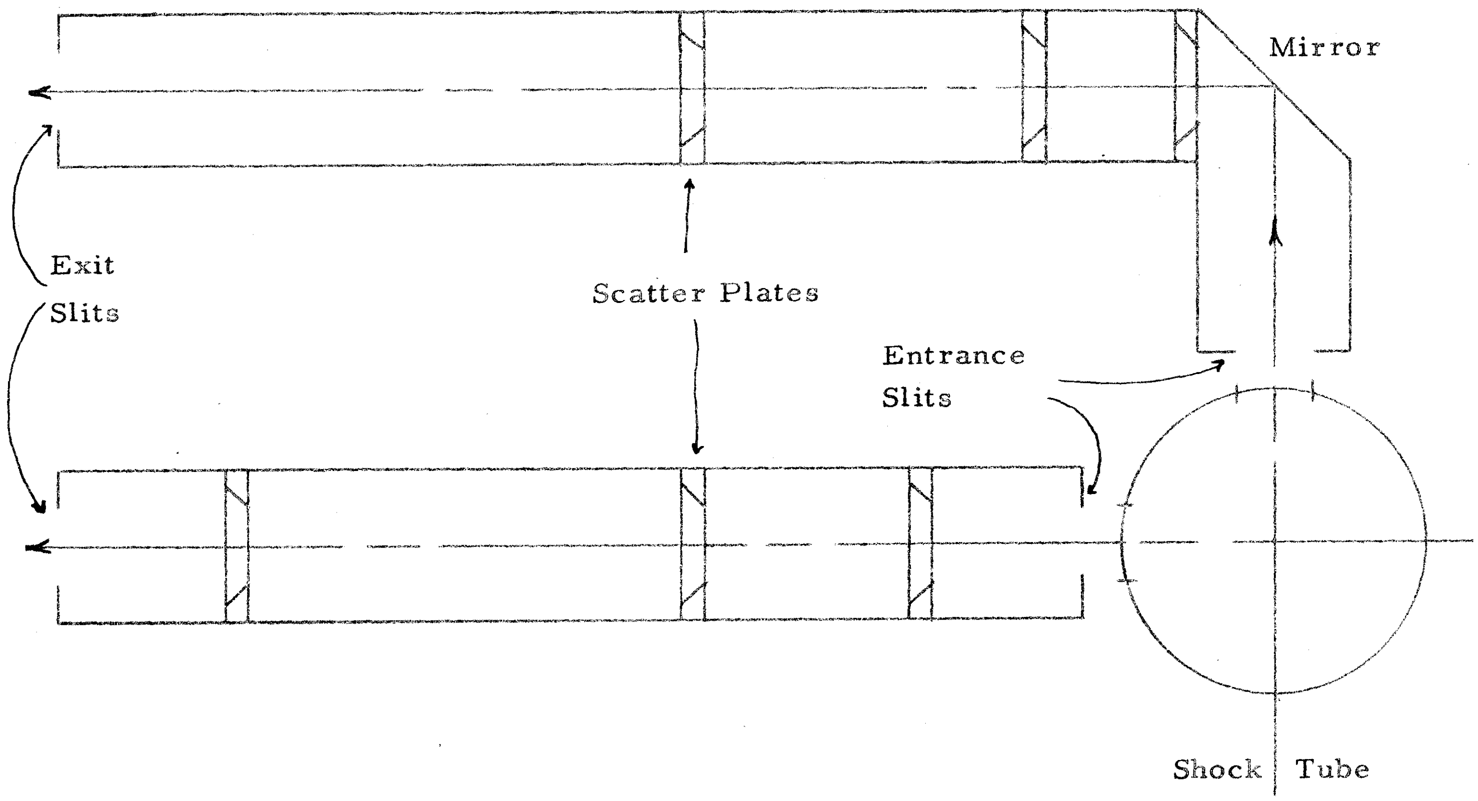

Fig. 18. Cross-section of the collimating systems for the two coplanar regions of observation in the shock tube.

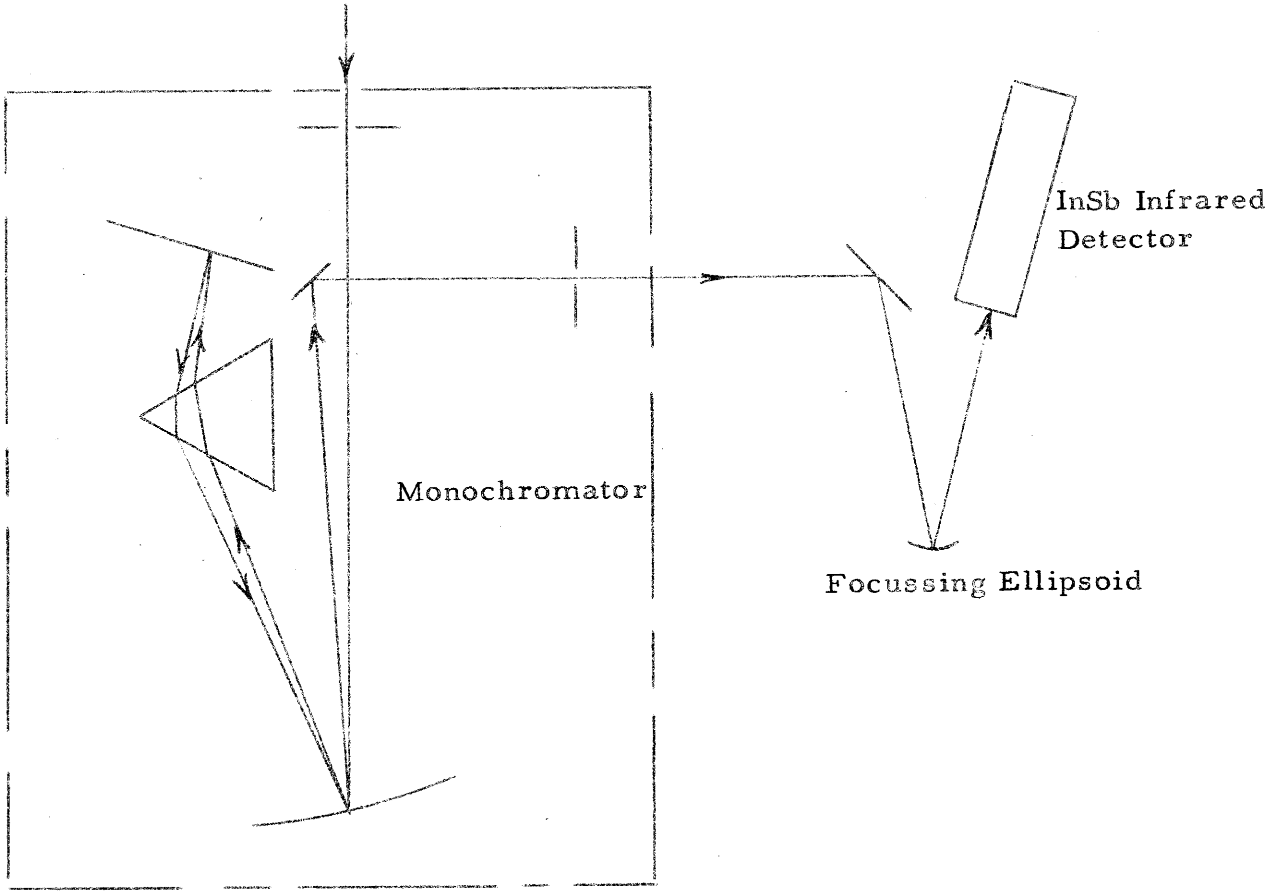

Figure 19. Schematic of the InSb focussing optics adjacent to the Perkin-Elmer monochromator.

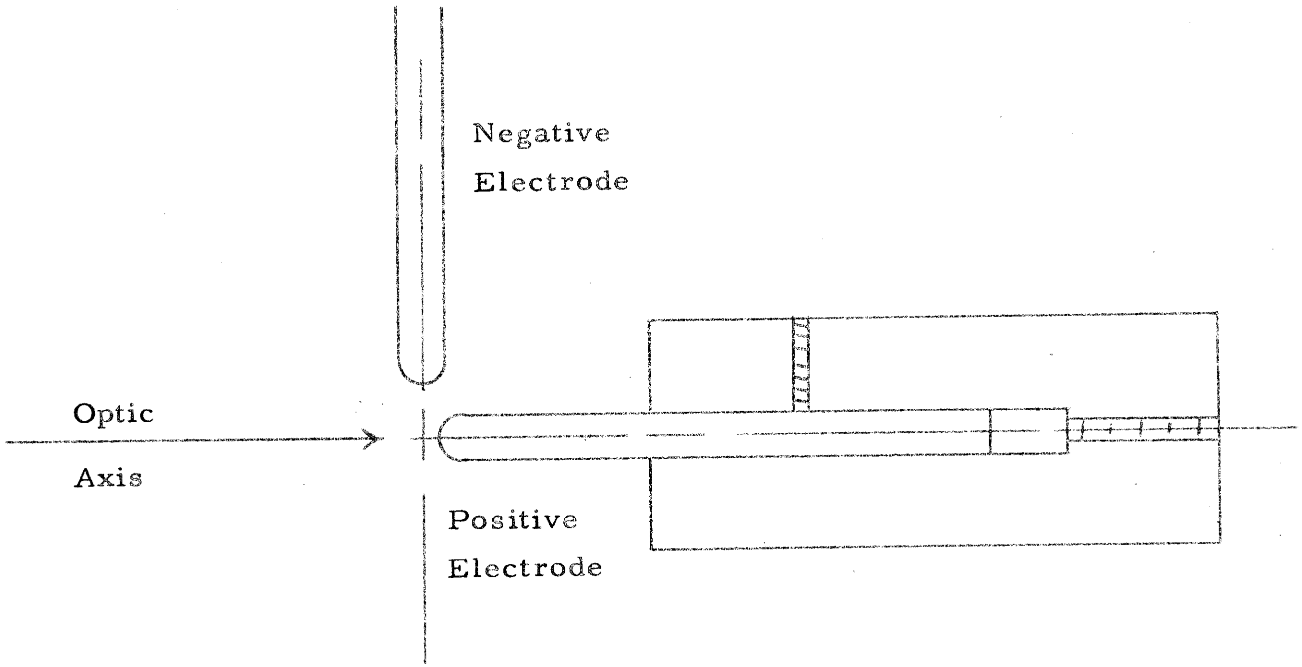

Fig. 20. Schematic of the carbon arc electrode assembly.

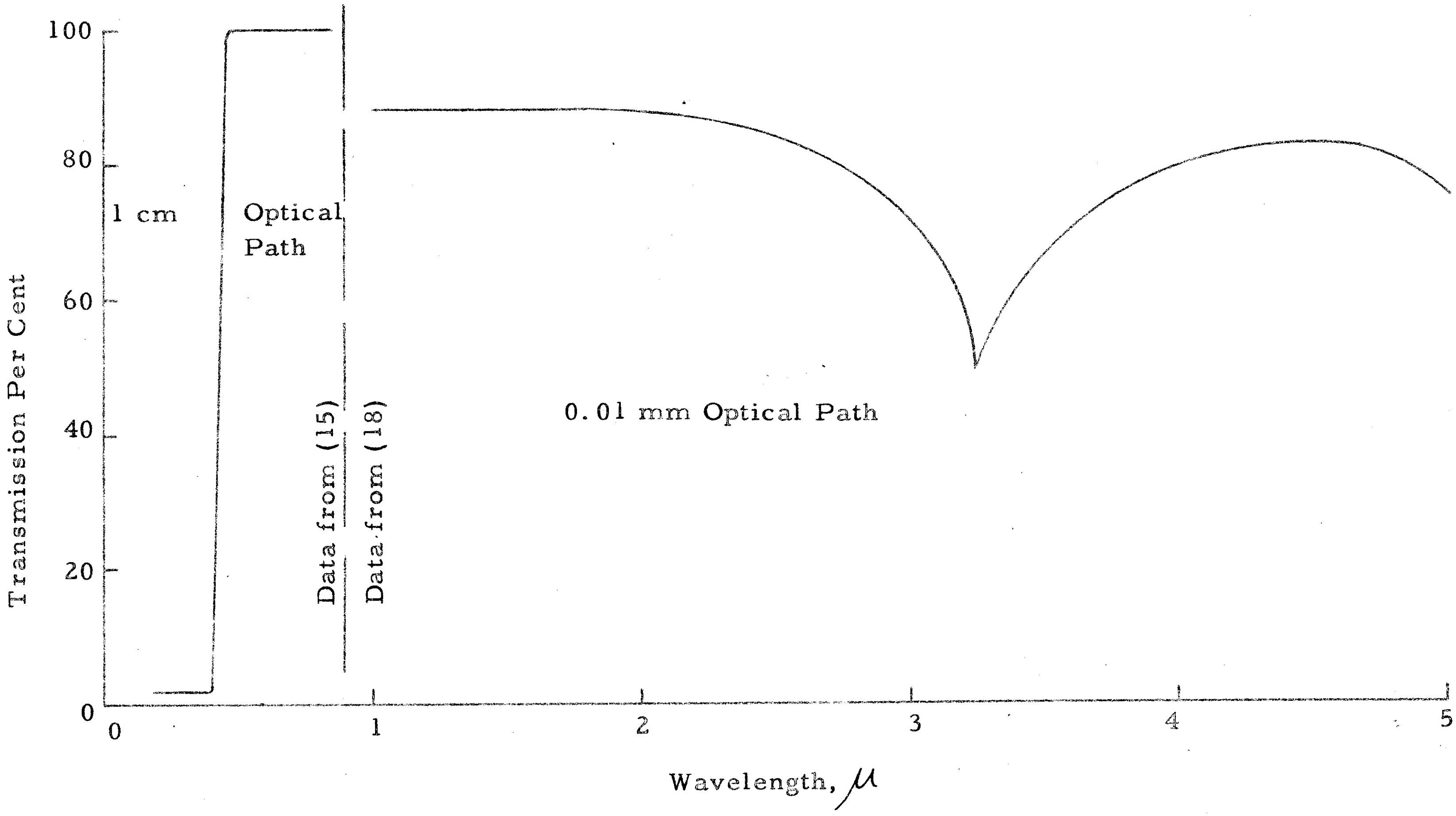

Fig. 21. Nitrobenzene absorption spectrum [from Zarem et al (15) and Coblentz (18)].

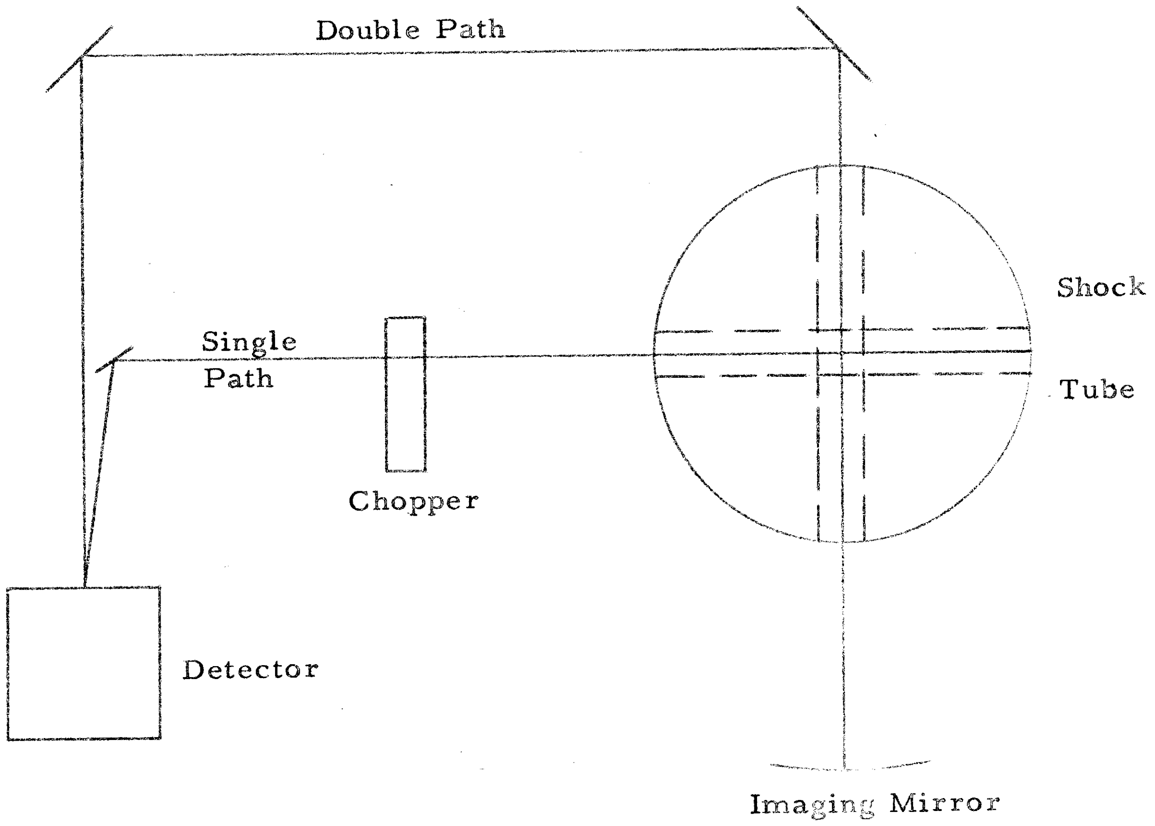

Fig. 22. Schematic of the optical system for a single-double-path experiment.

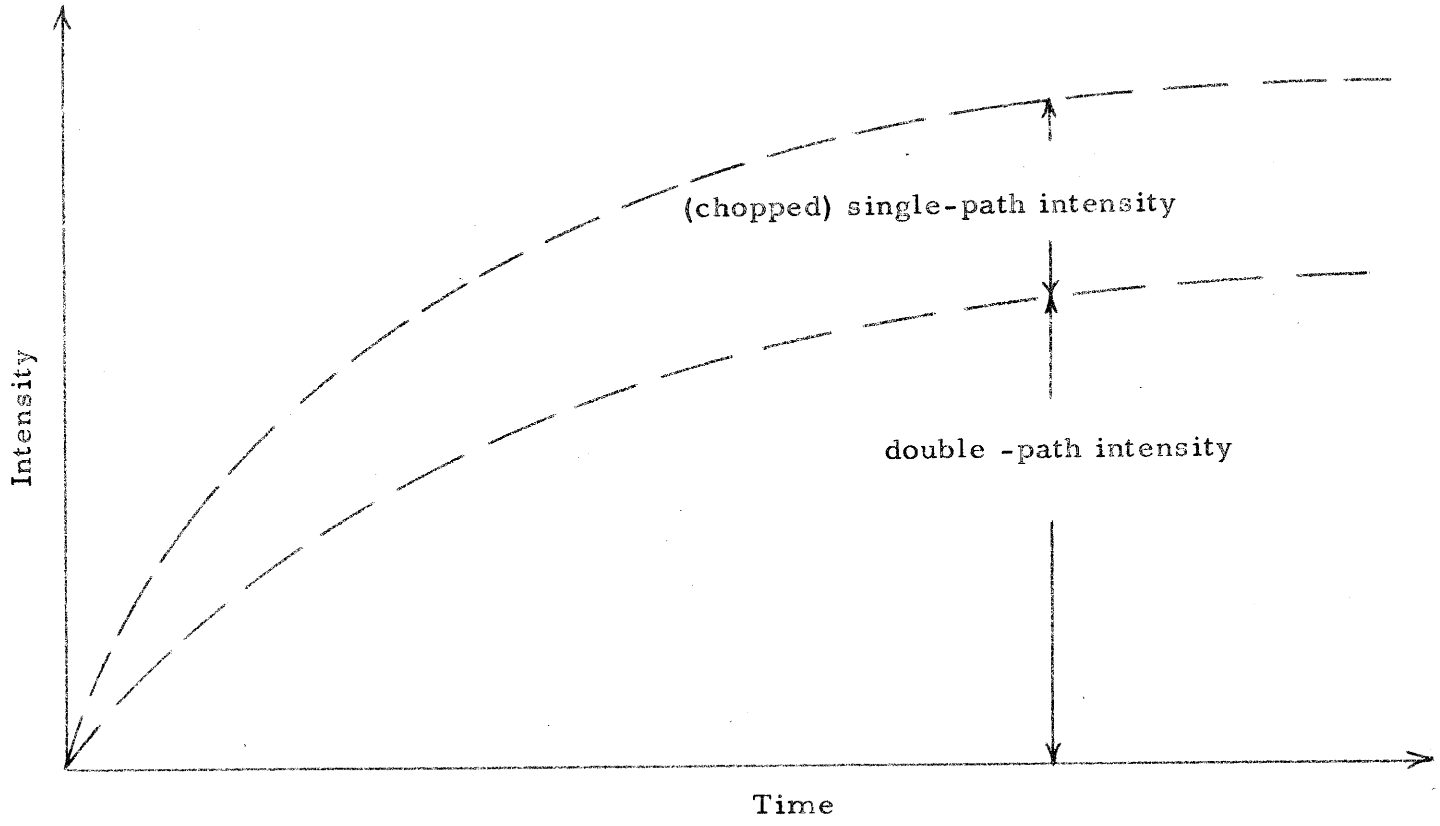

Fig. 23. Schematic of the detector output for a single-double path experiment.

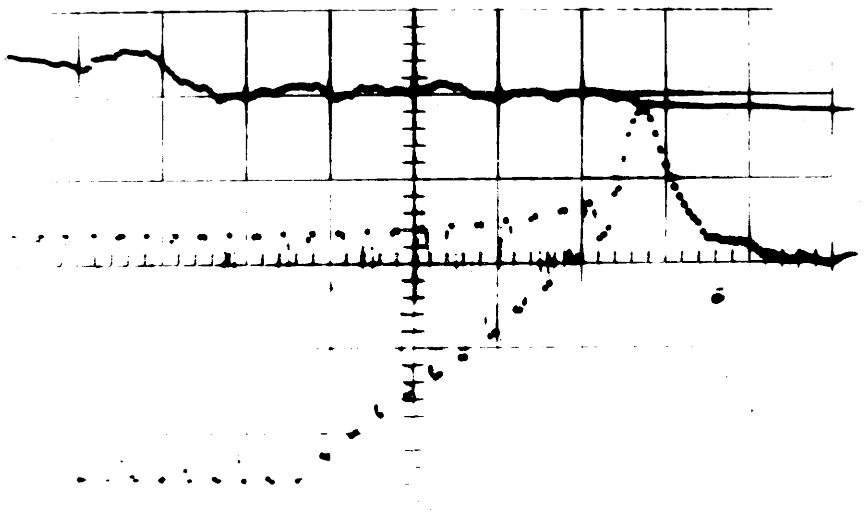

Fig. 24. Copy of an oscilloscope record from a simultaneous emission and absorption experiment. The time increases to the right at 20 μsec per major division. The top trace corresponds to acetylene emission at 3287 cm^{-1}; the intensity increases downwards. The bottom trace shows chopped, transmitted radiation in the visible region of the spectrum with intensity increasing upwards.

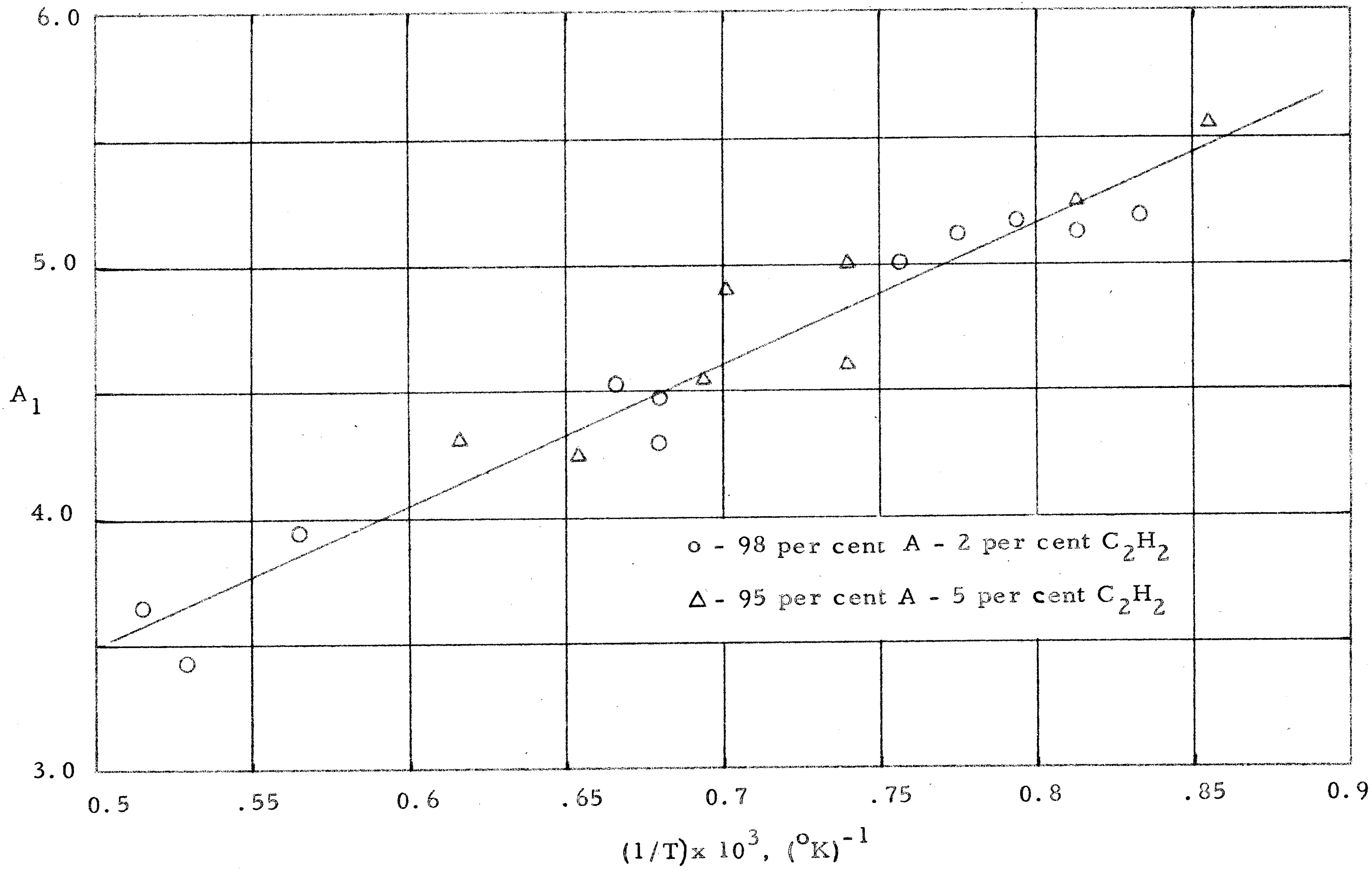

Fig. 25. The quantity $A_1 = -\log_{10}\left\{\left[-1/p_{C_2H_2}\right] d\left[\ell n(I_t/I_o)\right]/dt\right\}$ vs (1/T). The term $d\left[\ell n(I_t/I_o)\right]/dt$ has been evaluated for the initial increase in absorption.

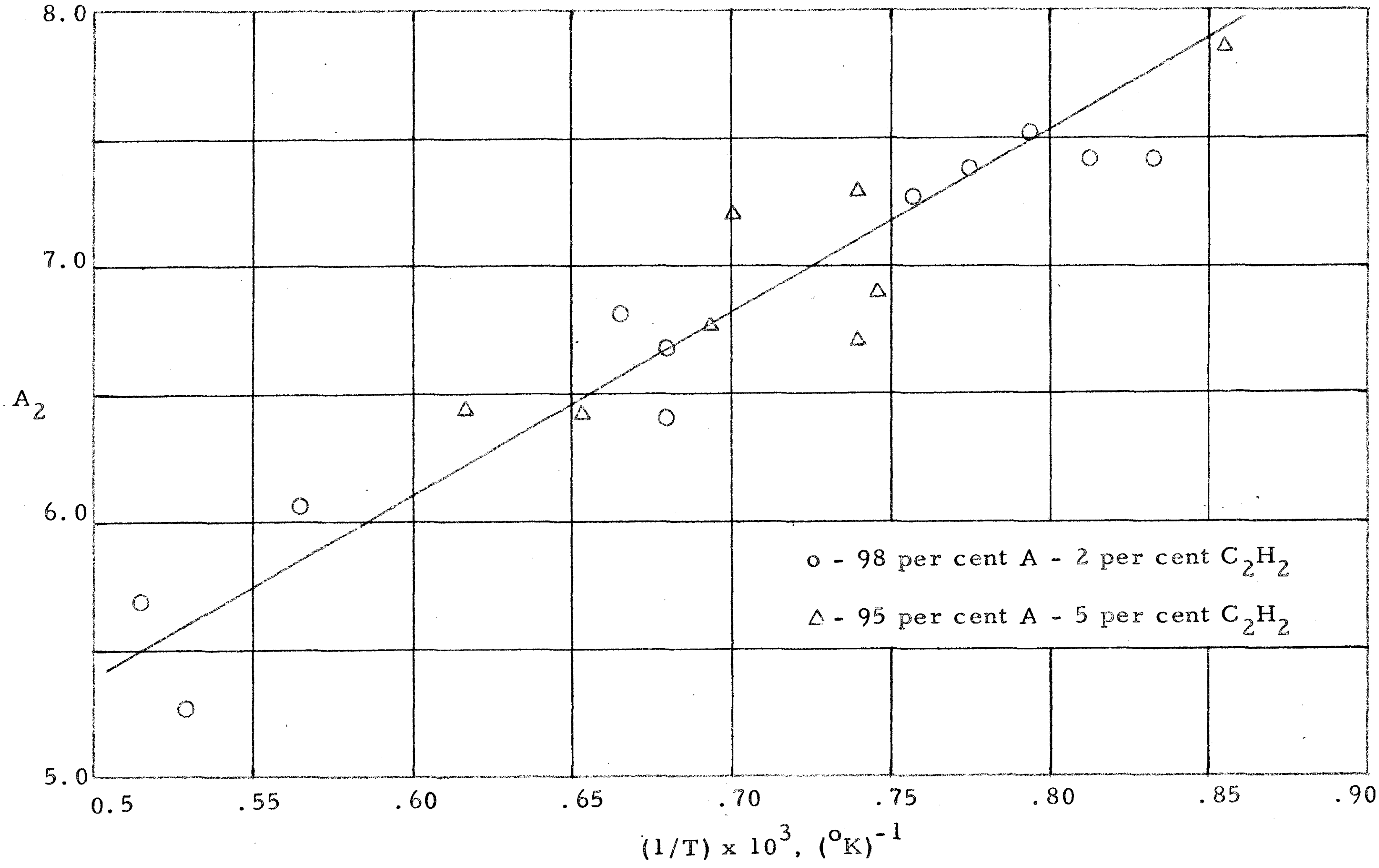

Fig. 26. The quantity $A_2 = -\log \left\{ \left[-1/(p_{C_2H_2})^2 \right] \left[d[\ell n(I_t/I_o)]/dt \right] \right\}$ vs (1/T). The term $d[\ell n(I_t/I_o)]/dt$ has been evaluated for the initial increase in absorption.

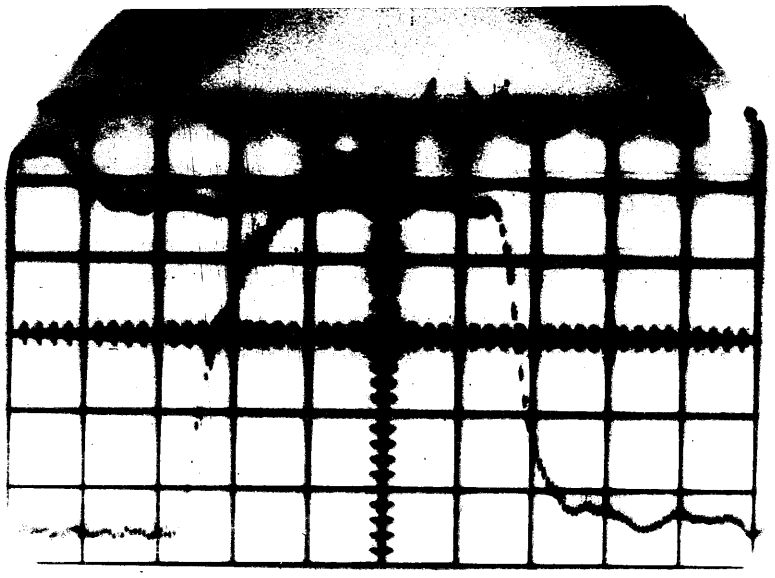

Fig. 27. Copy of an oscilloscope record from an induction time experiment. The time increases to the right at 20 μsec per major division. The top trace corresponds to acetylene emission at 3287 cm^{-1}; the intensity increases downwards. The bottom trace shows carbon radiation in the visible region of the spectrum with intensity increasing upwards.

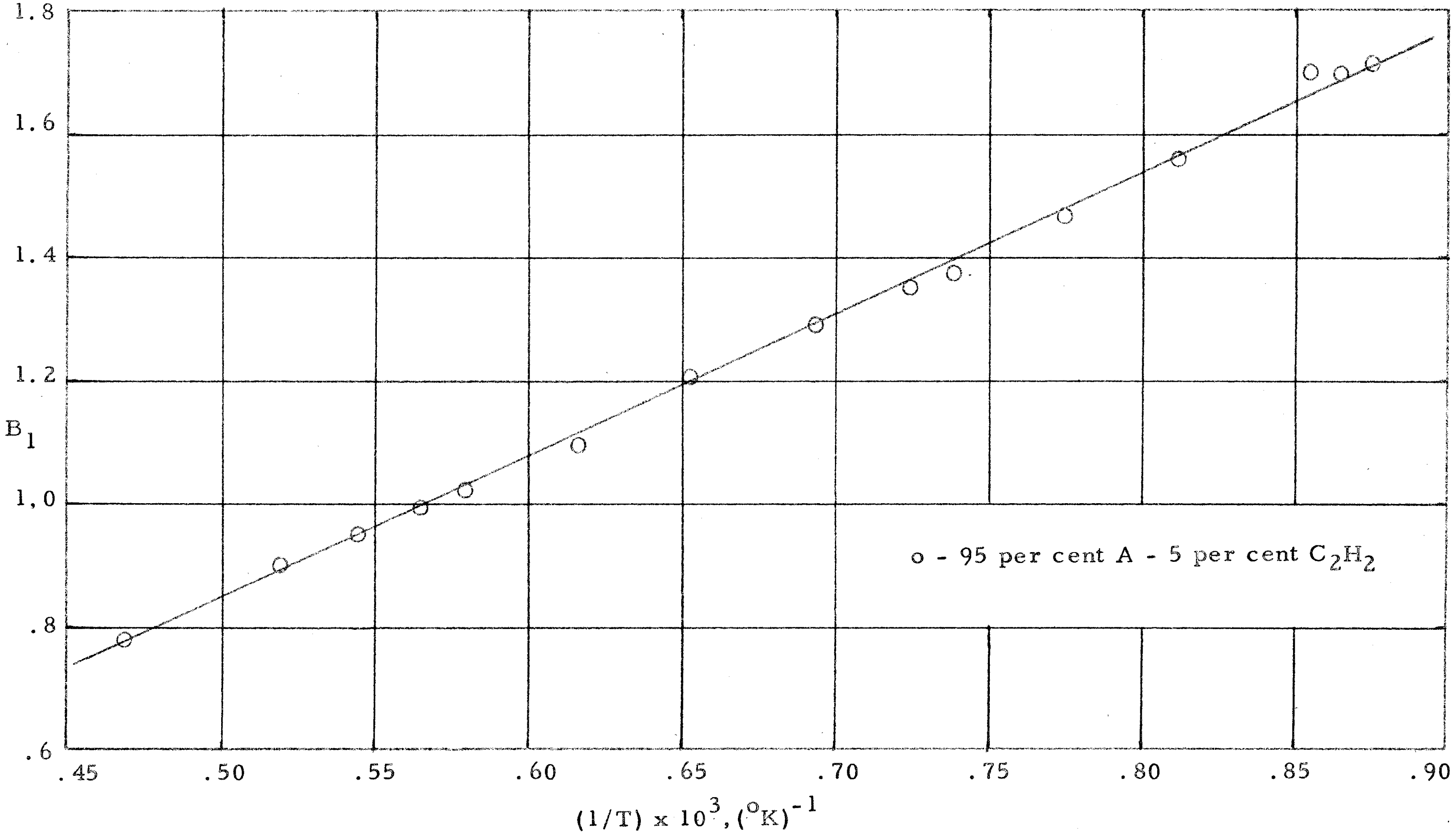

Fig. 28. The quantity $B_1 = \log_{10}\left[(p_{C_2H_2})\,\Delta\tau\right]$ vs (1/T) .

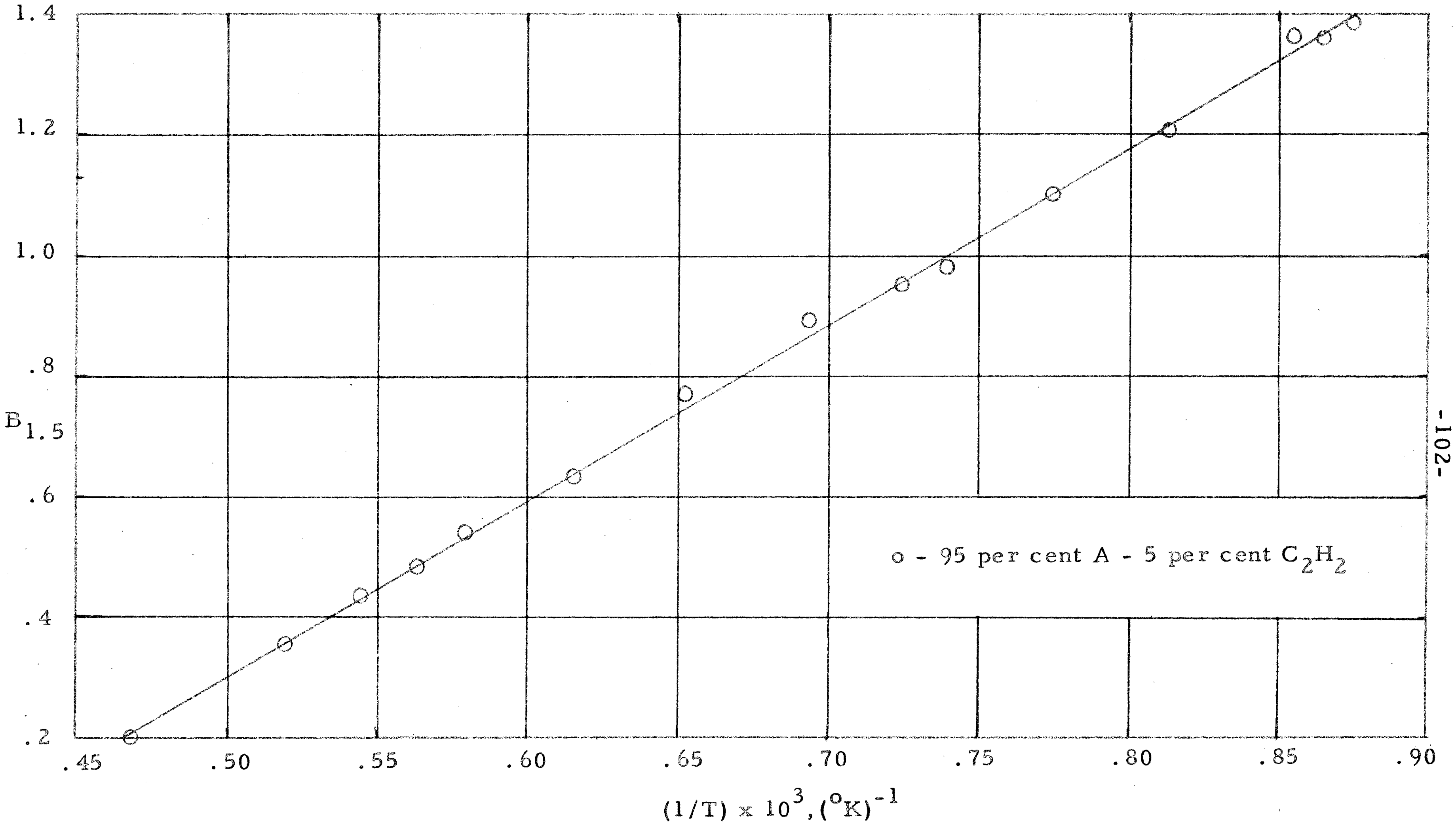

Fig. 29. The quantity $B_{1.5} = \log_{10}\left[(p_{C_2H_2})^{1.5}\,\Delta\tau\right]$ vs (1/T).

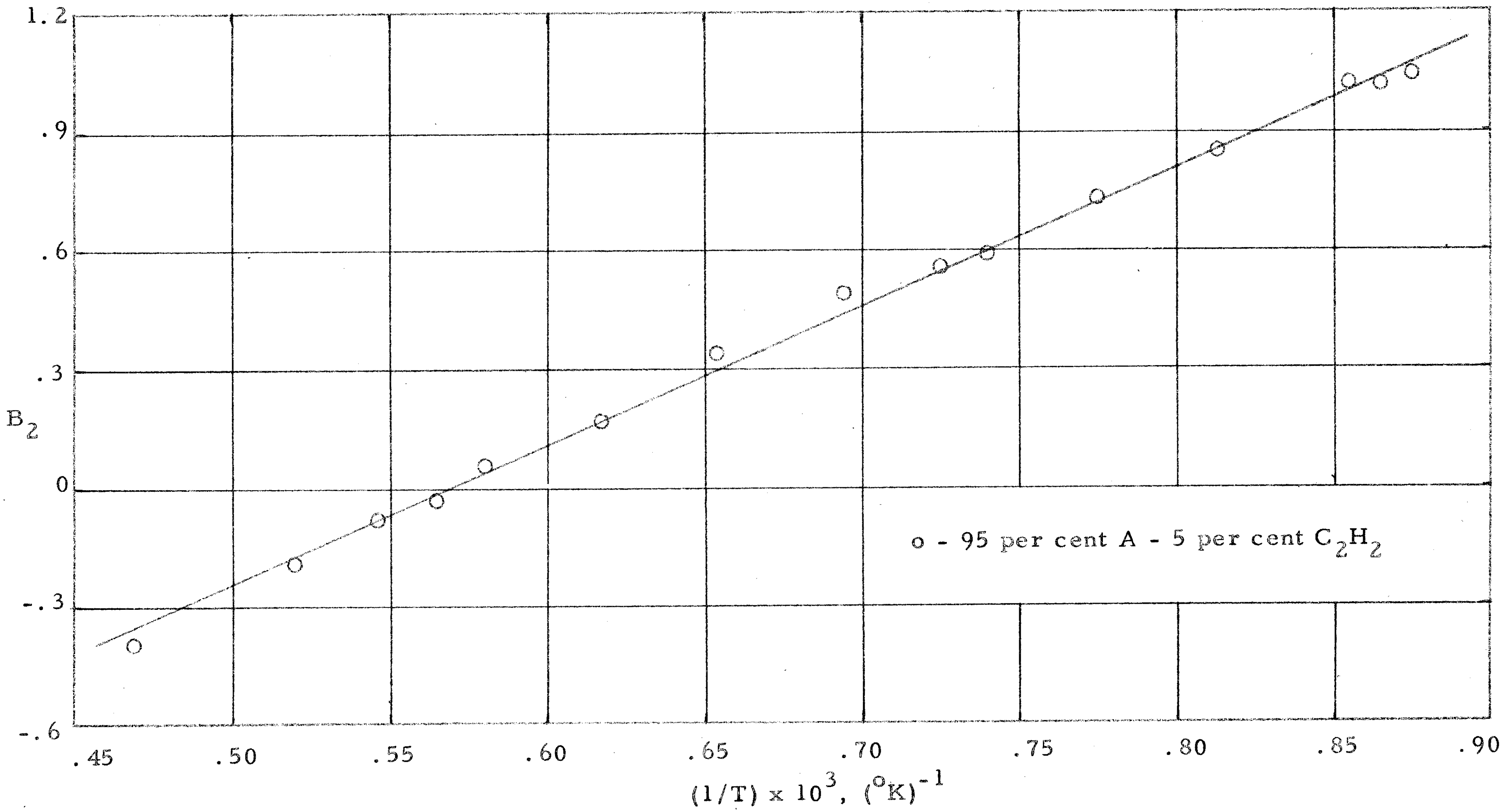

Fig. 30. The quantity $B_2 = \log_{10}\left[(p_{C_2H_2})^2 \Delta\tau\right]$ vs (1/T).

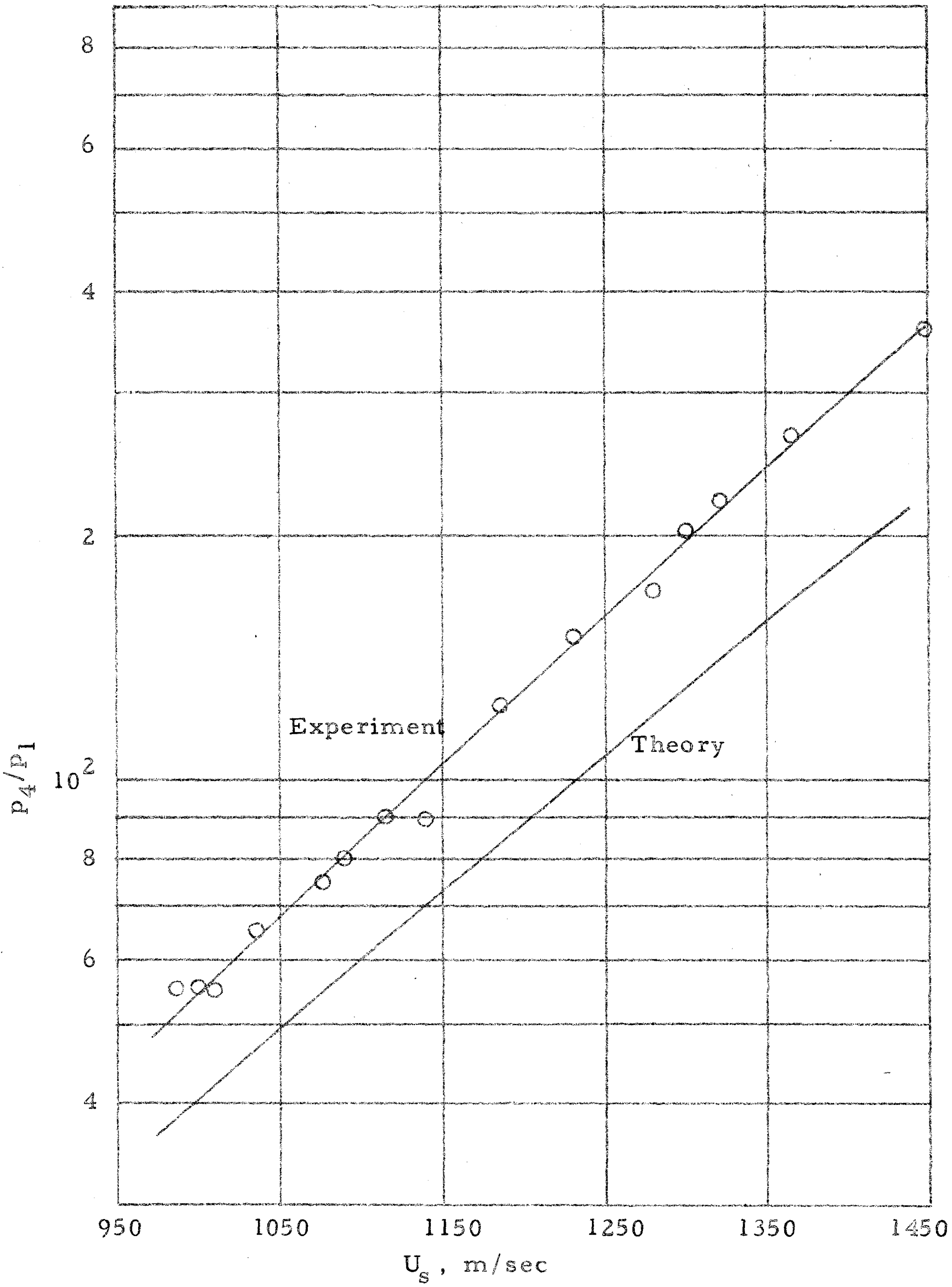

Fig. 31. Initial pressure ratio, (p_4/p_1), vs incident shock velocity, U_s, from experiments and one dimensional, inviscid, theory.

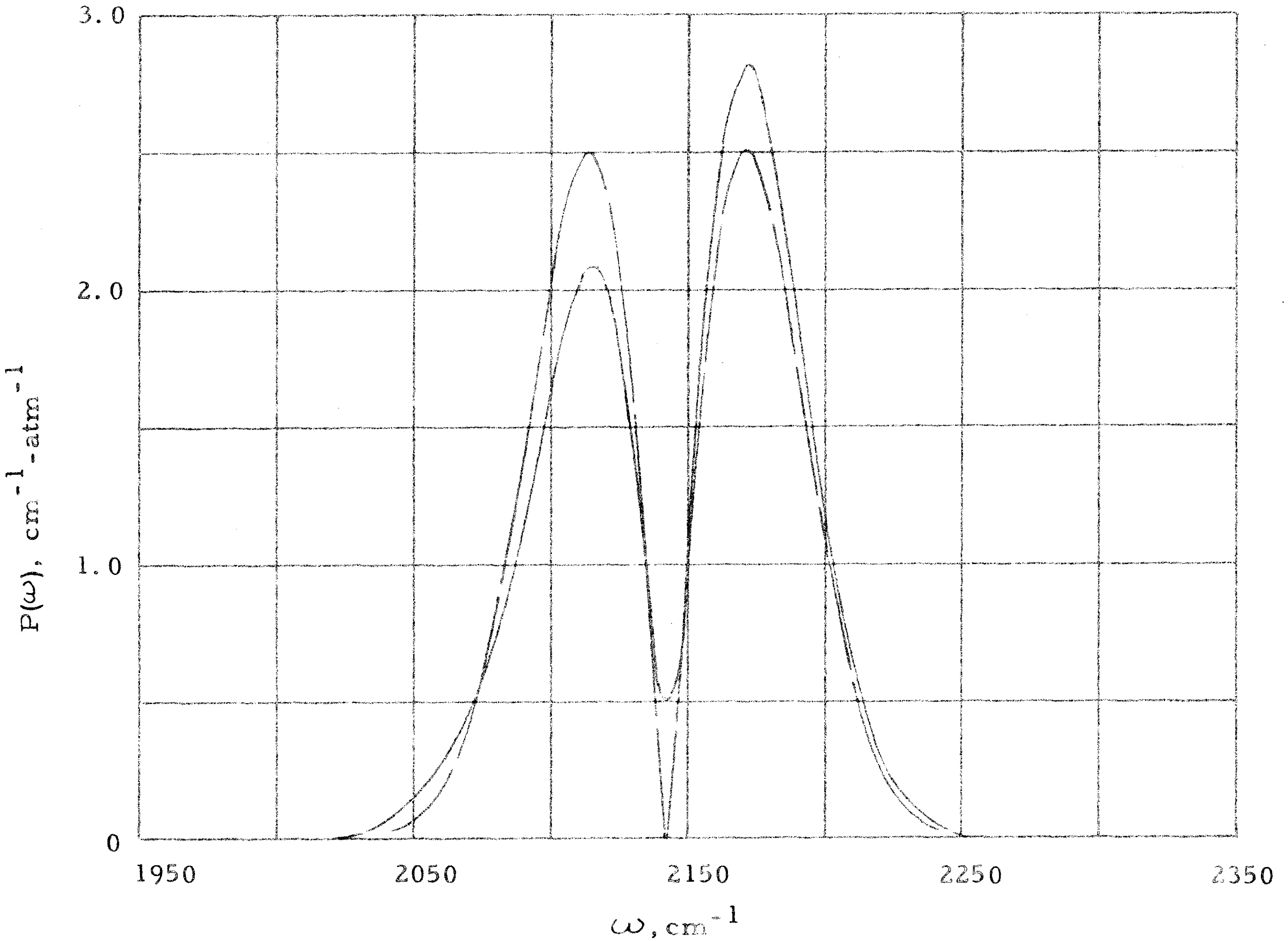

Fig. 32. $P(\omega)$ as a function of ω for the fundamental of CO at a total pressure of 47 atmos; observed: solid line [from Penner and Weber (39)], calculated: dotted line.

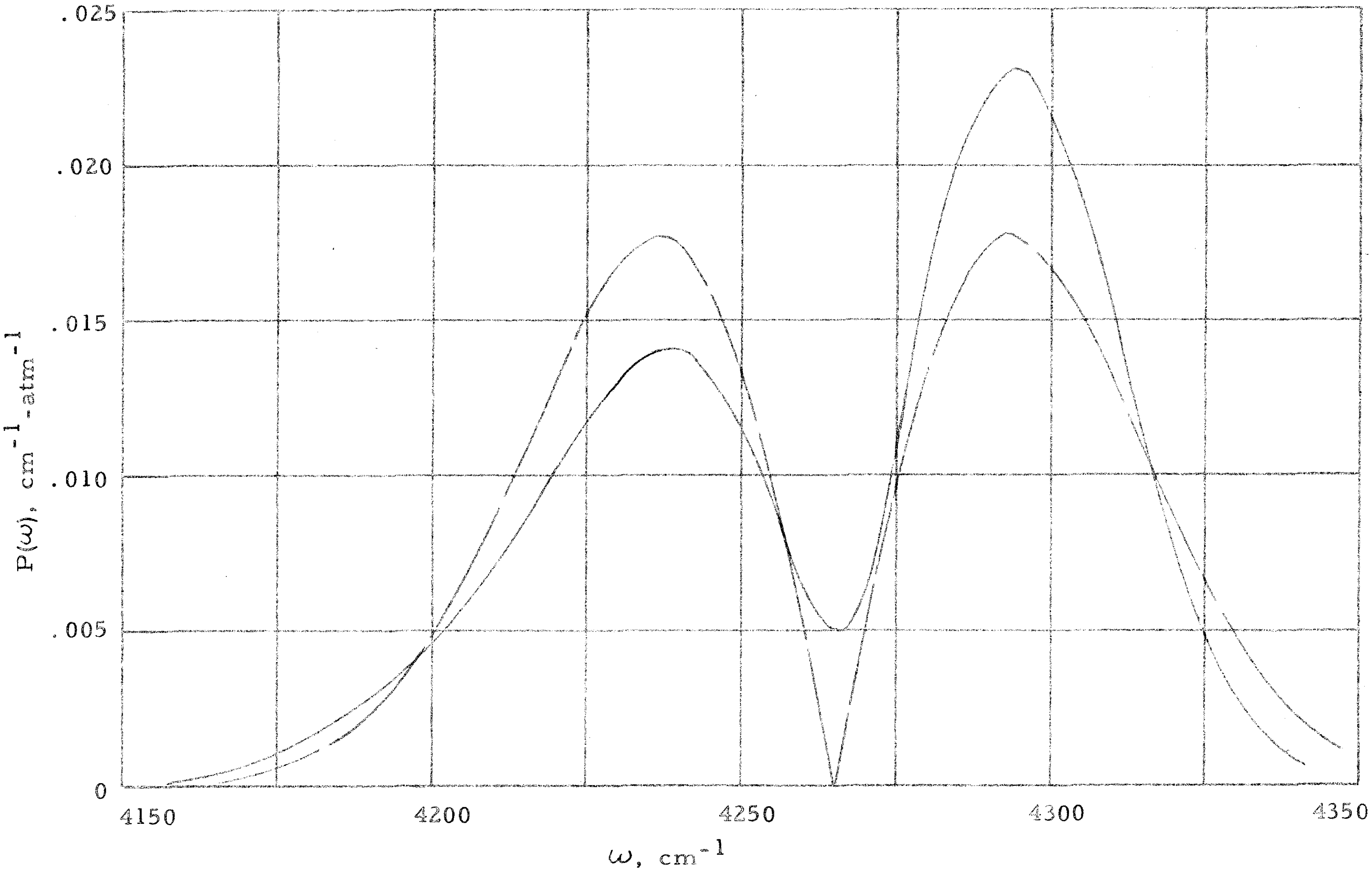

Fig. 33. $P(\omega)$ as a function of ω for the first overtone of CO at a total pressure of 47 atmos; observed: solid line [from Penner and Weber (39)], calculated: dotted line.

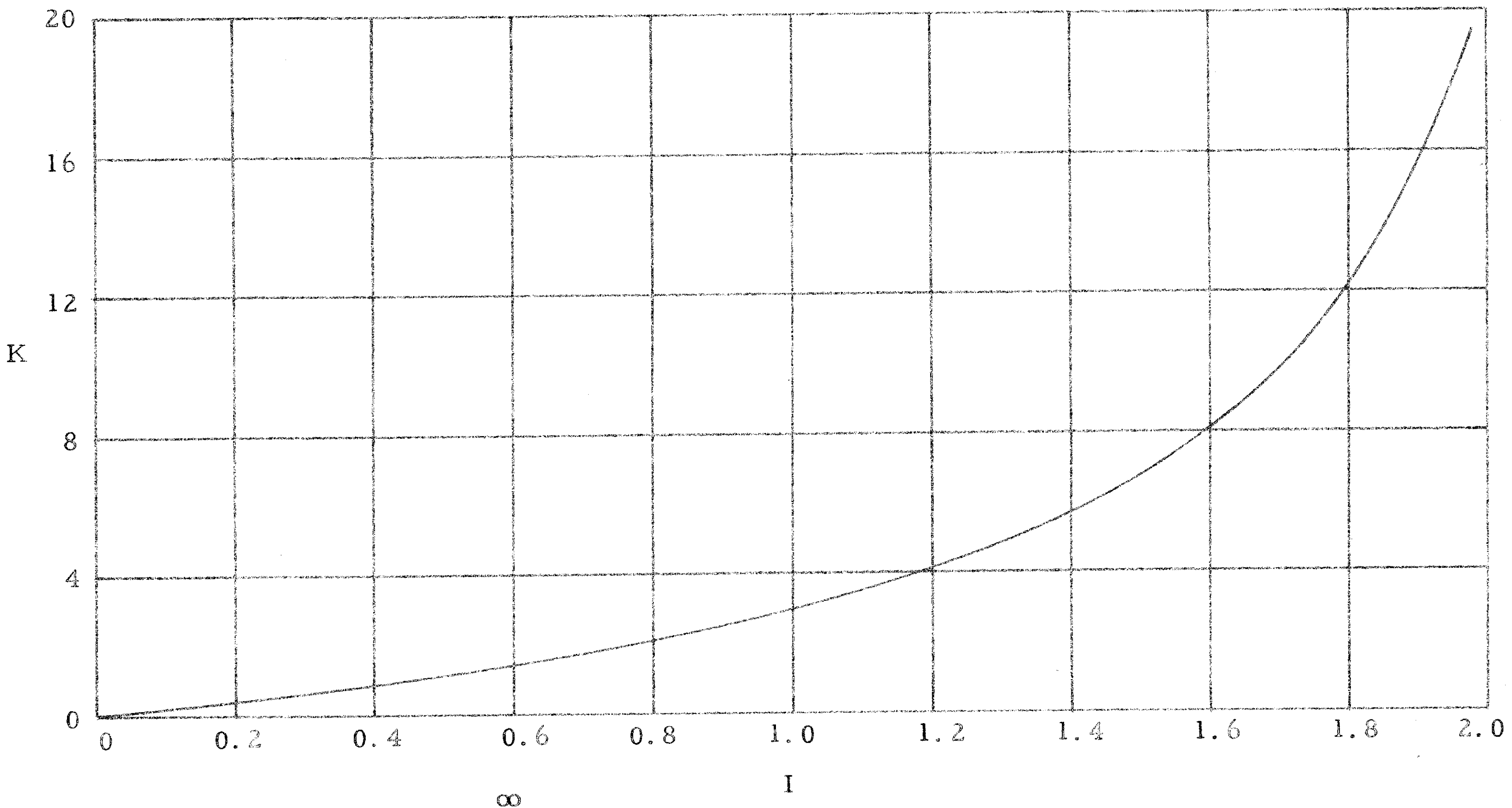

Fig. 34. The quantity $I = \int_0^\infty \left\{1-\exp\left[-K\xi \exp(-\xi^2)\right]\right\} d\xi$ vs K as computed by exact numerical integration.

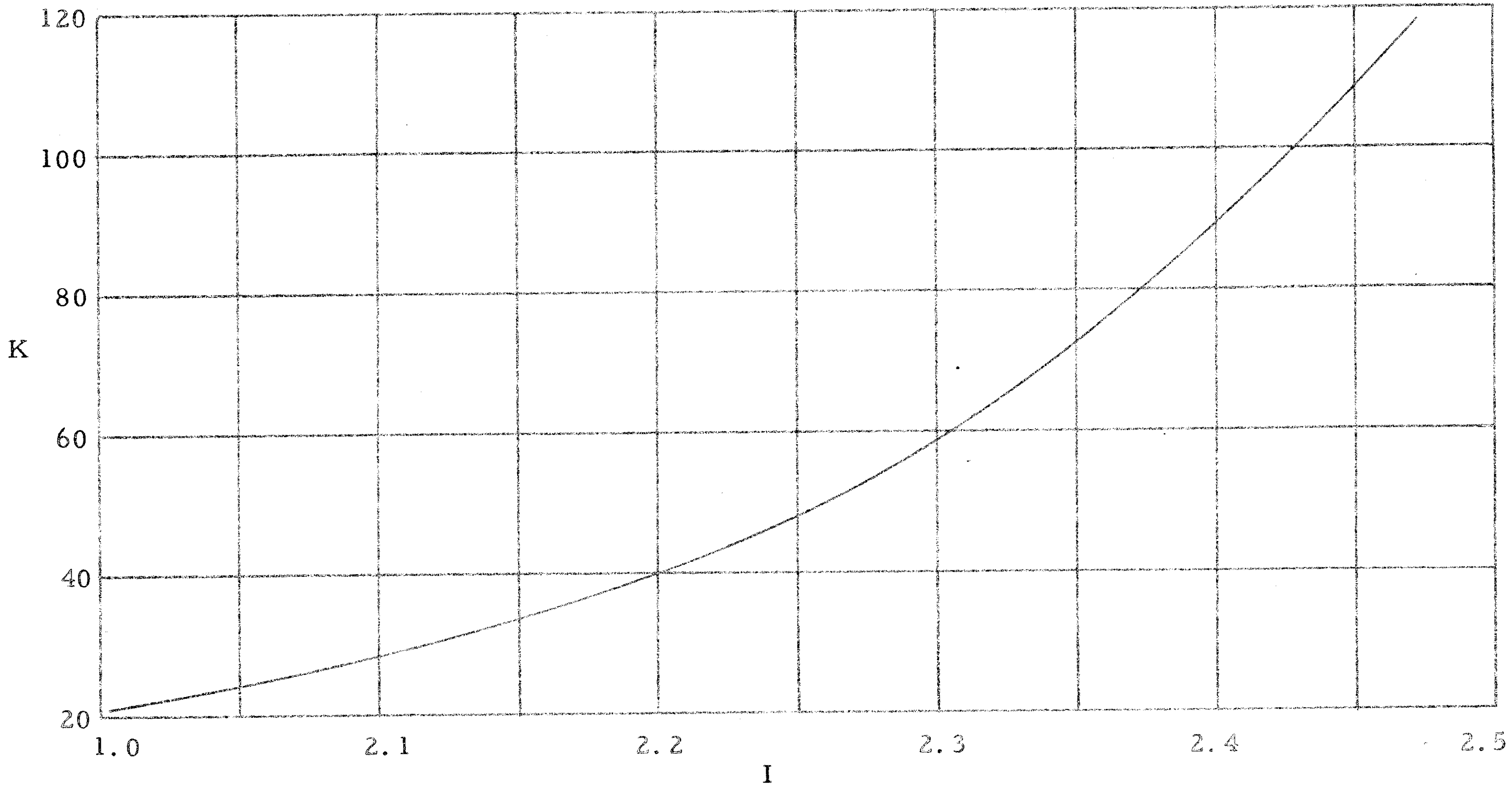

Fig. 35. The quantity $I = \int_{0}^{\infty} \left\{1 - \exp\left[-K \xi \exp(-\xi^{2})\right]\right\} d\xi$ vs K as computed by exact numerical integration.

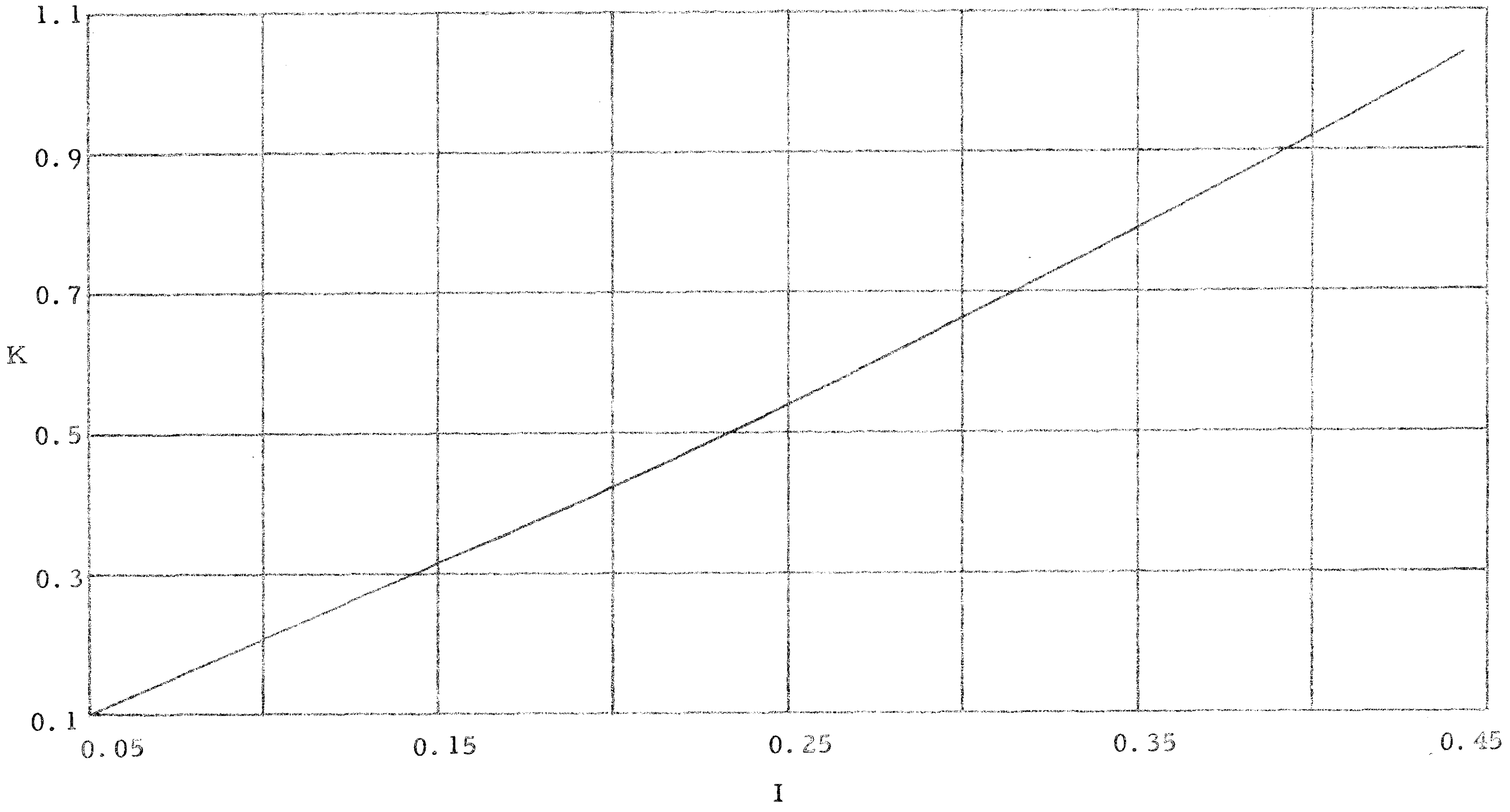

Fig. 36. The quantity

$$I \simeq (1/2) \sum_{n=1}^{9} \left[(-1)^{n+1} / (n)! \right] K^{n} \; n^{-(n+1)/2} \, \Gamma\left[(n+1)/2\right] \quad \text{vs} \ K.$$

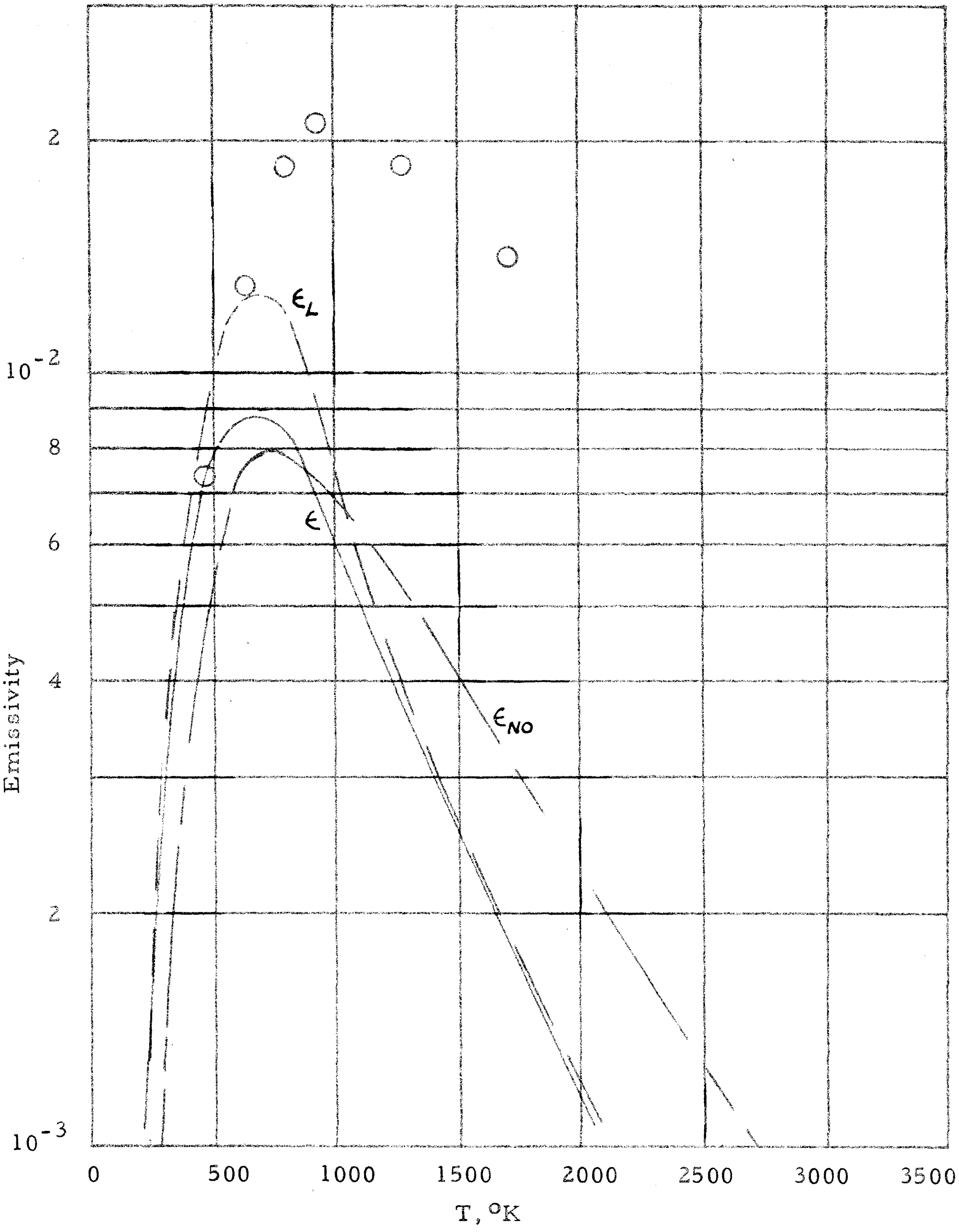

Fig. 37. Calculated and observed emissivities as a function of temperature for CO at X = 0.3 cm-atmos. ϵ : emissivities for just-overlapping lines; ϵ_L: limiting emissivities for overlapping lines; ϵ_{NO}: emissivities for non-overlapping lines; data: (O) [from Penner (34)].

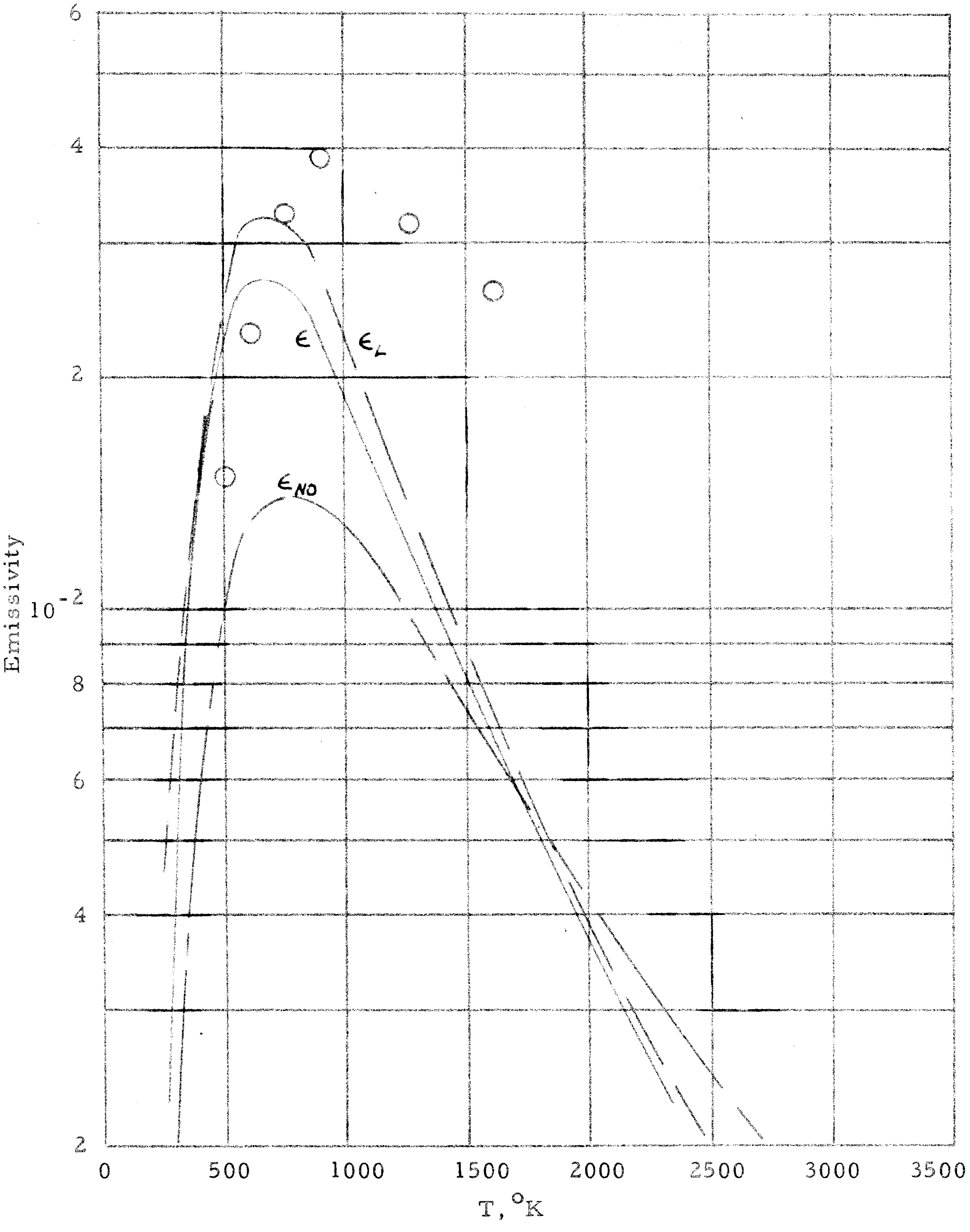

Fig. 38. Calculated and observed emissivities as a function of temperature for CO at X = 1.0 cm-atmos. ϵ: emissivities for just-overlapping lines; ϵ_L: limiting emissivities for overlapping lines; ϵ_{NO}: emissivities for non-overlapping lines; data: (O) [from Penner (34)].

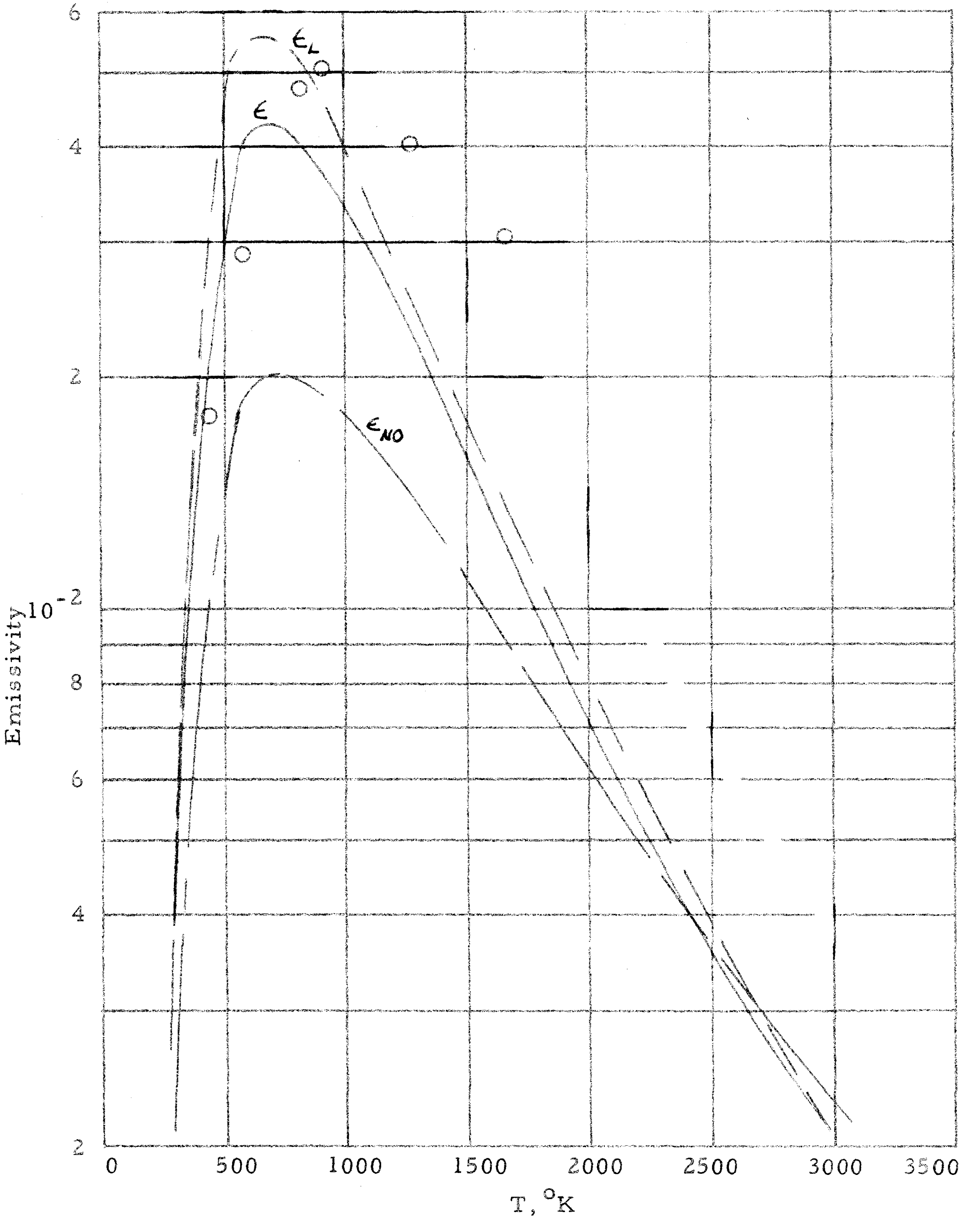

Fig. 39. · Calculated and observed emissivities as a function of temperature for CO at X = 2.0 cm-atmos. ϵ: emissivities for just-overlapping lines; ϵ_L: limiting emissivities for overlapping lines; ϵ_{NO}: emissivities for non-overlapping lines; data: (O)[from Penner (34)].

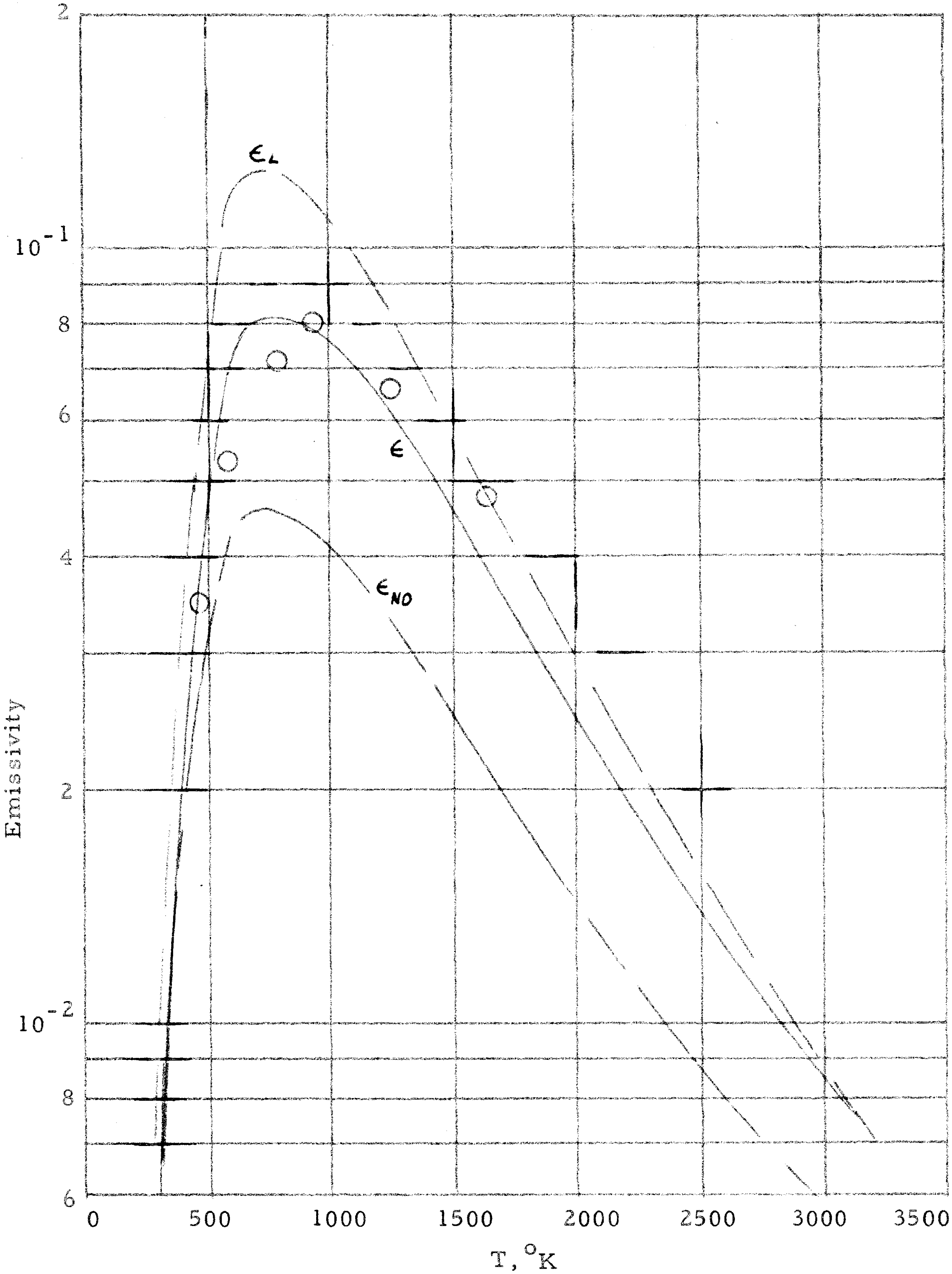

Fig. 40. Calculated and observed emissivities as a function of temperature for CO at X = 10 cm-atmos. ϵ: emissivities for just-overlapping lines; ϵ_L: limiting emissivities for overlapping lines; ϵ_{NO}: emissivities for non-overlapping lines; data: (O) [from Penner (34)].

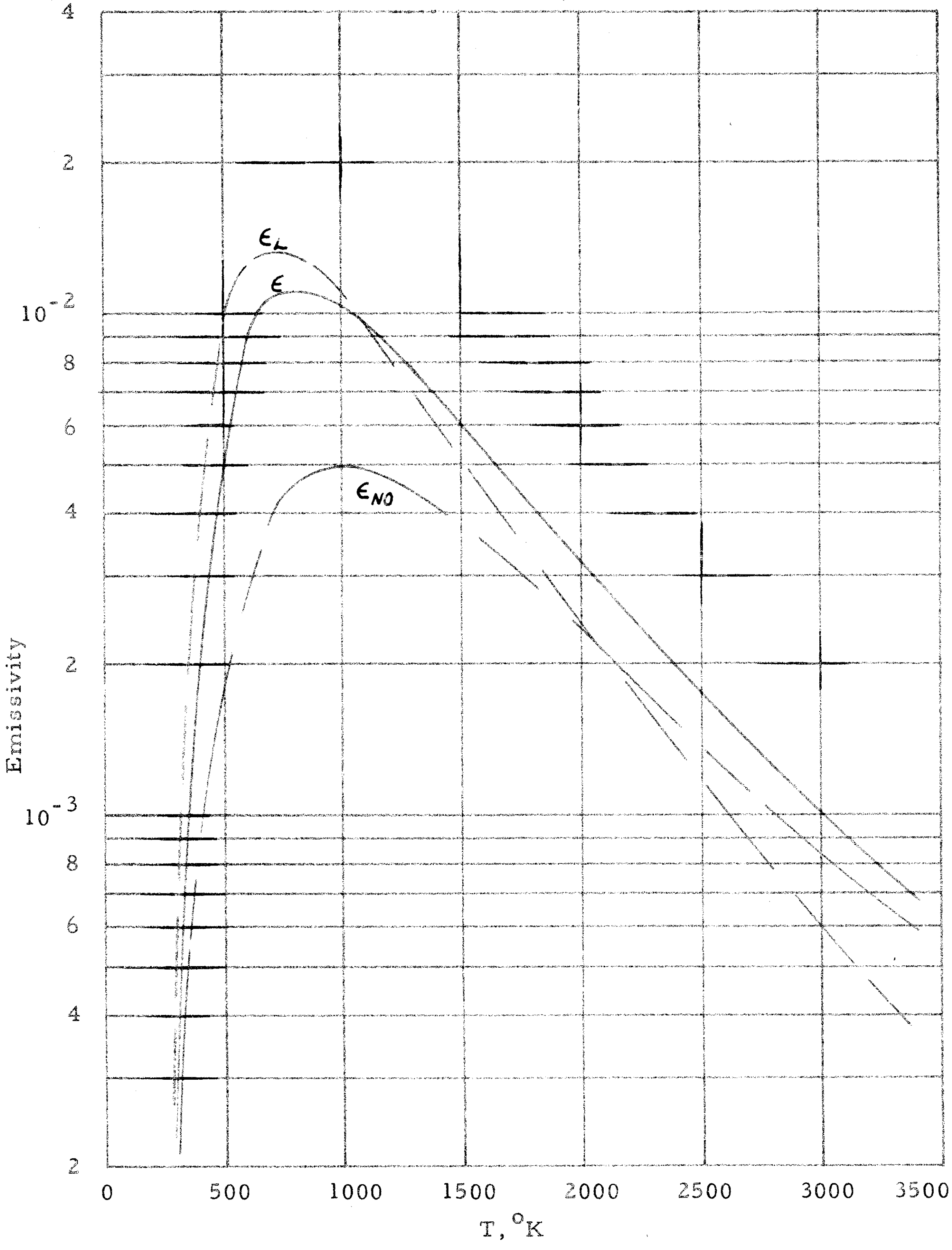

Fig. 41. Calculated emissivities as a function of temperature for HCℓ at X = 1 cm-atmos. ϵ : emissivities for just-overlapping lines; ϵ_L: limiting emissivities for overlapping lines; ϵ_{NO}: emissivities for non-overlapping lines [from Penner (34)].

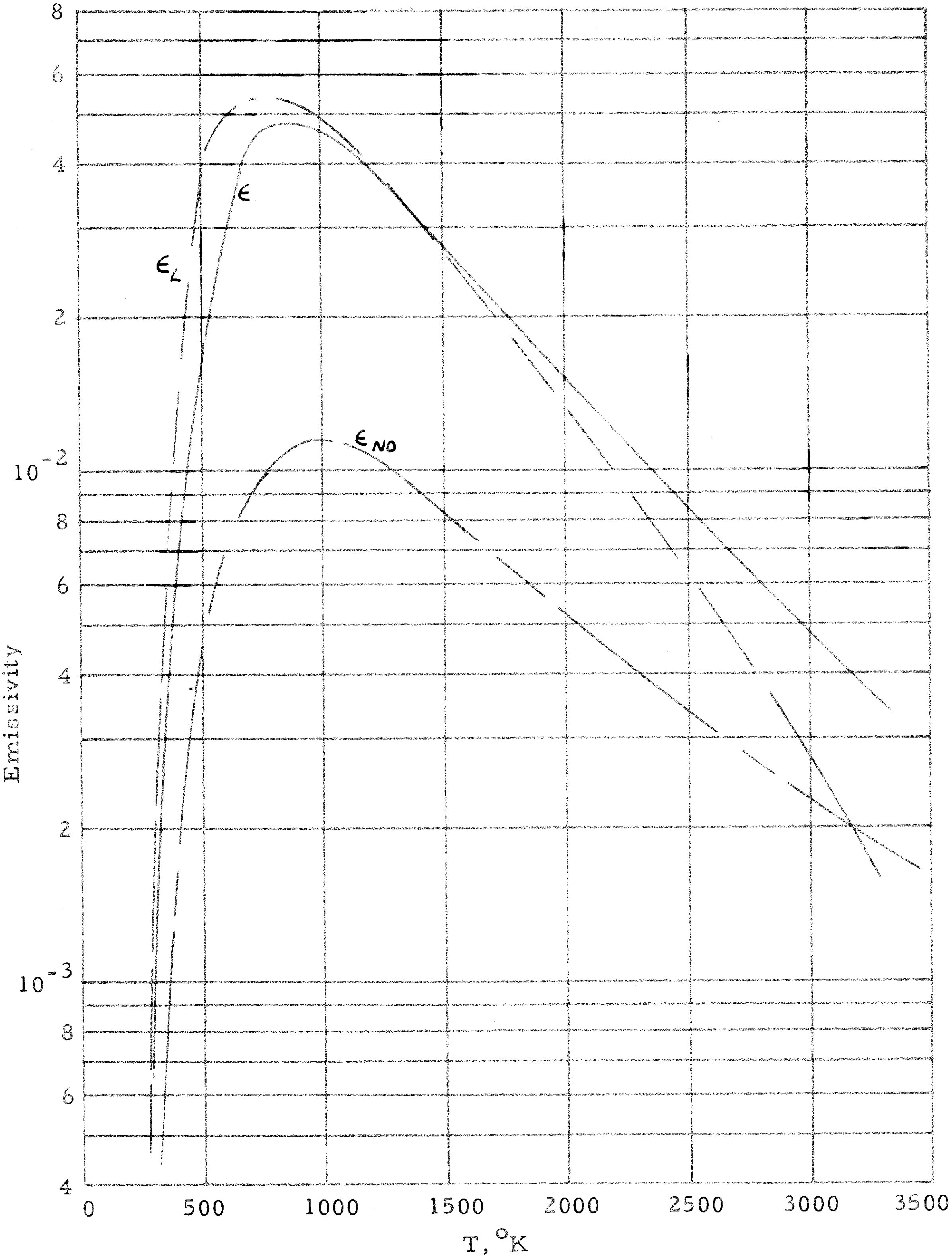

Fig. 42. Calculated emissivities as a function of temperature for $HC\ell$ at X = 5 cm-atmos. ϵ: emissivities for just-overlapping lines; ϵ_L: limiting emissivities for overlapping lines; ϵ_{NO}: emissivities for non-overlapping lines [from Penner (34)].

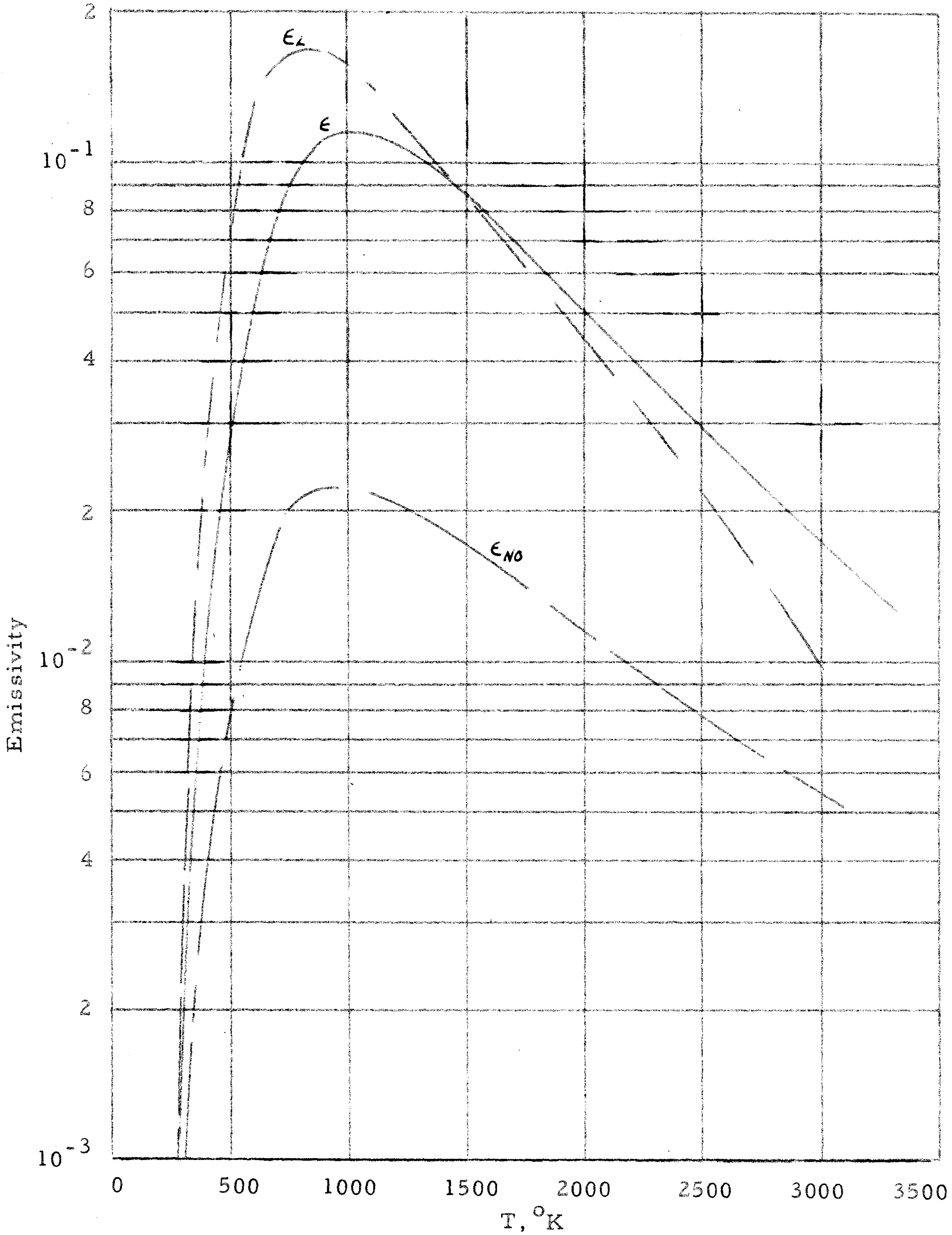

Fig. 43. Calculated emissivities as a function of temperature for HCℓ at X = 20 cm-atmos. ϵ: emissivities for just-overlapping lines; ϵ_L: limiting emissivities for overlapping lines; ϵ_{NO}: emissivities for non-overlapping lines [from Penner (34)].